



School of Chemistry

[Oliver Marsh]

Investigating the Effect of Magnetrons on the Growth of Microwave Assisted CVD Diamond

**This thesis is submitted in partial fulfilment of the requirements for the Honours Degree
of MSci at the University of Bristol**

1st assessor [Paul May]

2nd assessor [Neil Fox]

Section: [Physical and Theoretical]

Statement of Factors

The first half of my project involved growing diamond on the old magnetron setup, which all went smoothly. The other half of my project was meant to be spent on the new magnetron once it got setup. However, the installation process had many issues and the magnetron never got installed. This halted my whole project, where I was still expecting to grow on the magnetron with just two weeks left of being in the labs. So, I had to change the focus of this report from comparing the magnetrons to predicting what the diamond film grown would look like on the new magnetron. This proved to be difficult as there is no way in knowing how much more efficient the magnetron is over the old one. So I just had to do the best I could with what I had.

Abstract

Diamond is an extraordinary material. Its range of extreme and unique properties makes it a standout candidate for its use in microelectronic devices, radiation detection, water treatment and beyond. In the last three decades, significant progress has been made in the production of synthetic diamond through microwave-assisted chemical vapour deposition (MWACVD). Advancements in microwave plasma reactor design have proven to be consequential in the characteristics of the diamond film grown. Cavity magnetrons are known to lose their power efficiency over time, and so must be replaced according to their expected lifetimes. In this paper, we explore a plethora of reaction conditions that affect diamond growth, using a 25-year-old 1.5 kW ASTeX magnetron (HS-1000). A new 2 kW Sairem GMP G3 magnetron will be installed, whereby hydrogen and electron densities, and gas temperatures have been predicted using computer models. Higher microwave plasma densities (resultant from higher powers and pressures) have been found to increase the rate of hydrogen dissociation, which is directly linked to increased growth rates. Thus, optical emission spectroscopy (OES) has been chosen as a tool to find the intensities from the Balmer series transitions to predict the intensities of hydrogen transitions and growth rates on the new magnetron. Using this method, growth rates between 7.7 and 8.5 $\mu\text{m/hr}$ have been predicted for diamond growth at 1500 W and 150 torr using the new magnetron. This would produce growth rates 1.3-11.8% higher than the old magnetron under the same conditions.

Acknowledgements

Firstly, I would like to express great gratitude to my supervisor Professor Paul May. His invaluable advice has been a guiding light for me during the course of writing this dissertation. I'd also like to thank Ramiz Zulkharnay, his encyclopaedic knowledge and love for science has made my experience in the labs all the more enjoyable. Dr. James. Smith for all of his fantastic help to with Raman and optical emission spectroscopy, along with his continual efforts to implement the new magnetron system. Dr. Jean-Charles. Eloi, for showing me the ins and out of SEM, and of course, for all the stunning images of diamond taken throughout the year. Eduardo Requena Miravalles for being the fellow master's student in the office, where without his company I may not of had the incentive to work in the office as much as I did. Also, to everyone else working in the diamond labs, you all made my experience of being a project student so very fun and exciting, as well as helping me when I got stuck, which I know was a regular occurrence.

A very special mention to all my friends, for whom without, my experience at university would be very dull, and I may not have had the motivation to complete such a rigorous degree. Lastly, to my parents, Simon and Melanie, and my brother, Remy, your presence in my life has given me much meaning, and I dedicate this work to you all. Without you, none of this would have been possible. Thank you.

Contents

1. Introduction	7
1.1 Diamond	7
1.1.1 Carbon and its Allotropes	7
1.2 Diamond Synthesis Methods	8
1.2.1 High-pressure Synthesis	8
2.2.2 Early Efforts at Low-pressure Synthesis	9
2.2.3 Microwave Plasma CVD	10
1.3 Reaction Conditions and Diamond Morphology	12
1.3.1 Diamond morphology	12
1.3.2 Reaction conditions	13
1.4 Microwave Plasma Reactors	16
1.4.1 Microwaves and their uses	16
1.4.2 Plasma	16
1.4.3 Microwave Plasma	16
1.4.5 Plasma Modelling	17
1.5 The Construction of Microwave Plasma Reactors	19
1.5.1 Magnetrons	20
1.5.2 Directional Couplers	22
1.5.3 Waveguides	23
1.5.4 Waveguide Mode Converters	25
1.5.5 Resonant Cavities	27
1.6 Examples of Microwave Reactor Setups	30
1.6.1 The iPLAS Reactor	30
1.6.2 The NIRIM Reactor	31
1.6.3 The Seki-ASTeX Reactor	33
1.6.4 Summary of other MWPRs	34
1.6 Characterisation Techniques:	35
1.6.1 Raman Spectroscopy	35
1.6.2 Optical Emission Spectroscopy	36
1.7 Aims and Expectations	38
2. Results and Discussion	39
2.1 Growth Runs Using the 1.5 kW ASTeX Magnetron (HS-1000)	39
2.1.1 Pressure Dependency	39

2.1.2 Power Dependency	42
2.1.3 Methane Concentration Dependence	45
2.1.4 Nitrogen dependence	50
2.1.5 Effect of Wire Thickness	53
2.2 Diamond Growth Predictions using the Sairem GMP G3 Magnetron System.....	56
3. Conclusions.....	61
4. Future Work.....	62
5. Experimental Details	64
5.1 Substrates and Abrasion	64
5.2 The University of Bristol MWPR	64
5.3 Growth Runs Using the MWPR.....	65
5.4 Characterisation Apparatus.....	66
5.4.1 Raman Spectroscopy	66
5.4.2 SEM	66
5.4.3 OES.....	67
6. Bibliography.....	68

1. Introduction

1.1 Diamond

1.1.1 Carbon and its Allotropes

Carbon is the sixth element in the periodic table and is the most fundamental element for life on Earth. Due to carbon's ability to multiple bond, it can take up many structural forms which have different chemical and physical properties; this is known as allotropism. There are two categories of allotropes of carbon: crystalline (diamond, graphite, fullerenes, etc figure 1) and amorphous (coal, wood charcoal, lampblack, etc).¹ The high cohesive forces that hold these large polycrystalline allotropes of carbon together, along with a high activation energy allows carbon polymorphs to exist in a temperature and pressure region that is usually of another form. This is why diamond exists at room temperature despite being most thermodynamically stable at extreme temperatures.² When looking at desirable material properties, diamond tops nearly every list. Its extreme hardness, chemical inertness, wide band-gap, thermal conductivity and negative electron affinity offers great promise for its use in numerous micro-electromechanical devices.³ Diamond is formed by the bonding of sp^3 hybrids, in which carbon bonds with four equidistant neighbours, where tetrahedral symmetry is present. Graphite's structure is comprised of sheets of carbon atoms forming three σ bonds using its sp^2 hybridised orbitals, and one unhybridized p orbital, giving bond angles of 120° . The electron in the p orbital is delocalised, which gives rise to its conductive properties.

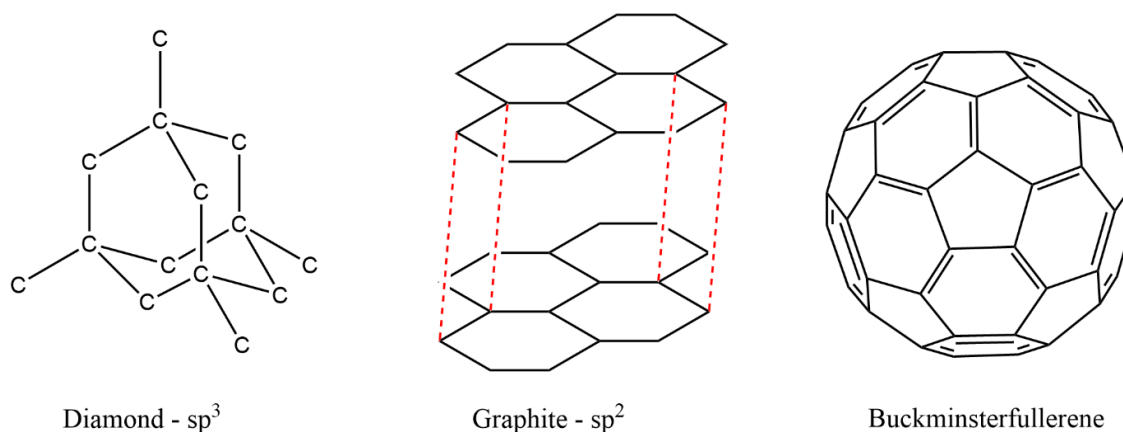


Figure 1: Three allotropes of carbon where one unit cell of diamond is shown.

Both graphite and diamond are the two allotropes of carbon that are most stable in the solid state. The formation of these polymorphs can be summarised in a phase reaction diagram (figure 2). As the pressure of the system is increased, the preference for the formation of diamond is also increased. The window for graphite formation increases linearly with temperature, where above 2300 K and at pressures of around 6 GPa, the graphitization of diamond can occur within minutes.^{4, 5} Along the line ABC, marks the points at which graphite and hexagonal-type diamond can be converted into

cubic-type diamond. Hexagonal type diamond is one in which its first and third layer can be superimposed on each other (i.e., ABABAB sequence of layers). Cubic type diamond has a sequence of ABCABC..., in which its first and fourth layer can be superimposed on each other. At point A on the dashed curve, a solid-solid conversion of graphite to cubic diamond occurs. At point B, hexagonal graphite is converted to cubic diamond, and at C, hexagonal diamond is converted into cubic diamond. Graphite can exist far into the diamond region (at point A), and diamond can exist far into the graphite region (point D). When either sp^2 or sp^3 carbon atoms get stuck in their respective bonding modes, a high amount of activation energy is needed to convert an assemblage of sp^2 to sp^3 carbons and vice versa. Thus, metastable forms of these allotropes can exist in the regions of thermodynamic stability for the other kind.⁶ This is the basis for high temperature high pressure techniques, where the idea is to create conditions similar to that inside Earth.

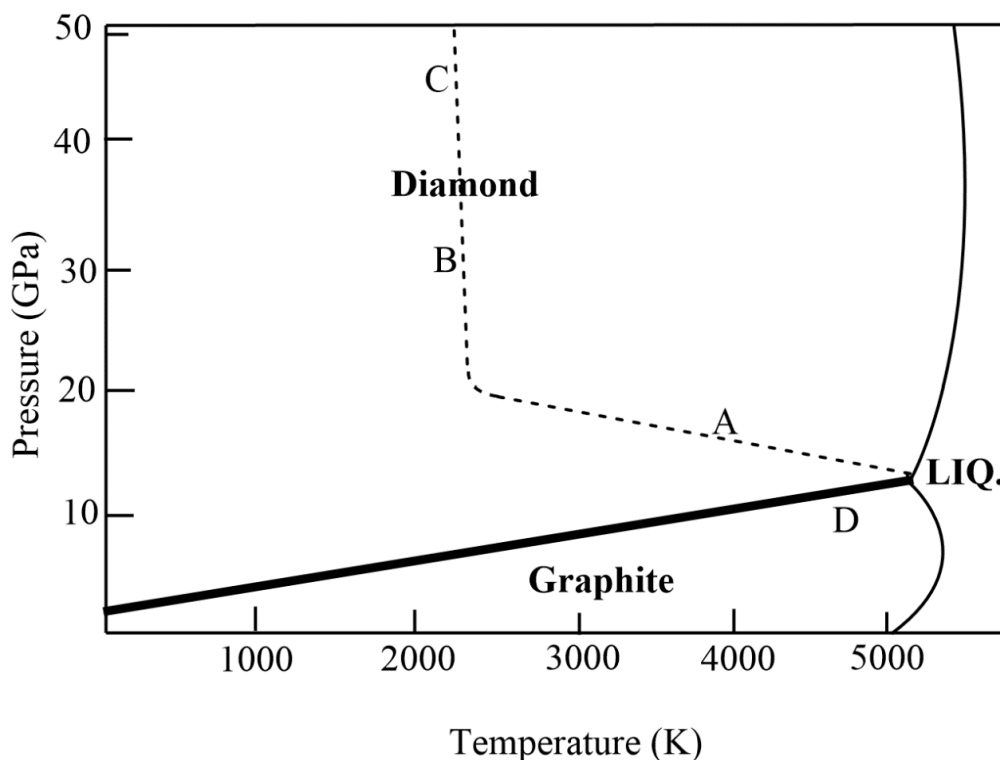


Figure 2: A phase reaction diagram for the formation of diamond and graphite. Along the ABC dashed line, fast pressure/temperature cycles readily convert graphite or hexagonal diamond into cubic type diamond. At point D, the graphitisation of diamond occurs.

1.2 Diamond Synthesis Methods

1.2.1 High-pressure Synthesis

Diamond was long believed to be synthesised only under high pressure, in its region of thermodynamic stability (figure 2). General Electric were the first corporation to announce the man-made synthesis of diamond in 1955.⁷ This was confirmed by X-ray diffraction patterns, and hardness

tests – where the man-made diamonds were hard enough to scratch the face of {111} natural diamond, and the fact that the diamond was repeatedly synthesised (figure 3).

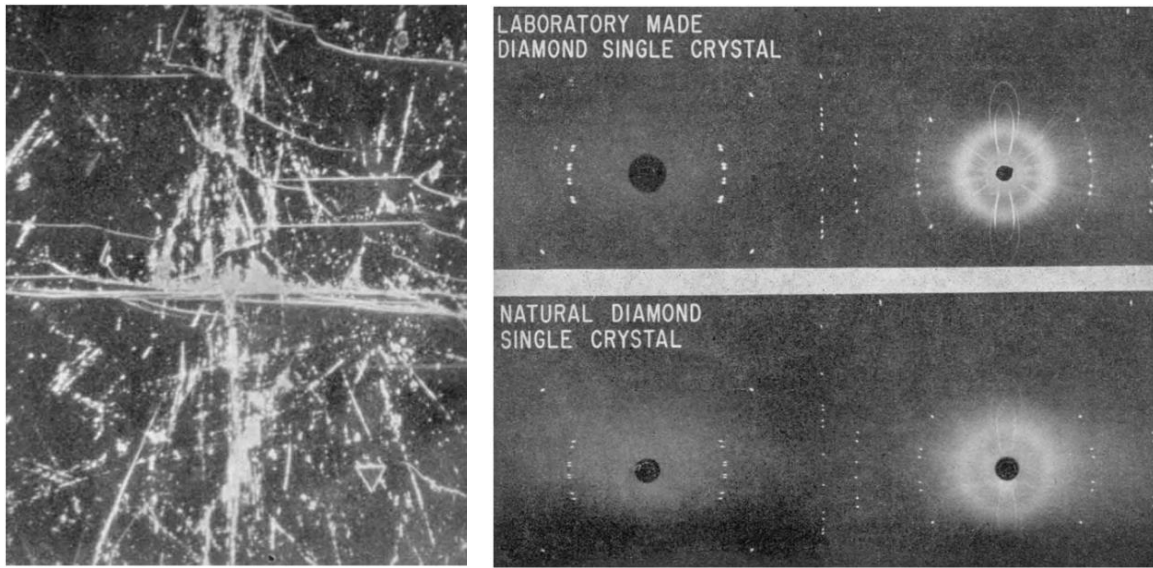


Figure 3: On the right are X-ray diffraction patterns of man-made and laboratory made diamond crystals. On the left are scratches made on {111} diamond, the horizontal scratches are growth steps, and the triangle on the bottom right is a growth mark commonly found on diamond faces.⁷

2.2.2 Early Efforts at Low-pressure Synthesis

Performing low-pressure synthesis of diamond in its metastable state was likely first achieved by Schmellenmier in the early January of 1956.⁸ Acetylene was decomposed in a glow discharge, where black carbon layers were found on the cathode that showed a remarkably high scratch hardness. Laue photographs showed that the material had a cubic lattice, and Debye-Scherrer photographs showed two strong lines indicative to that of diamond, with the graphite lines not present. Schmellenmier said “...there are also crystalline areas that show a diamond-like structure, presumably even diamonds.” The next major development in the formation of crystalline diamond was made in the early 1970s by Angus, where it was found that the use of hydrogen etched graphite faster than it does to diamond.⁹ This led to greatly increased growth rates, allowed for higher purity since less graphite will be present in the carbon sample after growth, and made the nucleation of diamond crystals on non-diamond substrates possible. In 1982, Namiki, Sakura-mura and Niihari-gun, researchers at the National Institute for Research in Inorganic Materials (NIRIM), published a number of techniques for the low-pressure deposition of diamond.^{10,11} These included: chemical vapour deposition (CVD), ion-beam deposition, sputtering, and plasma CVD. The group from NIRIM deposited diamond onto silicon wafers using a hot tungsten filament in a methane and hydrogen atmosphere at temperatures from 600 to 1000 °C, with pressures ranging from 10-100 Torr (figure 4). This pioneering research kickstarted the creation of CVD diamond groups across the globe.

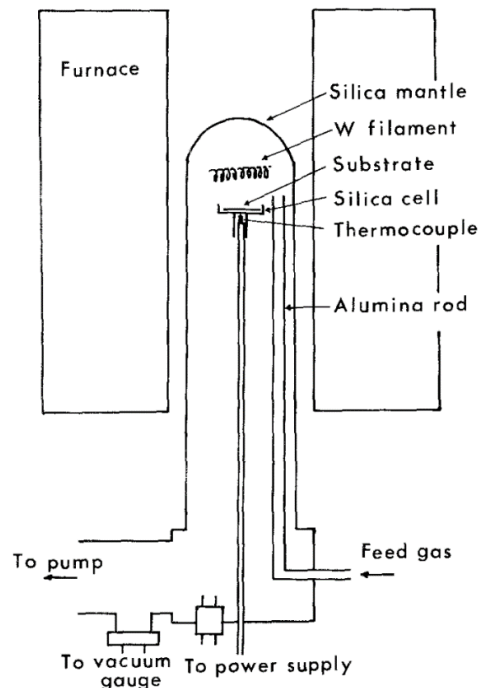


Figure 4: A diagram of the hot filament method used by the NIRIM group.¹⁰

2.2.3 Microwave Plasma CVD

Chemical vapour deposition (CVD) is a process used to grow thin films on substrates using a reactive precursor molecule to initiate the reaction. In the case of growing CVD diamond, hydrogen is activated through an activation region, causing the gases to fragment into reactive radicals and atoms, creating ions and electrons in the process (figure 5).¹² The activation region is generated using power from a cavity magnetron which produces microwaves. These microwaves are then used to excite pre-existing electrons in the gas mixture, forming a plasma, then fragmenting the gases. This process is known as microwave assisted chemical vapour deposition (MWACVD), which will be explained in much more detail in section 2.4.

For this report, only microcrystalline diamond (MCD) will be considered, but for many uses such as in semiconductors, nanocrystalline diamond (NCD) surpasses MCD due to its high surface smoothness. MCD can be formed via CVD, and this is summarised in figure 5. Initially, a substrate must be abraded using diamond dust, which forms scratches on the surface, allowing for the nucleation of the activated gases. A hydrogen atom can abstract a surface hydrogen forming a carbon radical on the surface, and a hydrogen molecule. The surface radical is then attacked by a gas-phase CH_3 species. This happens again on an adjacent unit, until another hydrogen atom abstracts yet another hydrogen off the methyl group to form a CH_2 radical. This then goes on to attack the adjacent methyl group to form a carbon lattice, in which under the correct conditions is diamond. This explanation doesn't quite give the full picture for diamond growth. Graphite is etched by hydrogen at much higher rates than diamond, which leads to major removal of graphite at the surface. Indeed, the sputtering rate decreases by a factor of around 100 times from graphite to diamond (from $7.7 \times 10^3 \text{ s}^{-1}$ for graphite and 75 s^{-1} for diamond).¹³ Hence, the favoured etching of graphite by hydrogen leads

to the preferential formation of diamond, not the diamond having superior growth rates over graphite.¹⁴

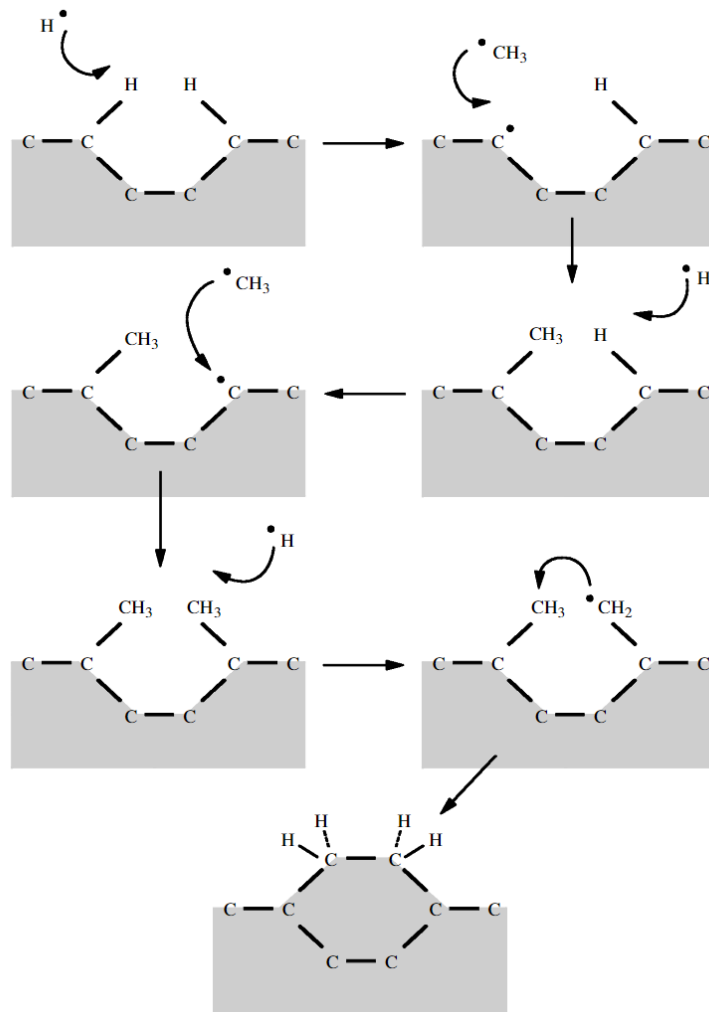
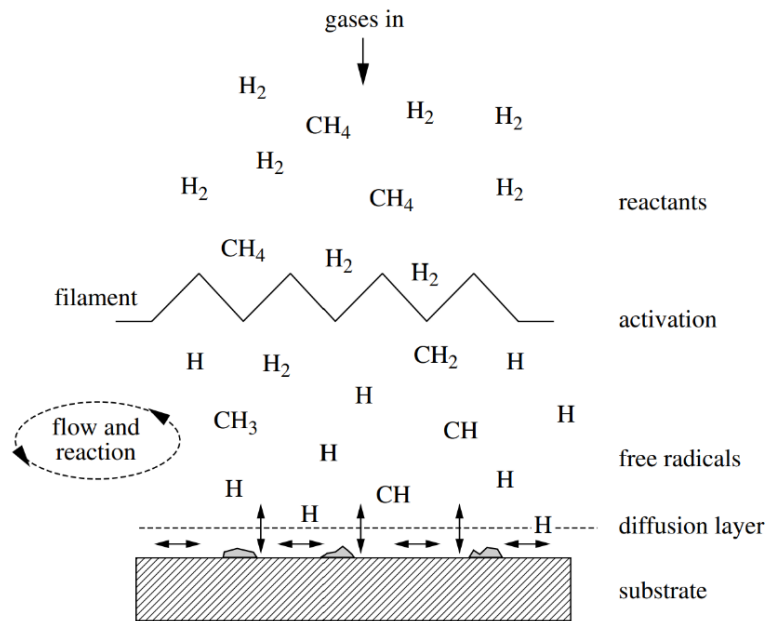


Figure 5: This diagram summarises the activation step and mechanism for CVD of diamond in a microwave plasma reactor.¹²

Microwave plasma deposition offers many advantages over high pressure high temperature synthesis, one of which is the ease of altering the power output which can influence the speed of diamond growth. Another, is the high diamond purity which can be formed since the plasma ball sits above the substrate, away from the chamber walls and hence prevents contamination of the diamond film.¹⁵

1.3 Reaction Conditions and Diamond Morphology

1.3.1 Diamond morphology

Diamond can adopt different morphological structures depending upon reaction conditions. During CVD, square faceted {100} crystals are in competition with triangular faceted {111} crystals (figure 6).¹⁶ This competition is seen in cubooctahedral structures where both triangular and square faces are present on each crystal.¹⁷ At temperatures exceeding 750 °C at high plasma intensity, octahedral diamond dominates, below this temperature cubooctahedral structures form, and at temperatures lower than 640 °C, under average plasma intensity, cubic diamond is seen.¹⁸

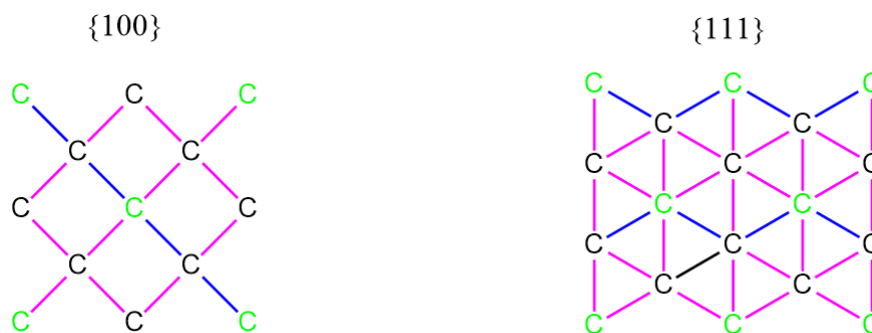


Figure 6: This diagram represents the atomic arrangement of homoepitaxial {100} and {111} diamond structures as viewed from the top. The carbon atoms in green and the bonds in blue are those on the top layer. Those carbon atoms in black and the bonds in pink are in the crystal plane below the top ones. {100} faces make-up cubic diamond, and {111} face make-up octahedral diamond.

LEED (low energy electron diffraction) patterns of homoepitaxially grown diamond can be used to determine diamonds morphology. The images in figure 7 and 8 clearly identify the differences in the surface structures of {100} and {111} diamond.

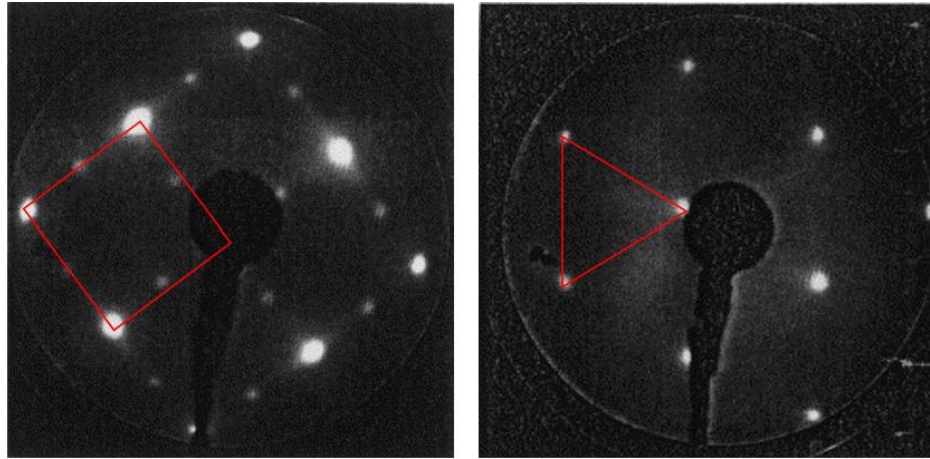


Figure 7: The LEED pattern on the left is homoepitaxially grown C{100} diamond taken at 80 eV. The red square indicates the square facets that gives rise to its surface structure. The pattern on the right shows a hexagonal pattern and is indicative of a C{111} structure that was grown at 690 °C and 98 eV. The red triangle outlines that seen in the surface structure of diamond – triangular facets.¹⁹

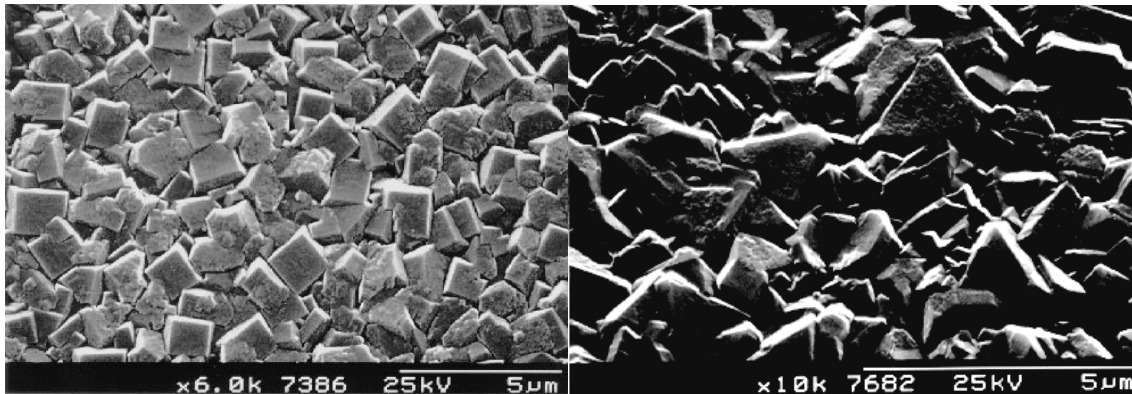


Figure 8: The SEM images show {100} diamond on the left, and {111} diamond on the right. The square and triangular facets can clearly be seen in respective photographs.²⁰

1.3.2 Reaction conditions

Altering the conditions by which the diamond film is grown in affects the growth rates, surface roughness, and morphology of the sample. Substrate temperature is a key parameter which affects the samples growth, and the temperature can be changed through the microwave power, controlling the substrate cooling rate, and deposition pressure.²¹ The ratio of C:H:O is vital as the atmosphere affects the morphology and quality of diamond film grown, which this is summarised via a Bachmann triangle diagram in figure 9.²²

Gas mixtures

Looking first at figure 9, there are three elements considered, O, C and H and these can combine into various molecules to form different atmospheres. For any binary gas composition, the data point is on the edges of the triangle. For CO, we have a mixture containing 50% C and 50% O, thus its data point is at 0.5 on the C-O line. For methane, we have 80% H and 20% C, hence it's found at 0.8 along

the H-C line in favour of H. What is evident from the studies taken by Bachmann is that there is a narrow window for diamond growth, especially for growing good quality homoepitaxial diamond film.²² Most microwave plasma experiments have used high concentrations of hydrogen mixed with a diluted carbon carrier such as methane. A small, shaded section in the bottom left of figure 9 contains lots of data for diamond growth. For the premise of this report, this small section will be explored through the variation of methane with hydrogen.

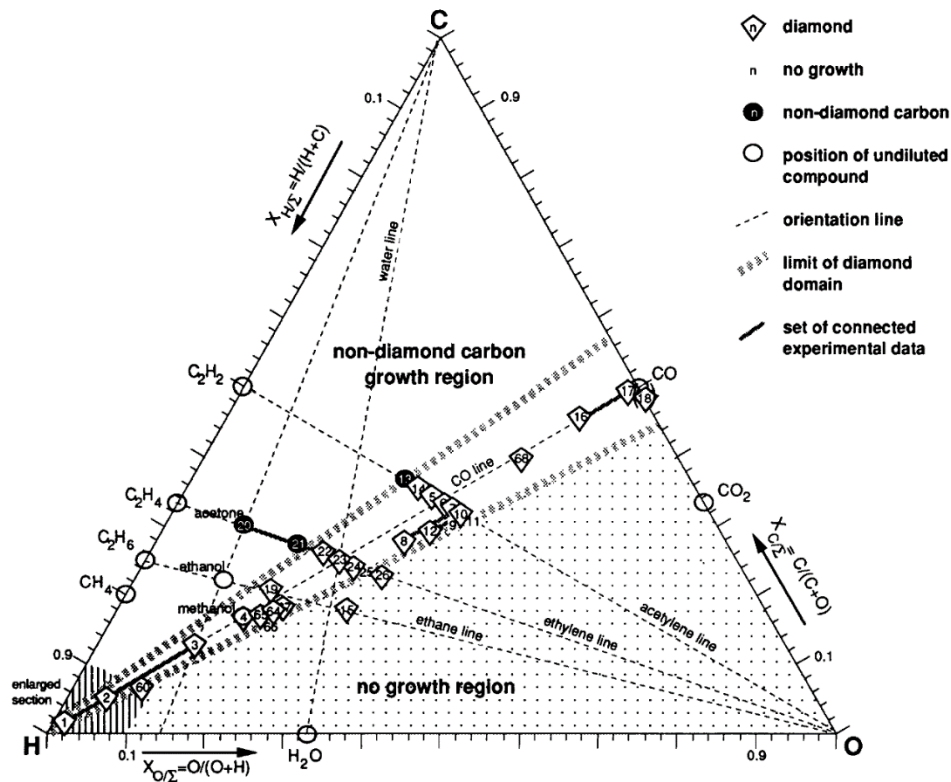


Figure 9: Bachmann's triangle diagram, showing the area for diamond growth which lies just to the C-side of the CO line. The shaded section in the bottom left is an area of high density of data points rich in hydrogen which is of particular interest.²²

Increasing growth rates

To maximise profitability in industry, high deposition rates should be achieved to minimise the time of growth, and hence minimising energy usage. There are several ways in which this can be achieved, the first to be discussed is temperature. It is known that the growth rates for diamond films follow Arrhenius type kinetics and reaches a maximum at around 1000 °C.²³ A maxima is reached because CH₃ and C₂H₂ desorption starts to outcompete the adsorption of the activated carbon species at raised temperatures. This etching process slows {100} growth rates, whilst {110} and {111} rates remain unaffected and maintain a steady growth rate at temperatures higher than 1000 °C.²⁴ The increase in etching rates for {100} serves to smoothen the {100} diamond surface, but also accounts for the domination of triangular and trapezium shaped grains observed at these temperatures, which conversely causes the overall surface to roughen.

Adding a small amount of nitrogen to the system can increase growth rates in the {100} direction.²⁵ The reason for this was proposed by Frauenheim *et al.* in a computational study, whereby the bond in the {100} plane is lengthened via an additional electron from N₂. Only a small amount of nitrogen is required, since the electron becomes available again, as the electron ‘jumps’ from bond to bond. In fact, a saturation point is reached as the electrons from N₂ molecules become evenly distributed across the diamond surface. Thus, there comes a point where an increase in N₂ concentration does not increase the growth rate. This has been investigated by Achard *et al.* where nitrogen concentrations were used between 75 and 200 ppm, and a plateau region was expected to follow soon after (figure 10).²⁶ From their study, at [N₂] of 150 ppm at 950 °C the grains are most well defined on single crystal diamond. However, at high concentrations of nitrogen, the electronic properties are significantly diminished. Thus, only at low N₂ levels (5 to 10 ppm), are the diamond crystals are of suitable quality to be used for thermal and optical applications.

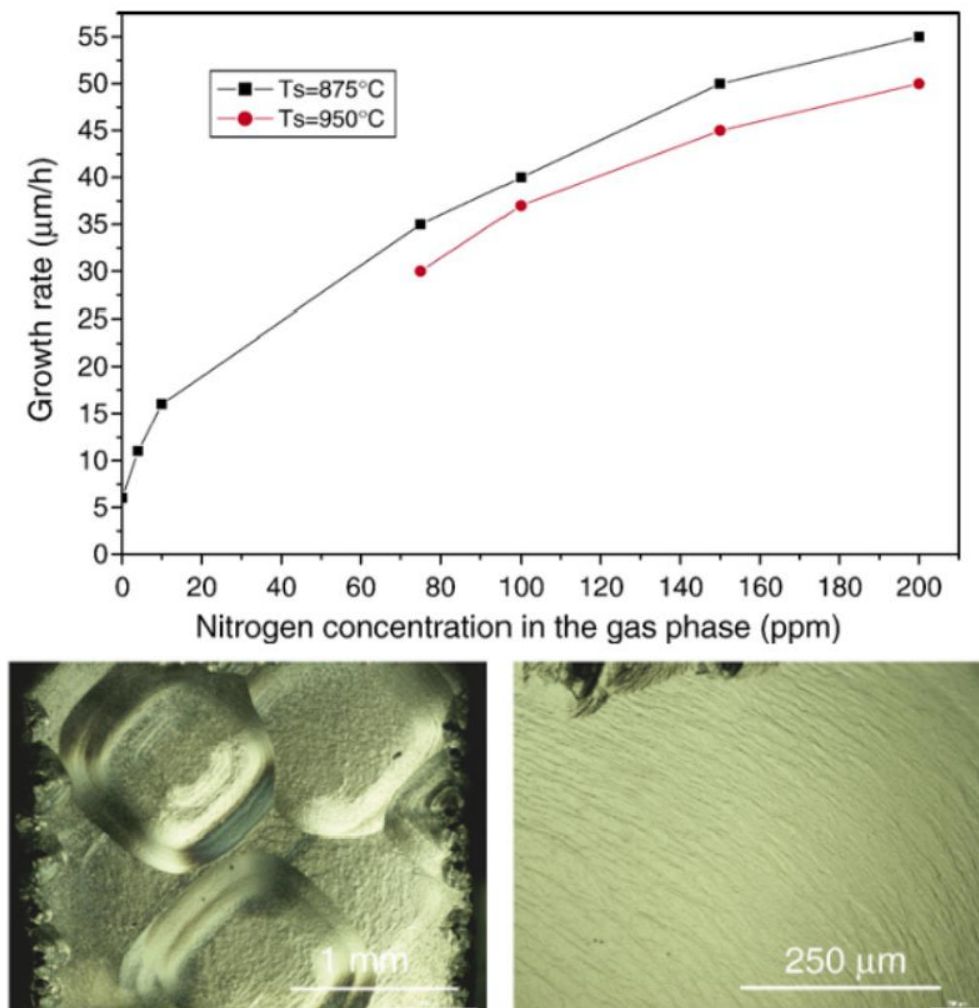


Figure 10: The first image is a graph showing how the increase of [N₂] in the gas feedstock causes the growth rate of single crystal diamond to increase.²⁶ A plateau region is expected to follow as the surface of diamond becomes supersaturated. The data points at 0, 4 and 10 ppm are from another source.²⁷ The lower image shows differential interference contrast microscopy (DICM) images of single crystal diamond of [N₂] at 150 ppm and 950 °C at low and high magnification. At low

magnification large defined square crystals are observed, and at high magnification the surface is seen to be relatively smooth.²⁶

The amount of hydrogen dissociation in the plasma core plays a large role in the growth of diamond.²⁶ The extent of this gas dissociation is governed by microwave power and pressure where hot and dense plasmas can form. At high pressure the plasma becomes more confined, whilst higher microwave power expands the plasma. It would be advantageous to use both very high pressure and MW power to grow diamond, to maximise the microwave plasma density, however this is limited by the equipment used, as at high temperatures the etching of the chamber walls can lead to silicon contamination.

1.4 Microwave Plasma Reactors

1.4.1 Microwaves and their uses

Microwave radiation is a form of non-ionising radiation that has a characteristic wavelength between the order of 1 mm to 1 m.²⁸ These microwaves are most commonly used domestically in microwave ovens as a means to heat up food through dielectric heating.²⁹ Microwaves have also been found to speed up reactions in organic synthesis such as the Diels-Alder reaction.^{30, 31}

1.4.2 Plasma

Plasma is a state of matter formed by the extreme heat that causes electrons to be ripped away from the atoms, forming a 'soup' of positively charged ions and electrons. Plasma makes up over 99% of the matter in the observable universe and is the constituent that makes up stars and nebulas, it's the glow from a strike of lightning, and the fluorescent light from neon signs. Plasma can be categorised into two different types, the first of which is thermal plasma, where there is a thermodynamic equilibrium between heavy ions and electrons, where it can be produced by electrothermal and electromagnetic launchers.^{32,33} Non-thermal plasmas have electrons that are much higher in temperature than its ions. These types of plasmas can be generated through continuous and pulsed dc discharges, microwave discharges, inductively coupled discharges and dielectric barrier discharges.³⁴ This report focuses on plasma generated via microwave discharges, as that is the method used in the synthesis of CVD diamond.

1.4.3 Microwave Plasma

Microwaves form part of the electromagnetic spectrum, where the type of radiation is defined part by its wavelength, which is on the same scale as the plasma reactor to be used in CVD diamond growth (2.45 GHz: $\lambda = 12.24$ cm). Non-thermal plasmas can be generated through microwaves at low pressure in a microwave plasma reactor. In the chamber of the reactor, there is a constant flow of gases, such as hydrogen, methane, and nitrogen. These gases contain a small number of ions due to interactions with radioactive radiation and cosmic rays. Thus, when an electric field is applied, these

ions are accelerated by the field and collide with neutral gas molecules, ionising them and thus creating more ions and electrons, which are themselves accelerated by the electric field. This causes a cascade of collisions to occur, forming a plasma.³⁵

For an intense electric field to be produced, the microwaves produced are generated at resonant frequencies that match those of the resonant cavity of the microwave plasma reactor (MWPR). There are two different forms of resonant modes for microwaves, the TE mode is when the electric field is orthogonal to the cavity axis, and the TM mode, when the magnetic field is orthogonal.³⁶ The notation used to describe the type of transverse mode (T stands for transverse), TM_{0mn} , describes first the symmetry of the electric field, the 0 denotes that the field is axisymmetric, i.e., a circular plasma is formed. The indices, m and n , indicate the number of lobes in the radial and axial positions respectively.

1.4.4 Plasma Induced Hydrogen Dissociation

An increase in pressure serves to decrease the size of the plasma ball, whilst an increase in temperature serves to increase the size of the plasma. The increase or decrease in the size of the microwave plasma can be viewed in terms of its volume, and hence a microwave plasma density (MPD), d , can be calculated:

$$d = P/4\pi r^3 \quad (1)$$

P is the microwave power and r is the radius of the plasma ball. Hydrogen molecules dissociate in a hydrogen only plasma – only through collisions with high energy electrons to form atomic hydrogen in a direct mechanism:



Thus, the electron density, n_e plays an important role in the rate of the dissociation of hydrogen, k :³⁷

$$k = k_d \cdot n_e \quad (3)$$

where k_d is the dissociation integral:

$$k_d = (8/\pi m_e)^{0.5} (k_B T_e)^{-1.5} \int_0^\infty \varepsilon \sigma(\varepsilon) \exp\left(-\frac{\varepsilon}{k_B T_e}\right) d\varepsilon \quad (4)$$

m_e is the mass of the electron, σ is the dissociation cross section of the excitation process, which is a function of the electron energy ε , and T_e , the electron temperature. Higher pressure causes the MPD, n_e , T_g and $[H]$ to increase whilst the T_e decreases as described in equation 4. This is confirmed by studying the atomic hydrogen concentration, as at higher atomic hydrogen concentrations in the plasma ball, the lower the amount of hydrogen incorporation into the diamond film.³⁸

1.4.5 Plasma Modelling

An objective of this thesis is to predict power outputs for the new Sairem magnetron for when it will be installed. A new power source should mean a more efficient one, where less power is lost in

transmission to the microwave cavity. More microwave power alters the plasmas characteristic properties such as its chemistry, MPD and, electron temperature. These values can be predicted using iterative models based off Maxwells equations.³⁹

For a plasma to form, the electron temperature must be high enough for ionisation of the gas mixture. For a typical hydrogen plasma, ionisation occurs at around 15 000 K, which has been calculated using a Maxwellian distribution function. Electron temperature is calculated by considering the balance of electron heating via the electric field, and the electron energy loss through collisions with gas molecules:³⁹

$$\frac{|eE_z|^2 n_e}{2m_e \omega} \frac{(v_m/\omega)}{1+(v_m/\omega)^2} \approx n_e N \kappa(T_e) \quad (5)$$

Whereby E_z is the local field amplitude at z , v_m is the momentum transfer frequency of collisions between gas particles and electrons, n_e is the electron density, ω is the wave frequency, T_e is the electron temperature, N is the gas particle density, and κ is the energy loss coefficient (units: energy x volume per litre). The left-hand side of the equation describes the power absorption density, whilst the right-hand side expresses the collisional power loss. By substituting $v_m = k_m N$ in (5) it can be gathered that at low gas pressures T_e is determined by E/ω , and at high gas pressures by E/N . When the plasma is ignited, N is large and so more energy is needed to ignite the plasma than to sustain it, since N is smaller after the ignition. This explains the observation that plasmas can exist at powers lower than its ignition power.

A two-dimensional self-consistent model allows for a more detailed approach to find out about how the plasma interacts with the electric field. The model considers both the axial and radial dimensions of a cylindrical cavity, where the EM fields are calculated from Maxwell's equations. The microwaves are modelled, considering only the TM mode, and the components E_ϕ , H_r (radial), and H_z (axial) are zero. The time-averaged power-deposition profile is given by:³⁹

$$P = -C \frac{en_e \omega}{2\pi} \int_0^{2\pi} \mathbf{V}_e \cdot \mathbf{E} dt \quad (6)$$

Where C is a normalisation constant, so that the volume integral of P adds up to total power. The EM fields, \mathbf{H} , \mathbf{E} and \mathbf{V}_e are calculated from Maxwells curl equations:³⁹

$$\mu_0 \frac{\partial \mathbf{H}}{\partial t} = -\nabla \times \mathbf{E} \quad (7)$$

$$\varepsilon_0 \frac{\partial \mathbf{E}}{\partial t} = \nabla \times \mathbf{H} + en_e \mathbf{V}_e \quad (8)$$

K.Hassouni *et al* have used these equations to help model hydrogen plasmas for a variety of microwave powers and pressures (figure 11).⁴⁰ The models show that the plasma expands, and the gas temperature increases with an increase in microwave power, whilst the electron count stays roughly the same, these are consistent with equations 2 and 4. Knowing the hydrogen density over a range of powers can be used to predict growth rates of diamond film when comparing to experimental data, and this is shown in section 2.2.

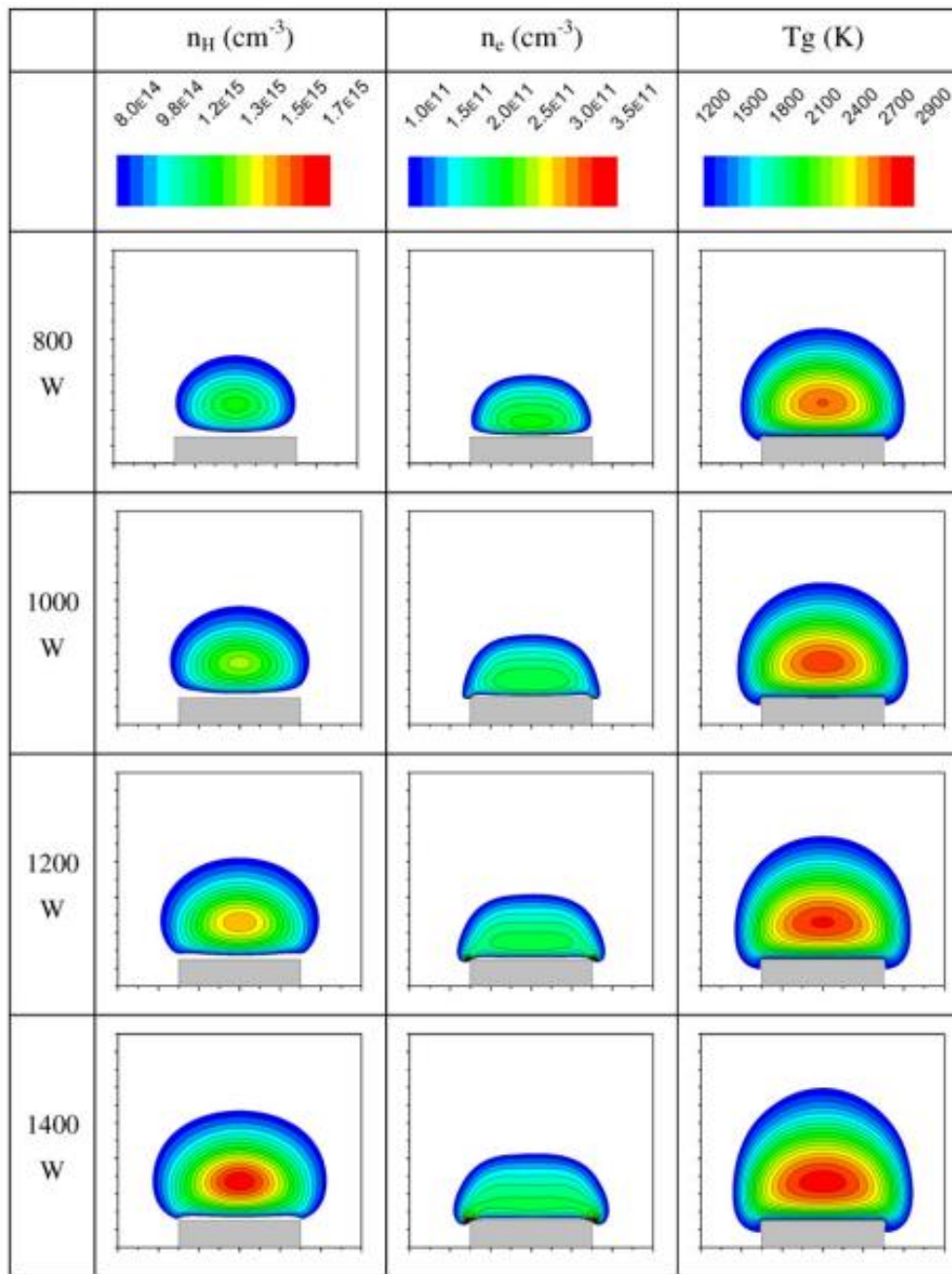


Figure 11: Distributions in the n_H , n_e and T_g are shown to change as microwave power changes. These plots are computed at 38 torr.⁴⁰

1.5 The Construction of Microwave Plasma Reactors

We have already considered some growth parameters that lead to making high quality diamond. High MPD is essential in ensuring that high hydrogen atom concentration is achieved, which can then lead to high growth rates. A fundamental part of the reactor is the microwave-to-plasma applicator as this is the component that defines the amount of energy being sent to the plasma. Thus, it can tune the MPD by monitoring the pressure, power, and frequency.⁴¹ An advantage of microwave discharges (MD) is that the electrodes are not susceptible to erosion due to the negligible bombardment of ions on the electrode surface, and this prevents the chance for contamination of

the plasma. A microwave plasma reactor is composed of many parts which converts electricity into microwaves (of the same mode) that are directed into a cavity to generate a plasma. A general scheme for the structure of reactors can be seen below (figure 12).

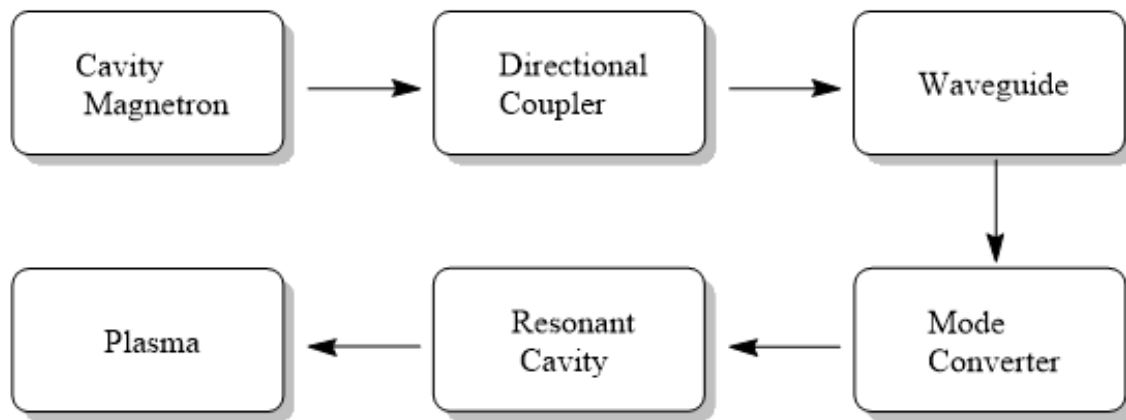


Figure 12: A flow chart showing the pathway for microwaves plasma generation.

1.5.1 Magnetrons

The cavity magnetron was invented in the autumn of 1940, early into the second world war, by a British team, led by Sir Henry Tizard.⁴² Two physicists named, Henry A. Boot and John T. Randall were those who developed the cavity magnetron at the British General Electric Laboratory in Wembley. This technology was sent to the United States where it would be used in high-power pulse-modulated radar systems. Two billion dollars was invested into further developing the cavity magnetron, and this proved to be crucial in the successful war effort by the allies.

The underlying physics behind the functioning of the cavity magnetron is LC oscillation. The L and C represent an inductor and a capacitor respectively, and, when connected, can act as an electrical resonator (figure 13). The voltage across the capacitor drives a current through the inductor (in this case it's a coil). Once the voltage of the capacitor reaches zero, the energy from the magnetic field in the coil induces a voltage which causes a current to flow in the opposite direction. This recharges the capacitor, and the process repeats itself, only now the initial current flows in the opposite direction to the first time. This oscillation of the back and forth current, has a natural frequency to it, and if the applied current has the same frequency as the circuit's natural resonant frequency, resonance will occur. If an antenna is placed next to the inductor, the magnetic field of the coil in the LC circuit induces a current to flow in the antenna, and the resultant voltage causes electromagnetic waves to be produced.

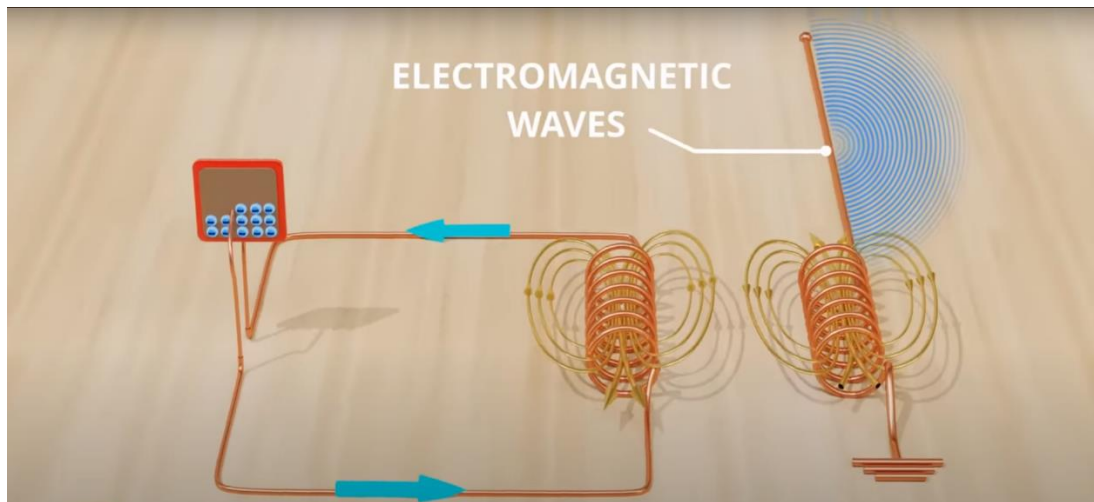


Figure 13: A diagram showing an LC circuit.⁴³ The left red box is the capacitor, and the coil on the right is the inductor. Adjacent to the circuit is an antenna, where a magnetic field causes a voltage to be produced, which in turn radiates electromagnetic waves.

These electromagnetic waves can be harvested efficiently in magnetrons through thermionic emission. Let's suppose we have a cathode and a filament system, where a current flows through the filament heats the cathode. Electrons are released from the filament, and if an anode is placed around this system, the electron will move towards it. The acceleration of the electrons towards the anode produces radiation. However, this process is inefficient as the electrons spend little time in the interaction space (the space between the filament and the anode). So, a magnet is placed either side of this system (figure 14), and this slows down the electron in the interaction space, making radiation more efficient. This system is known as the hull magnetron, but this can be improved even further when utilising LC oscillations.

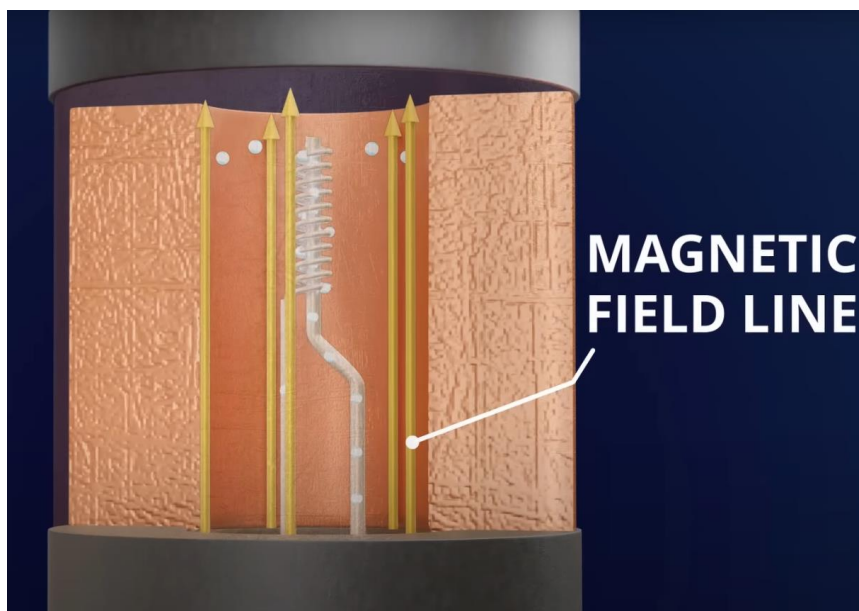


Figure 14: This diagram shows a side on view of the hull magnetron.⁴³ A magnetic field is present, and this affects the path of the electrons as they move around interaction space before striking the anode.

The cavity magnetron, as the name suggests, contains cavities, and these cause induced currents to flow around the anode. When an electron strikes the anode next to the cavity, electrons in the anode move across the cavity as to invoke a current.⁴⁴ This current which forms around the cavity acts as an inductor, notice how now we have the components for an LC circuit. The cavity as the inductor, and the induced charge at either side of the cavity as the capacitor. The axial magnetic field exerts a force on the radially moving electrons, and they travel to negatively charged areas at the cavities. Since these electrons are being ‘swept’ around the cavity, the charges are pushed around, giving energy to the oscillations at the resonant frequency of the cavity (equation 9, figure 15).⁴⁵ An antenna is placed on one of the cavities which converts the oscillations to electromagnetic radiation in the form of microwaves. Since the electrons are constantly moving around the cavities, the energy collected from one cavity is the same as all others combined.

$$f_{resonance} \approx \frac{1}{2\pi} \sqrt{\frac{1}{LC}} \quad (9)$$

Where L is inductance, and C is capacitance.

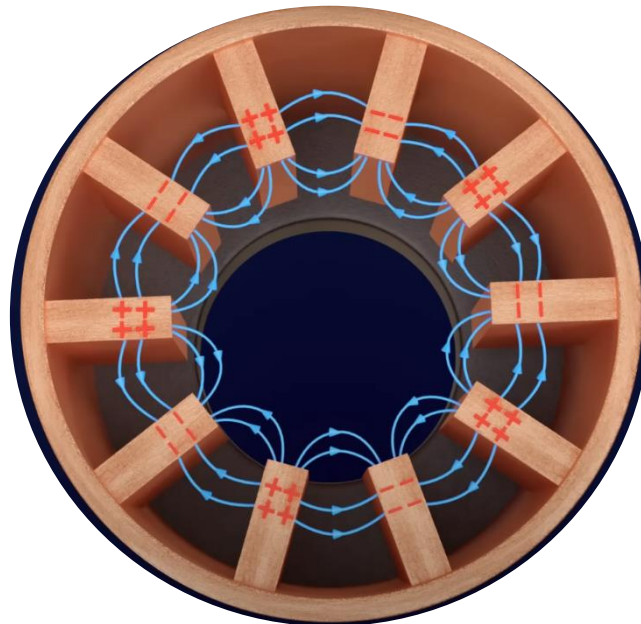


Figure 15: This diagram shows the cavity magnetron.⁴³ The arrows which move around the cavities, denote the flow of electrons. These change in direction and strength as the induced charge changes. The oscillations of the electrons around the cavity resonate at the resonance frequency of the cavity.

1.5.2 Directional Couplers

Directional couplers are used as a means to prevent reflective power entering back into the magnetrons cavity.⁴⁶ They are made up of two components, a primary waveguide (port 1-2), and a secondary waveguide (port 3-4) (figure 16). Because of how the coupler is made, there is no reflection of power between port 1 and 2, and no transmission of power between port 1 and 3 or between port 2 and 4 since no coupling exists. A coupling factor defines the ratio of power levels between the first and secondary waveguide lines. Thus, a known coupling factor can be used to

measure the power at the input port by measuring the power at port 4, through the following equations:⁴⁶

$$C_f = 10 \log_{10} \frac{p_1}{p_4} \quad (10)$$

$$D = 10 \log_{10} \frac{p_4}{p_3} \quad (11)$$

Where C_f is the coupling factor in decibels (dB), D is the directivity (dB), and P_n is the n port. This is useful when changing magnetrons and comparing their power output, which is a focus of this report.

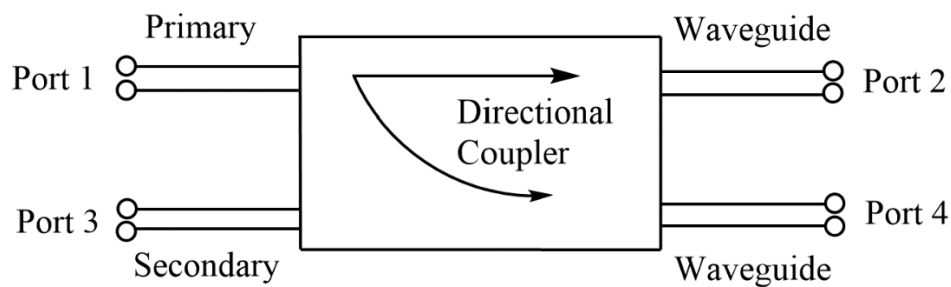


Figure 16: This diagram shows how a directional coupler works; to ensure unidirectional transmission of microwave power.

1.5.3 Waveguides

Waveguides are a form of transmission line that are used to transport microwave signals from the cavity magnetron to the reaction vessel, though minimal loss of energy by restricting the wave to one direction. They are generally made from metals (such as silver), or alloys of metals have low bulk resistivity such as brass. The waveguide can propagate TM and TE modes since one conductor is present. Rectangular, circular, and coaxial waveguides have been produced, where the shape determines the resonant frequency of the cavity (Figure 17).⁴⁷ The cut-off frequency, f_c , is the lowest frequency for which a wave will propagate in the waveguide. There can be many modes that the waveguide can propagate (i.e., TE_{10} , TE_{20} , TM_{01} etc), but this can be troublesome, as if there are many modes are propagating, the waveguide is said to be *overmoded*, and this can result in attenuation. Thus, the dimensions of the waveguide are chosen carefully, so that only the dominant mode propagates (the dominant mode is the mode that has the lowest cut-off frequency).

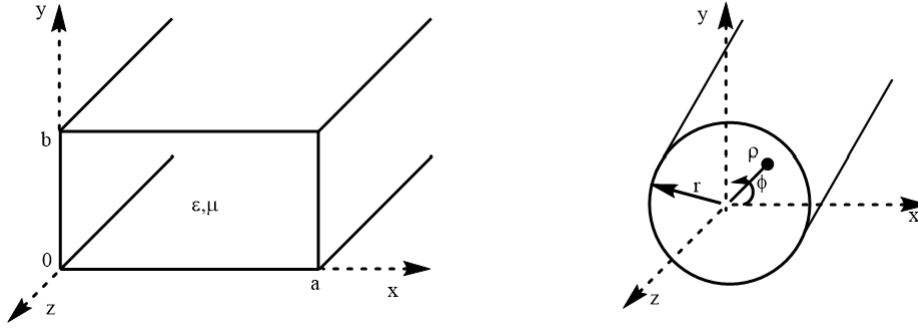


Figure 17: The diagram on the left shows the dimensions for a rectangular waveguide. The diagram on the right shows the dimensions for a cylindrical waveguide. Note the change to polar coordinates when looking at the cylindrical waveguide, where ρ is at an arbitrary distance to a turning point of an arbitrary wavefunction.

For a rectangular waveguide in the TE mode, the $f_{c,mn}$ is given by:⁴⁷

$$f_{c,mn} = \frac{1}{2\pi\sqrt{\mu\epsilon}} \sqrt{\left(\frac{m\pi}{a}\right)^2 + \left(\frac{n\pi}{b}\right)^2} \quad (12)$$

Where the hollow waveguide is made from a material of permittivity ϵ and permeability μ . The dimensions of a waveguide are such that the longest side points along the x-axis, hence $a > b$, and m and n describe the modes of the wave. The dominant mode is one where $a > b$, thus the lowest f_c occurs for the TE₁₀ mode ($m=1, n=0$):⁴⁷

$$f_{c,10} = \frac{1}{2a\sqrt{\mu\epsilon}} \quad (13)$$

Note how there is no TE₀₀ mode as this would mean that the electric field component \hat{E} , and the magnetic field component \hat{H} (from maxwells equations), are zero when m and n are zero.⁴⁶

For TM modes in a rectangular waveguide, the f_c is TM₁₁, and this is because \hat{E} and \hat{H} are zero if either m or n are zero. Therefore, TM₀₀, TM₀₁, and TM₁₀ modes are not possible. So, $f_{c,11}$:

$$f_{c,11} = \frac{1}{2\pi\sqrt{\mu\epsilon}} \sqrt{\left(\frac{\pi}{a}\right)^2 + \left(\frac{\pi}{b}\right)^2} \quad (14)$$

This has a higher cut-off frequency than the TE₁₀ mode, and so TE₁₀ is the dominant mode for rectangular waveguides.

For circular waveguides spherical coordinates are used as seen in figure 17. The TE modes are determined by the cut-off wavenumber, $k_{c,nm} = \frac{\rho'_{nm}}{a}$, where n is the number of circumferential variations, and m is the number of radial (ρ) variations, and a is the point at which \hat{E} is zero. The cut-off frequency is:

$$f_{c,mn} = \frac{k_c}{2a\sqrt{\mu\epsilon}} \quad (15)$$

The smallest ρ' is the first TE mode to propagate, and this is found to be from the TE₁₁ mode, which has a value of 1.841.

The first TM mode to propagate in a circular waveguide is the TM₀₁ mode, where $\rho_{01} = 2.405$:

$$f_{c,mn} = \frac{k_c}{2\pi\sqrt{\mu\epsilon}} \quad (16)$$

Here, $k_c = \rho_{nm}/a$, and since $2.405 > 1.841$, the dominant mode in the circular waveguide is TE₁₁.

1.5.4 Waveguide Mode Converters

The magnetron at the University of Bristol initially produces a TE₁₀ mode which travels through a rectangular waveguide, and this is the dominant mode for the waveguide system. In a circular waveguide, the dominant mode is TE₁₁, but the mode that has the next lowest cut-off frequency is the TM₀₁ mode. TM modes are used in microwave cavities over TE modes because the plasma is formed over the substrate and not in contact with the cavity's walls. Thus, the TM₀₁ is the desired mode used in microwave plasma reactors. There are two problems associated with using the TM₀₁ mode. The first is that a mode converter is required to convert the TE₁₀ mode to the TM₀₁ mode. Secondly, since the TE₁₁ mode is the dominant mode in a circular waveguide, and the TM₀₁ mode is the desired mode, there therefore must be some way to prevent the propagation of the unwanted modes.

The converter works through first introducing the wave into a cylindrical waveguide, that has a small radius, from the rectangular waveguide.⁴⁸ This preferentially selects the TM₀₁ and TM₁₁ modes and cuts off all other modes. Convex slots are introduced at the rectangular waveguide which suppresses the TE₁₁ mode but allows for the transmission of the TM₀₁ mode as seen in figures **18** and **19**. The slots affect how the microwaves propagate within the waveguide by altering the distance travelled. Thus, the undesirable microwave modes cannot resonate with the resonance frequency of the waveguide, and therefore cannot travel efficiently. Other groups have used similar methods to the one just stated where the rectangular waveguide is joined head-on to the cylindrical one.⁴⁹ What is apparent however, is the use of different frequency microwaves, where 1.75 GHz, 2.45 GHz and 12.5 GHz waves in the literature have been seen.⁵⁰ Different frequencies require differently sized waveguides, and the solutions of these problems can be modelled computationally using CST microwave studio.

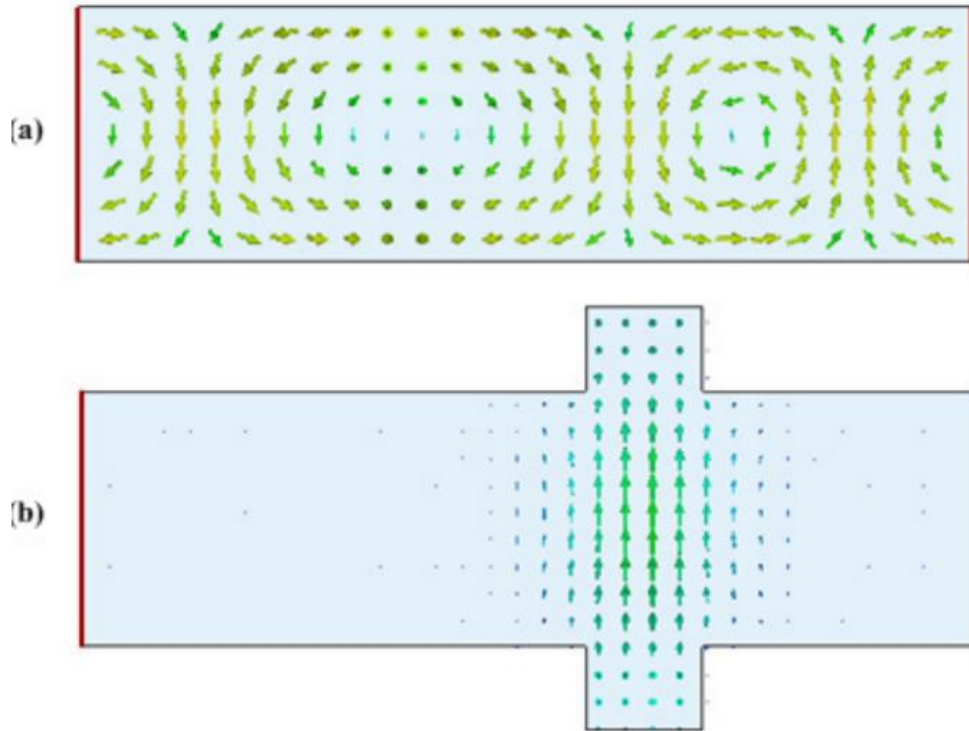


Figure 18: Two top view images of a rectangular waveguide showing the direction of the magnetic field when the circular TE_{11} mode is generated from the circular waveguide: (a) this image is showing the propagation of the TE_{11} mode in a rectangular waveguide before the convex slots have been added; (b) another top view image, but this time convex slots have been added. The TE_{11} mode cannot propagate, and the magnetic field is suppressed either side of the slots.⁴⁸

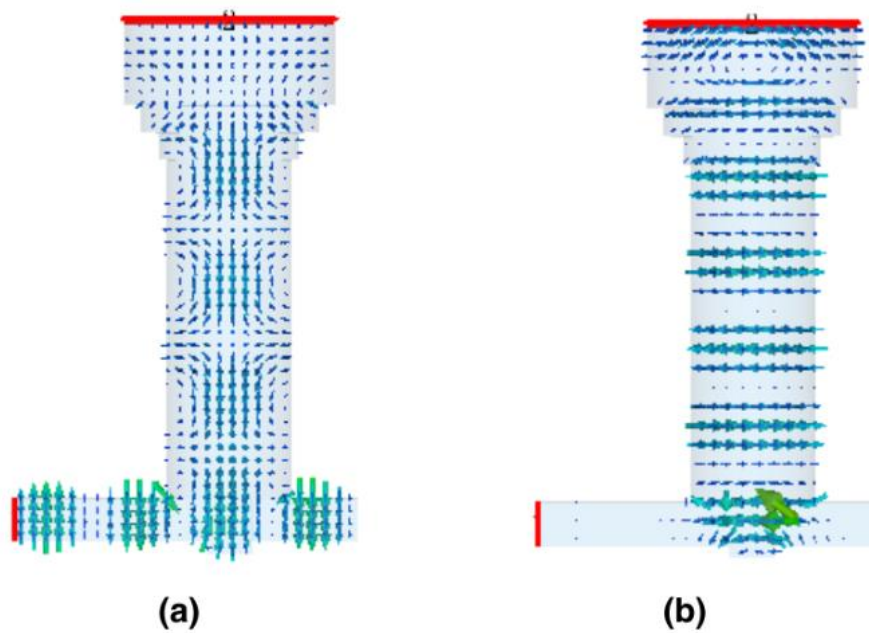


Figure 19: Rectangular to cylindrical mode converters showing their respective electric fields when injected with (a) the TM_{01} mode and (b) the TE_{11} mode. The waves were fired from the cylindrical

port, and the mode that circulates in the rectangular waveguide is the TM_{01} mode and not the TE_{11} mode.⁴⁸

1.5.5 Resonant Cavities

Resonant cavities are chosen for the construction of MWPRs for a few reasons. Resonant cavities can ignite plasmas much easier since they are able to hold a higher electric field when excited at their resonant frequency.³⁶ The MWPR to be used in the growth of CVD diamond in this thesis uses a TM_{001} mode (figure 20) that was converted by a waveguide from the TE_{010} mode, and this is made by ASTeX (now called SEKI Technotron).^{51,52} Other types of TM modes have been used by other groups including TM_{20} , TM_{21} , $TM_{1(1-4)}$ and TM_{11} .^{53,54,55,56} The TM_{21} mode was used by the group at the University of Science and Technology in Beijing where they reported that two-inch diameter and 460- μm -thick free-standing diamond was synthesised at 6 kW microwave power. Transverse electric fields are not used often in MWPRs as the as the field is normal to the substrate, which means that the field regions contact the chamber walls, and the plasma formed won't be in contact with substrate.

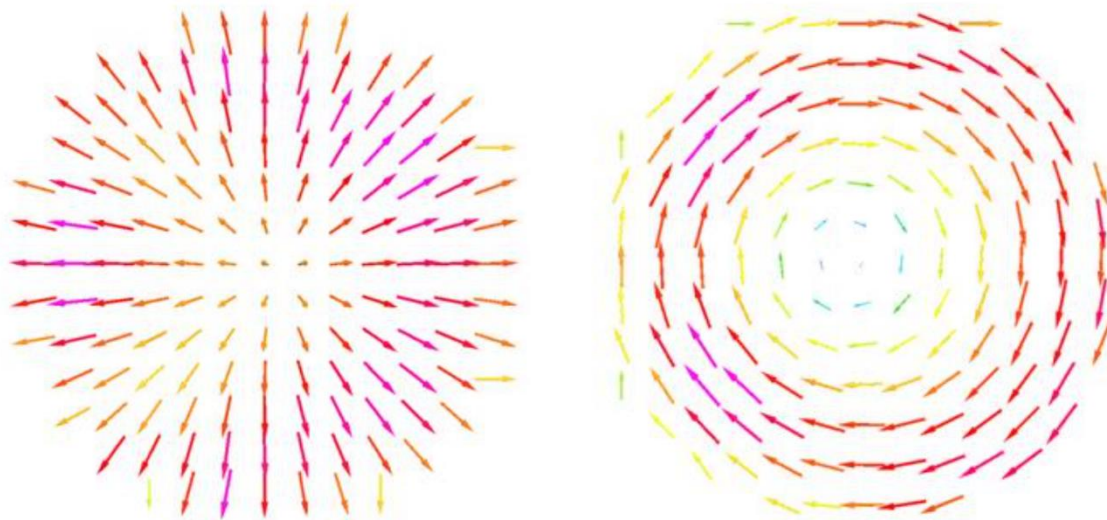


Figure 20: The left and right images are the respective cross-sections of the distribution of electric and magnetic fields for the TM_{01} mode in a circular waveguide.⁵²

For the MW energy to be efficiently transmitted from the magnetron to the plasma, coupling techniques must be used to do so. A resonant mode, either in the electric or magnetic window must be excited in which the resonant mode shares a component with the cavity mode that will be excited. Electric-field coupling can be achieved through using antennas as seen in figure 21 for the TM_{012} resonant cavity mode.³⁶ Magnetic coupling uses magnetic loops or slots on the cavity walls to induce the magnetic field to point in the same direction as the mode of the cavity to be excited.

Magnetic coupling is limited by its lower power transmission of up to 100 W and thus electric coupling is the most chosen coupling technique for plasma reactors.

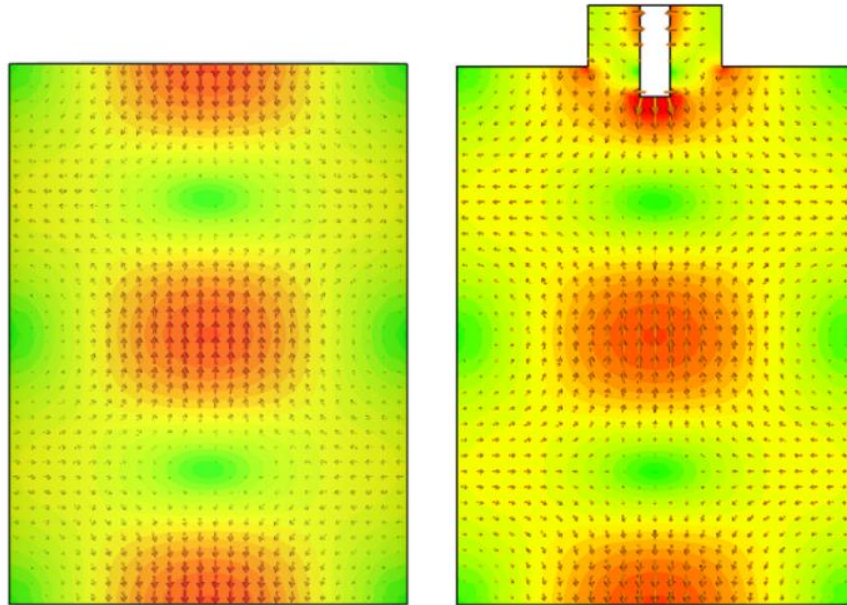


Figure 21: Both diagrams illustrate the direction of the electric field in the same direction as the cavity mode field, with (right) and without (left) an antenna. The electric coupling technique is used with the TM_{012} mode in a cylindrical cavity.³⁶

The choice of dielectric window is an important consideration when designing a resonant cavity MWPR. The reactor used in the experimental section in this thesis has a dielectric window made of quartz, which is piezoelectric and has a high temperature resistance. The need for a window is obvious when considering the electric field in figure 21. Without a window the whole cavity will contain low pressure gas and the plasma will be ignited in all the regions of the intense electric field, including those produced near the antenna.³⁶ The use of a quartz window vacuum seal, which separates the atmospheric pressure, ambient air, and the antenna from the low-pressure process gases, allows the electric field to be intense in only one region and away from the chamber walls. Hence, the only position where a plasma can form is directly above the substrate.

The design principle for the addition of a quartz window can be rationalised in figure 22, whereby an ASTeX reactor is shown using a TM_{013} mode. This is similar to the cavity used at the University of Bristol diamond labs, the quartz window reduces the pressure in the chamber and confines the flow gases, hence a plasma only forms above the substrate and not where there is just an intense electric field.

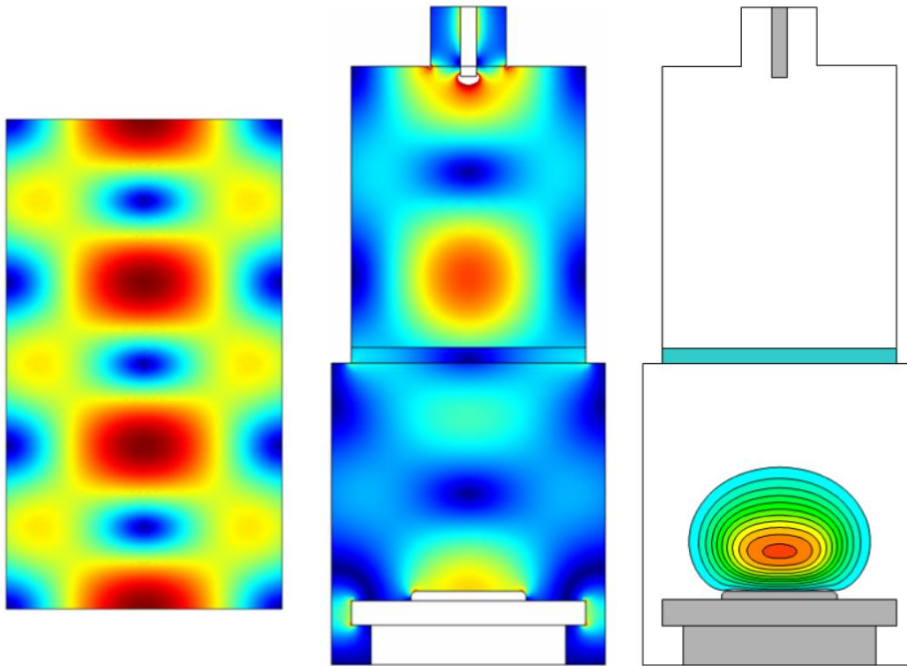


Figure 22: This is a diagram showing the evolution of design for an ASTeX reactor using a TM_{013} mode. The left image has the electric field show when no antenna and quartz plate is used. The middle image does have those features mentioned, with the region above the quartz plate at atmospheric pressure and that below it at low pressure. The right picture is a model of a 200 mbar H_2 plasma.³⁶

Another consideration with regards to the resonant cavity is its shape. Exxelia Temex are manufacturers that develop resonators, they offer disk, cylindrical, square and rectangular shaped resonant cavities.⁵⁷ Cylindrical cavities are the most common shape seen in the literature, as they can support a wide range of TM modes.⁵⁸ There are three MWPR at Michigan State University which all use cylindrical cavities in the TM_{103} , TM_{013} and TM_{202} modes.⁵⁹ Other than those shaped cavities mentioned, the ellipsoidal cavity has attracted attention for its ability to both stabilise plasmas more effectively and to withstand greater MW powers.⁶⁰ AIXTRON, a German technology company that was founded as a start up from RWTH Aachen University in 1983, were first to manufacture an ellipsoid egg-shaped cavity.⁶¹ The basis for the creation of these cavities was the idea that in an ellipse, two focal points would be created where the strong electric field would be contained. The addition of an antenna would block one of these points and thus a single plasma would form at one end of the cavity (figure 23).

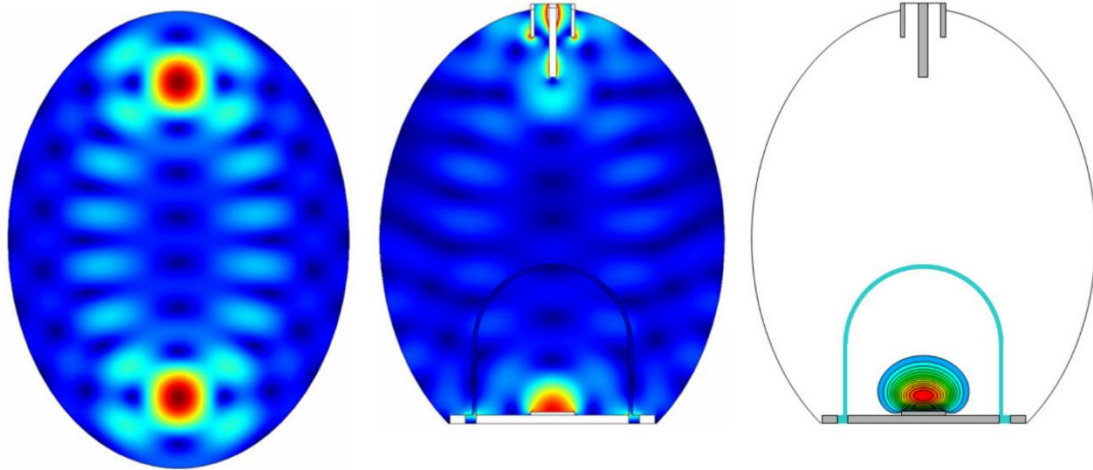


Figure 23: An ellipsoidal shaped cavity produced by AIXTRON. There are two foci of the electric field in the TM_{036} mode shown in the left panel, with the addition of an antenna in the central panel. On the right panel, a 200 mbar H_2 plasma is shown.³⁶

The frequency of the microwave used influences the deposition area of the diamond. Lower energy 915 MHz microwaves can increase the deposition area by up to 4.5 times. This makes it more attractive for commercial usage.³⁶

1.6 Examples of Microwave Reactor Setups

1.6.1 The iPLAS Reactor

A company named iPLAS (innovative plasma systems) have developed microwave plasma systems for over 25 years, and a number of research groups across the world have used their technology for the growth of CVD diamonds.⁶² Figure 24 shows the magnetic fields produced from a toroidal waveguide in the TM_{12} mode.³⁶ This reactor has been designed so that the waveguide is the same length as four microwaves, and the slots are positioned every half wavelength (hence there are eight intense regions in red). A cross sectional image (24 b) shows the regions of the magnetic field at the point the microwaves are released into the resonant cavity. At the centre, the microwaves are transferred into the cavity (24 a), where a tube is used to prevent plasma forming at the slot's location. The iPLAS reactor has been used to create microplasma deposited nanodiamond structures by reactive ion etching, and laser nanoablation of diamond films.^{63, 64} The utilisation of the iPLAS reactor for nanoscale diamond processes can be owed to its moderate power and the use of a TM_{12} mode which makes for a shorter wavelength. This produces a small, hemispherical plasma as seen in figure 25.

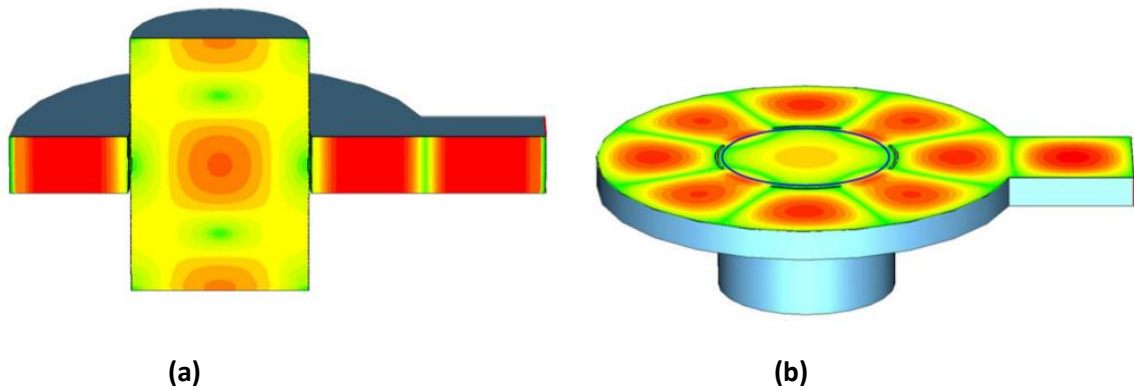


Figure 24: A diagram showing the intensities of the magnetic field from a TM_{12} mode in a cylindrical mode of an iPLAS type reactor. The right image is a cross sectional picture of the left image, and this can be seen in the four intense regions across the centre of both pictures.³⁷

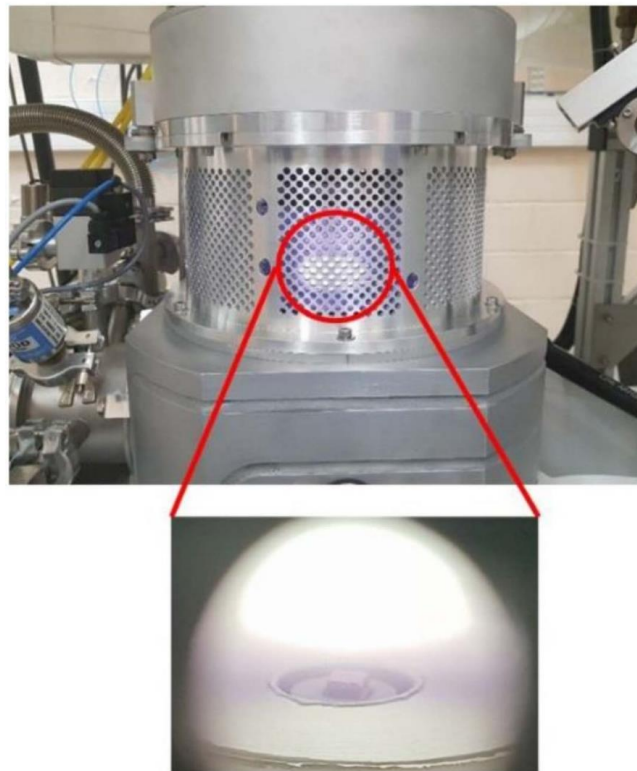


Figure 25: These images show what the iPLAS reactor and the plasma generated look like. An intense, hemispherical plasma forms over the substrate.⁶⁵

1.6.2 The NIRIM Reactor

The National Institute for Research in Inorganic Materials (NIRIM) in Japan have made important progress involving CVD diamond since the 1980s.⁶⁶ The MWPR designed by the NIRIM group was made commercially available, and this allowed research groups across the globe to experiment with plasma CVD. The waveguide system (including the magnetron) is sourced from a radio and micro

frequency technology company called Sairem. All of the microwave components used are part of the WR340 series by Sairem. The reactor uses a 2.45 GHz rectangular waveguide (suitable for a TE₁₀ mode), which is attached to a quartz vacuum tube (figure 26). The microwaves pass through an isolator and an arc deflection flange, 'I', to minimise the reflected power returning to the magnetron. Three tuning stubs, 'K', are used to minimise the reflected power by matching the impedance of the discharge tube. The microwaves pass through a quartz window, into a cylindrical cavity, where a plasma is ignited from free electrons in the gas mixture. One disadvantage of the NIRIM reactor is that the substrate temperature cannot be independently controlled since the plasma engulfs the substrate.⁶⁷ This has consequences when altering the power and pressure output of the reaction conditions. The substrate will have different amounts of contact with the plasma due to the plasma changing in size, and thus, there will be an inconsistency in plasma temperature when growing at different conditions.

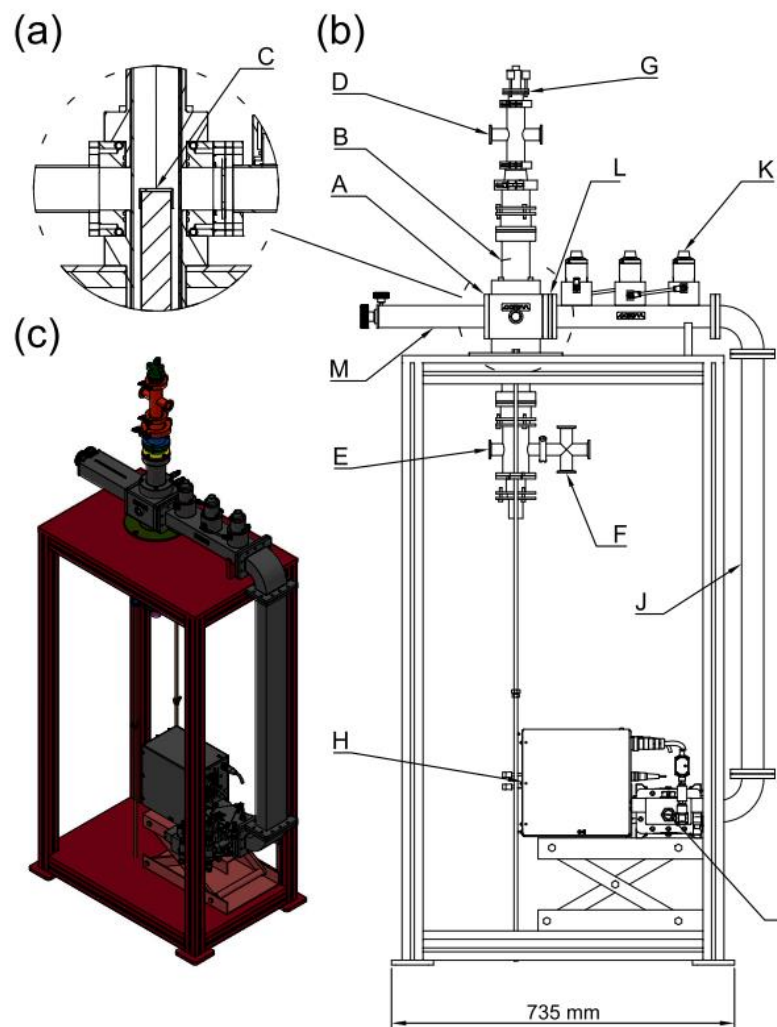


Figure 26: An overview of the NIRIM reactor. (a) A zoomed in cross-sectional image of the substrate holder, (b) Is a side view of the reactor and its important components, and (c) a computer image of the reactor. The lettering system can be summarised in the table 1.⁶⁶

Table 1: Summary of the components that make-up the NIRIM type reactor

A	Water cooled cavity
B	Interchangeable chimney
C	Ceramic sample holder
D	Reducing cross
E	Flange for mating to vacuum components
F	KF25 cross
G	Pyrometer and quartz window
H	2 kW 2.45 GHz magnetron
I	Isolator and arc detection flange
J	WR340 waveguide
K	Tuning stubs
L	Quartz window
M	Sliding short-circuit

1.6.3 The Seki-ASTeX Reactor

The Seki-ASTeX reactor design (a manufacturer based in USA of plasma systems) deals with the problems associated with the NIRIM reactor. The plasma ball hovers over the substrate and isn't in contact with the microwave cavities walls. This allows for the substrate temperature to be independently controlled using a cooling plate underneath the substrate holder (Figure 27). A uniform plasma over the substrate is required to grow uniform, homoepitaxial diamond film. Hence, the need to build a device to create an axisymmetric plasma is essential to achieve this. A rectangular waveguide is used to propagate microwaves in the TE₁₀ mode, and this is connected to a switchable cylindrical waveguide where different diameters are available. Differently sized waveguides are able to hold different TM modes (TM₀₁, TM₀₂, TM₀₃, are used), an increase in the number of radial nodes can be utilised for processing larger or multiple substrates, since a large plasma can form. High quality, homoepitaxial diamond film, grown using an ASTeX-Seki reactor design has been found to create hillock-free surfaces.⁶⁸ The ability to use different frequency microwaves also gives the ASTeX-Seki an advantage against other reactor designs forementioned. Decreasing the microwave wavelength to 915 MHz from 2.45 GHz, allows for diamond films with diameters of 150 mm to grow when using 60 kW of microwave power.⁶⁹

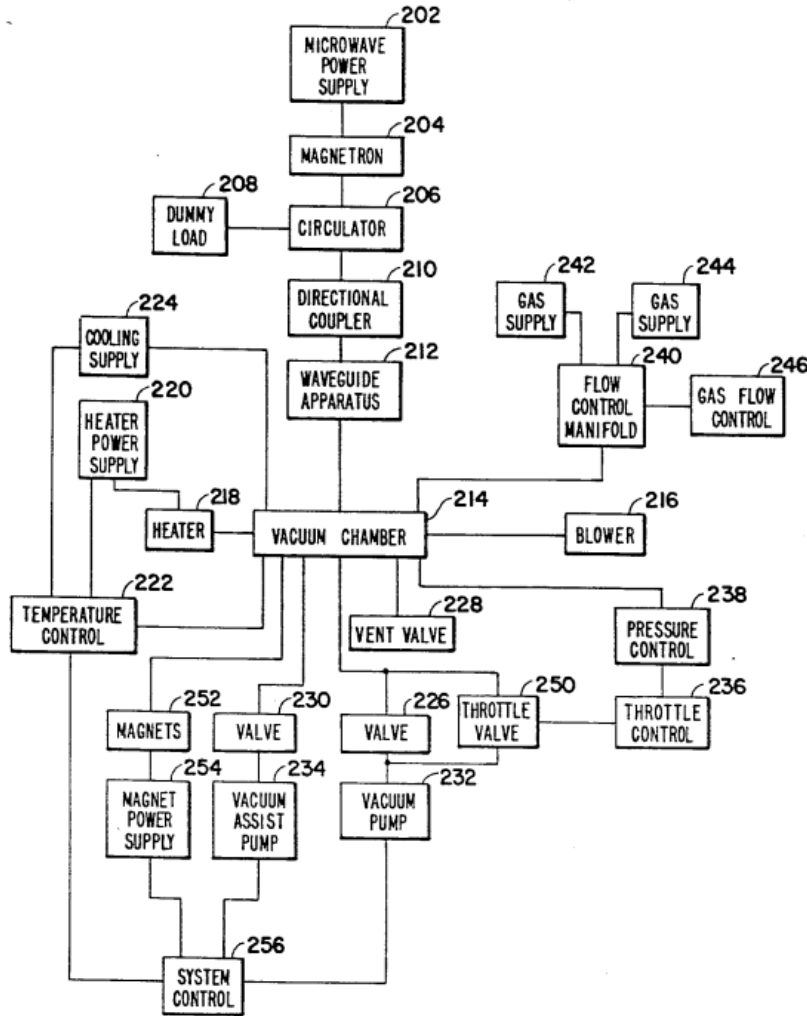


Figure 27: A map of an ASTeX-Seki reactor design.⁷⁰ A circulator is used to prevent magnetrons from being damaged by any reflected power, by directing the transmission into a dummy load.

1.6.4 Summary of other MWPRs

Table 2: A summary of some research groups around the world, the manufacturers of the microwave plasma reactors, and the details of CVD diamond growth.

Group of Researchers	Type of MWPR	Substrate T (°C)	TM mode	Cavity shape	Microwave frequency	Coupling method	Characteristics of diamond grown
Fraunhofer Institute for Applied Solid State Physics ^{36,61,71}	AIXTRON	950	001, 012, 036	Ellipsoidal	2.45 GHz	Magnetic – using antenna system	MCD, PCD
School, of Physics, University	iPLAS	975	012	Cylindrical	2.45 GHz	Magnetic – using slots	SCD, NCD

of Melbourne 72							
Michigan State University, USA ^{36,49,73}	ASTeX/SEKI	950-1300	103, 013, 202	Cylindrical	2.45 GHz	Electric	Various
LIMHP, France ^{36,} 72,73	LIMHP/ PLASSYS	800-1000	022	Cylindrical	915 MHz, 2.45 GHz	Magnetic – using antenna system	Small to large area deposition (up to 16cm diameter (at 915 MHz))
University of Bristol	Element Six, Ltd/ ASTeX	900	001	Cylindrical	2.45 GHz	Electric	MCD, PCD

1.6 Characterisation Techniques:

1.6.1 Raman Spectroscopy

Raman spectroscopy is a powerful technique for the characterisation of various carbon allotropes, such as diamond, graphite, fullerenes, nanotubes and amorphous carbon films.⁷⁴ Materials made mostly out of covalent bonds with small to no dipole moments are perfect candidates for Raman spectroscopy, whereby tiny changes in the structure can be detected accurately. Peaks of sp^3 and sp^2 carbons can be distinguished in Raman spectroscopy since they have distinct peaks – table 3.⁷⁵ Laser beams in the visible, near-IR or near-UV region of the EM spectrum are shone at the sample, vibrationally exciting the structure, which puts the molecule into a virtual energy state before a photon is emitted. Due to inelastic scattering, the photon energy may be higher or lower in energy than the initial excitation photon. A Stokes shift is when the photon is in a lower energy state, an anti-Stokes shift is when the photon is lower energy, and as for Rayleigh scattering, there is no change in the photon energy before and after collision with the sample. Thus, for the energy of the system to be conserved, the molecule must move to a new rovibronic state.

Table 3: Common Raman peaks observed in CVD diamond:

Position (cm^{-1})	Typical FWHM (cm^{-1})	Assignment
520	3-5	first-order silicon Raman peak
1100-1150	40-80	Could potentially be transpolyacetylene at grain boundaries ⁷⁶
1332	5-10	first-order diamond Raman line
1345	250	sp^2 amorphous carbon – the D peak
1430-1470	80	Could potentially be transpolyacetylene at grain boundaries
1520-1580	100	sp^3 amorphous carbon - the G peak

The peaks described in table 3 can be shown visually through the Raman spectra below (figure 28). The FWHM indicates the broadness of the peaks, the metric measures the width of the peak at half of its maximum amplitude. A large G peak indicates low quality diamond due to the presence of a high amount of sp^2 carbons from amorphous carbon.

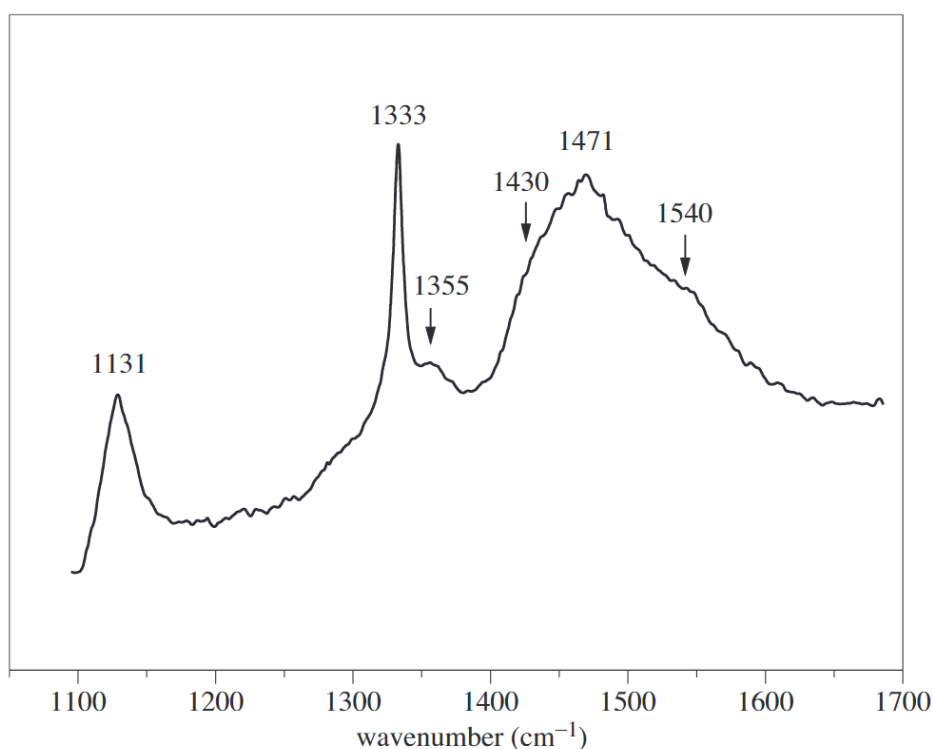


Figure 28: A Raman spectra of CVD diamond film, grown on a Mo substrate at 820 °C.⁷⁵

1.6.2 Optical Emission Spectroscopy

To understand the plasma chemistry, optical emission spectroscopy (OES) can provide useful data that can characterise the composition and intensities of gases in the plasma. Sophisticated OES systems can map the whole plasma region, showing how the gas mixture changes with distance from the substrate (known as spatially resolved OES (SR-OES)).⁷⁷ Other systems, such as the one used in the OES collected in the experimental section of this report, collects data at a single point in the plasma, and hence only provides information of the gas composition at a distance, x , from the substrate. The microwave power is mostly used on heating the gas mixture, exciting H_2 and C_2H_y species (where $y = 0-6$). High energy H atoms take part in H addition and abstraction reactions which causes CH_4 to react, forming a variety of other species. The distribution of some of the species present in the plasma are summarised in figure 29 as a distribution of their radial (r), and axial (z), distances from the plasma.⁷⁴ The intensity of the transitions occurring in a CH_4/H_2 plasma are shown in the OES in figure 30, and a table of these transitions shown in table 4.⁷⁸ The most intense peak is the C_2 ($d^3\pi_g \rightarrow a^3\pi_u$) transition at 516.52 nm, which is evidenced by the plasma's strong green colour when increasing the methane concentration. The intensity of the peaks in OES does not relate to the amount of that species present, but is a facet of the strength of the electronic transition occurring. Thus, OES is best used for qualitative purposes and not a quantitative spectroscopic method.

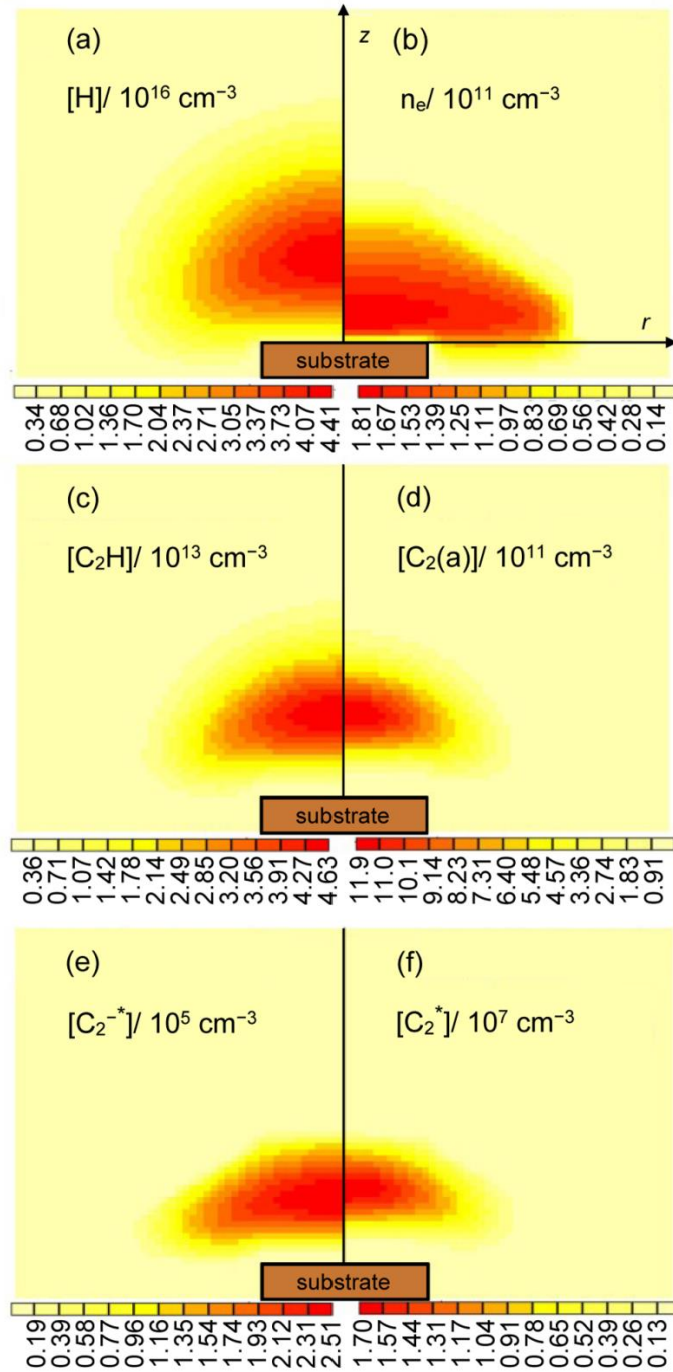


Figure 29: Density distributions of a variety of species that make up a CH_4/H_2 plasma (H_2 flow rate is 300 Sccm, $\text{CH}_4 = 19$ Sccm). In this system, the vertical distance from the substrate to the quartz window at the top of the reactor is 5.7 cm, and the reactor radius is 6 cm.⁷⁷

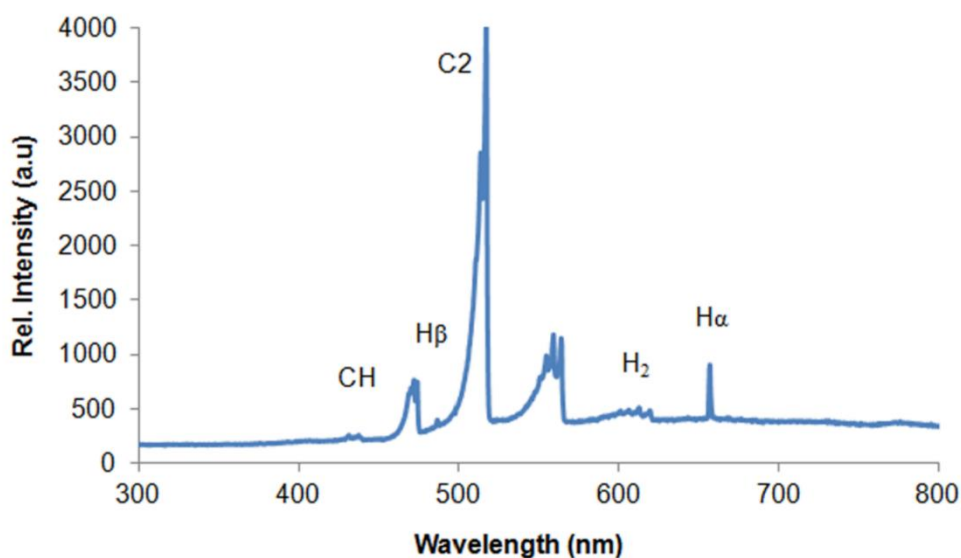


Figure 30: OES of a microwave plasma at 5% CH₄/H₂, 135 Torr and, 3.5 kW microwave power.⁷⁸

Table 4: Shows the species present in plasma, the electronic transition occurring, and the wavelength of light emitted during electronic transition in a CH₄/H₂ plasma.⁷⁸

Excited species	Electronic Transition	Peak position (nm)
CH	$A^2\Delta \rightarrow X^2\Pi$	431.15
H γ	$n^{\prime} = 5 \rightarrow n = 2$	436.85
C ₂	$d^3\Pi_g \rightarrow a^3\Pi_u$	471.55
H β	$n^{\prime} = 4 \rightarrow n = 2$	486.31
C ₂	$d^3\Pi_g \rightarrow a^3\Pi_u$	516.52
C ₂	$d^3\Pi_g \rightarrow a^3\Pi_u$	563.25
H ₂	$3p^3\Sigma_u \rightarrow 2s^3\Sigma_g$	602.16
C ₂	$d^3\Pi_g \rightarrow a^3\Pi_u$	619.12
H α	$n^{\prime} = 3 \rightarrow n = 2$	656.81

1.7 Aims and Expectations

As previously stated, a MWPR will be used to synthesise CVD diamond. The magnetron used at the School of Chemistry, University of Bristol is 15 years past its lifetime and is expected to have lost its efficiency. A new magnetron (made by Sairem; model number – ISO65K – WR340B1), being new, is expected to be more power efficient than the old one. So, the aim of this report is to predict the

characteristics of the diamond film grown under the new magnetron. First, to predict the outputs of the new magnetron, the old magnetron must be used to grow films under a wide range of conditions. Power, pressure, wire thickness, and gas composition are the variables to be changed, whereby the substrate temperature will be closely monitored. Grain sizes, growth rates, surface morphology, and film quality will then be measured to probe the effects of changing the growth conditions. This will then give a wide enough range of data to predict the effects of higher microwave power on the diamond film grown.

Higher powers means that the plasma temperature will be higher, thus the hydrogen atom concentration will also be higher (according to equation 2). Higher hydrogen atom concentration in the gas mixture is known to increase growth rates, and improve film qualities. Therefore, it is necessary that the predictions for the new magnetron will have to factor in how much hydrogen dissociation occurs under a range of different pressures and powers. Optical emission spectroscopy will be used to probe the strength of the hydrogen transitions in the Balmer cycle, and then, we can extrapolate the data to find out the intensities at higher powers, using literature data as guidance. Thus, we can use this to find expected growth rates using the new magnetron.

2. Results and Discussion

2.1 Growth Runs Using the 1.5 kW ASTeX Magnetron (HS-1000)

The first part of the experiment involved growing 15 substrates under various conditions. The substrates were then subject to SEM and Raman spectroscopy where they were characterised, looking specifically at grain size, growth rates, sp^2 vs sp^3 peaks and surface morphology. Standard conditions for diamond growth had been set to 1200 W, 150 Torr, CH_4 (4%), N_2 (0%), and a 5 ml wire, where growth times were kept to 6 hours.

2.1.1 Pressure Dependency

The pressure of the microwave chamber was changed during diamond growth, whilst keeping all other variables constant. Three different pressures were chosen, 100, 150 and 200 Torr. The increase in pressure confines the plasma, where its electron density increases as a result of a higher amount of hydrogen dissociation (equation 3). As the pressure rises from 100 to 200 torr, growth rates jump to $5.77 \mu\text{m/hr}$ from $1.95 \mu\text{m/hr}$ (figure 31). The reason for the rise in growth in rates is merely a facet of a higher degree of dissociation of hydrogen, as this increases the frequency at which they nucleate onto the substrate, along with other hydrocarbon radicals. At 200 torr, very large grains form, reaching an average size of $7.88 \mu\text{m}^2$, the large grains are associated with thicker diamond film grown, since when the grains grow upwards they also grow outwards, overlapping with each other (figure 32). The SEM images show that at higher pressures, the {111} faces begin to outcompete the {100} faces, which serves to roughen the surface. {110} grains also become more numerous at elevated pressures, due to the etching rates of {110} surfaces being unaffected by substrate temperature (pressure causes the substrate temperature to rise).²⁴ Whereas the etching rate of {100} faces increases when temperature does. The quality of the diamond films also changes as pressure does. Raman spectra (figure 33) show that the most pure diamond film grown is at 150 Torr, since the ratio of the 1332 cm^{-1} , sp^3 peak to the graphitic, $1430\text{-}1570 \text{ cm}^{-1}$, sp^2 peak is greatest. The broad peak from $1430\text{-}1570 \text{ cm}^{-1}$ is a combination of the stretching mode of the C=C bond in transpolyacetylene, and the G band from amorphous carbon.⁷⁹ At 100 Torr, the plasma density is quite low, limiting the amount of hydrogen dissociation. Thus, more surface CH_3 units have a, or

some hydrogens left unabstracted, leading to a higher degree of graphite formation. The diamond film grown at 200 Torr has an even lower $sp^3:sp^2$ ratio than at 100 Torr. At high pressure, the plasma density is very high, leading to large amounts of atomic hydrogen, but also elevated levels of hydrocarbon radicals such as CH_3 , CH , C_2H_2 , etc being produced. This leads to an increase in the growth rate of larger crystals. However, the activation energy for non-diamond carbon species is lower than that of diamond, hence they are more likely to nucleate and grow leading to the formation of graphitic carbon. Therefore, the increase in deposition rate of diamond, along with a higher probability of non-carbon species depositing onto the surface, increases the overall graphitic content of the diamond film.

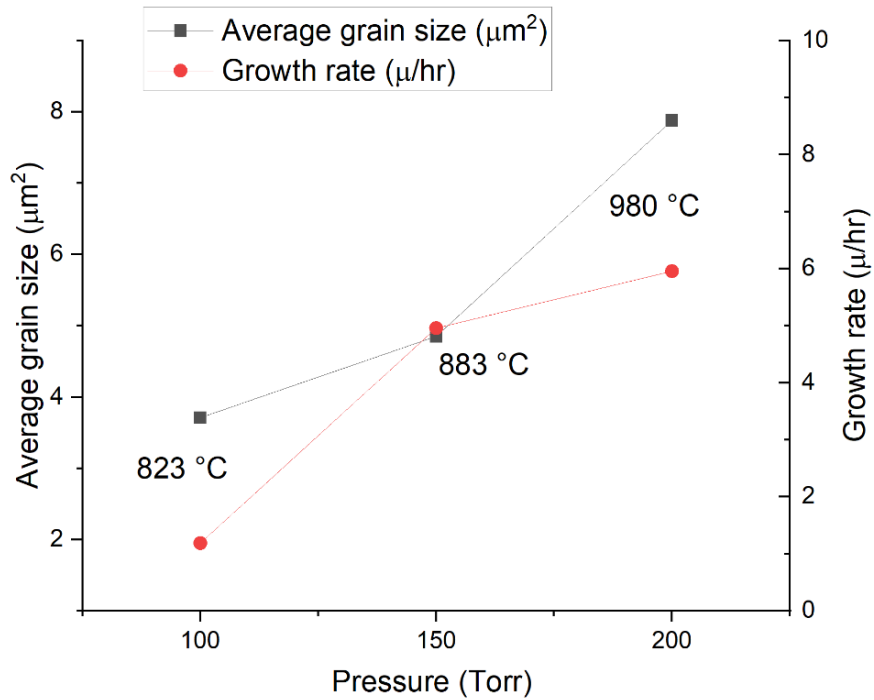


Figure 31: This graph shows the dependency of grain size and growth rate as a function of pressure. The substrate temperatures are shown above the data points. A positive correlation between both pressure and temperature with growth rates and grain sizes are observed.

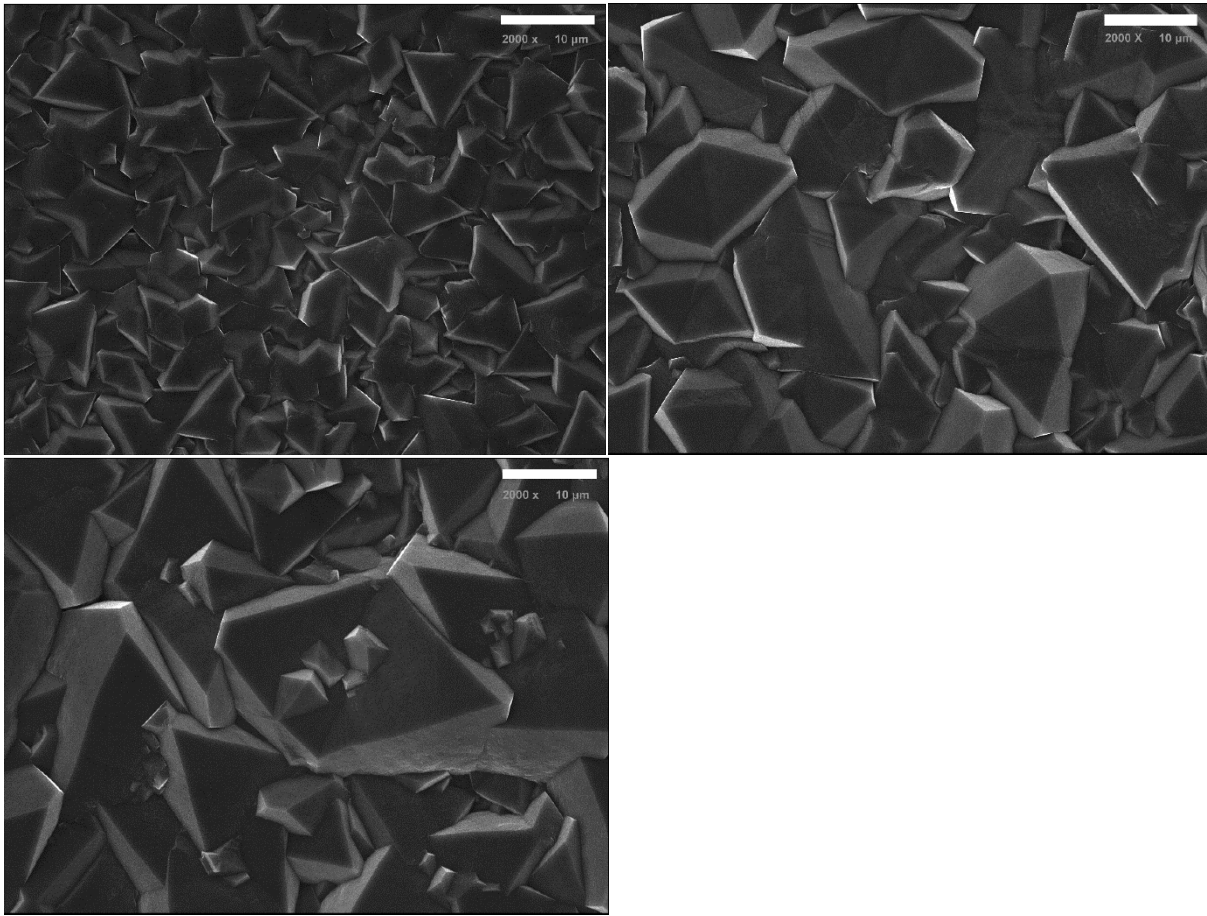


Figure 32: This series of SEM images shows the trend of an increase in grain size with an increase in pressure. At the top left, the diamond was grown at a pressure of 100 Torr, where small irregular polyhedra are seen. Top right, is 150 Torr, where there is {111} and {100} faces, with very few {110} facets. The bottom left image shows much bigger grains, with more {110} faces than at 150 Torr. Twinning of grains are present in the 150 and 200 torr runs, and at 200 torr, the large grains are shown to be nucleation sites for {110} and {111} crystals.

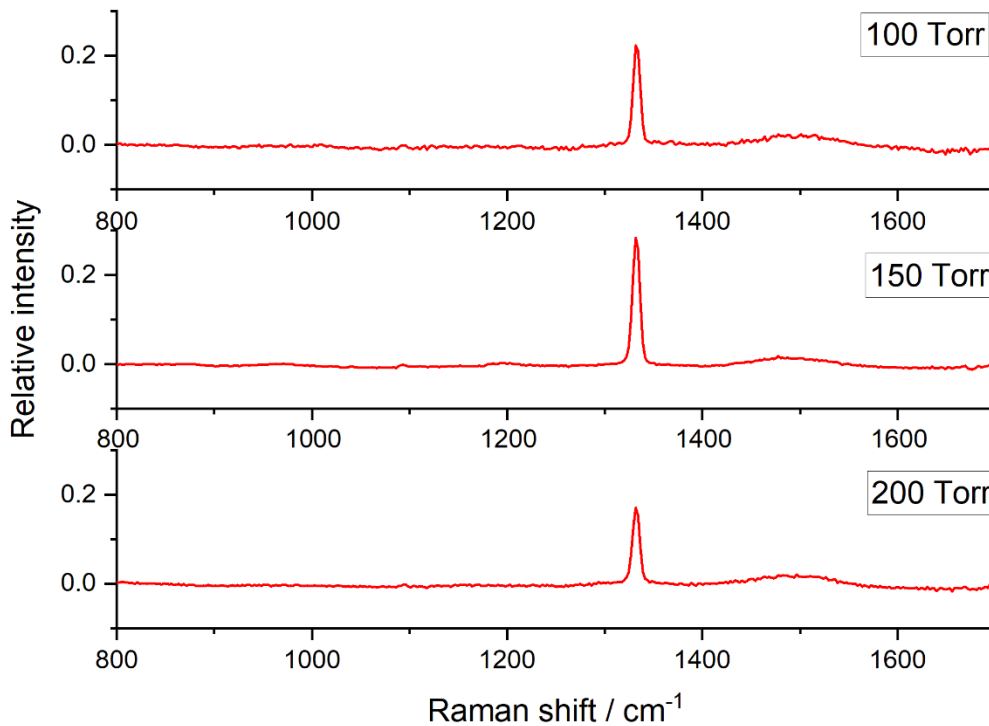


Figure 33: These 514 nm visible Raman spectra show the extent of graphitisation in diamond grown at various pressures. At 100 and 200 Torr, the diamond grown shows worse quality, since the $sp^3:sp^2$ ratio is lower than at standard conditions.

2.1.2 Power Dependency

Four different power regimes were used to grow CVD diamond film in a MWPR. First, a low power 1000 W run produced very small grains ($1.67 \mu\text{m}^2$) and low growth rates ($1.79 \mu\text{m/hr}$) at $820 \text{ }^\circ\text{C}$ (figure 34). The grains produced were mixtures of smaller square-based pyramid $\{111\}$ grains, and slightly larger, flat triangular $\{100\}$ grains (figure 35). The reason for an unusual amount of $\{111\}$ faces, is likely to be greatly influenced by the abrasion process, and the orientation of the silicon substrate. The abrasion process could be inconsistent since its done by hand, where some areas might be more abraded than others, leading to differently sized and shaped grains. These would be more prominent at low film thicknesses since the grains havent significantly overlapped eachother yet, hence at 1000 W, there are a large variety of shapes and sizes. The second six hour run was grown under standard conditions, where 1200 W of power was used producing temperatures of $883 \text{ }^\circ\text{C}$. In this instance, averagely sized grains ($4.85 \mu\text{m}^2$) and growth rates ($4.97 \mu\text{m/hr}$) were grown when compared to the data collected across all growth runs. The surface comprised mainly of flat triangular grains, many of which have grown adjacent to one another, where they coalesce to form diamond shaped structures, this is known as twinning. A higher power, a 1350 W run produced the largest grains and the thickest films when varying the power output. This can be put down to reaching temepratures of $976 \text{ }^\circ\text{C}$, which are optimal for high growth rates due to the faster kinetics of hydrogen disscioation (equation 4), as well as faster hydrogen atom and methane adsorption onto the substrate. The surface is mostly made up of $\{111\}$ facets with small $\{100\}$ facets in between the $\{111\}$ facets, this gives rise to a very textured surface. The highest power run didn't follow the upwards trend of, the greater the power, the greater the growth rates and grain size. At 1500 W, the temperature was $1060 \text{ }^\circ\text{C}$, this was found to be much too high to produce large grain sizes and high growth rates. This is due to the increased etching rates at high temperatures, limiting the growth rate, and reducing the film quality, since a rise of transpolyacetylene was found in the rivenes at grain boundaries.⁸⁰ The columnar shape of the grains means that the crystal is growing completely

perpendicular to the substrate.⁷⁹ The {111} facets defines the morphology of the grains, and very small {100} faces, on top of the columns, grow parallel to the substrate.

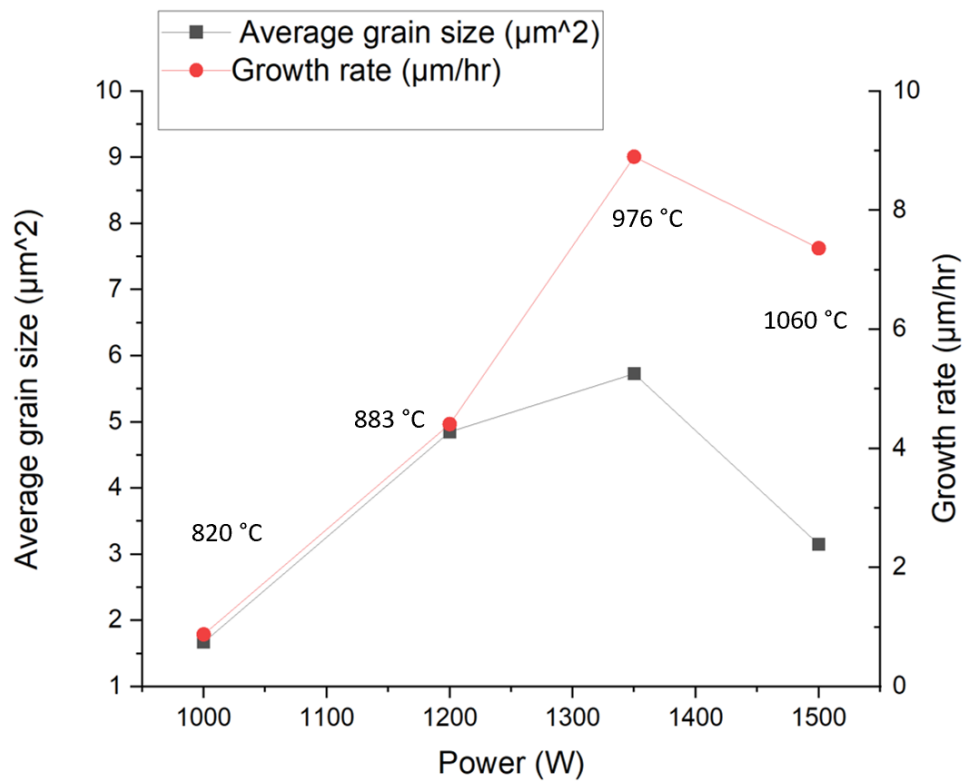


Figure 34: This graph shows the dependency of grain size and growth rate as a function of the power output. The temperatures of the six hour growth runs are shown on the graph, as higher power is directly correlated to higher temperatures.

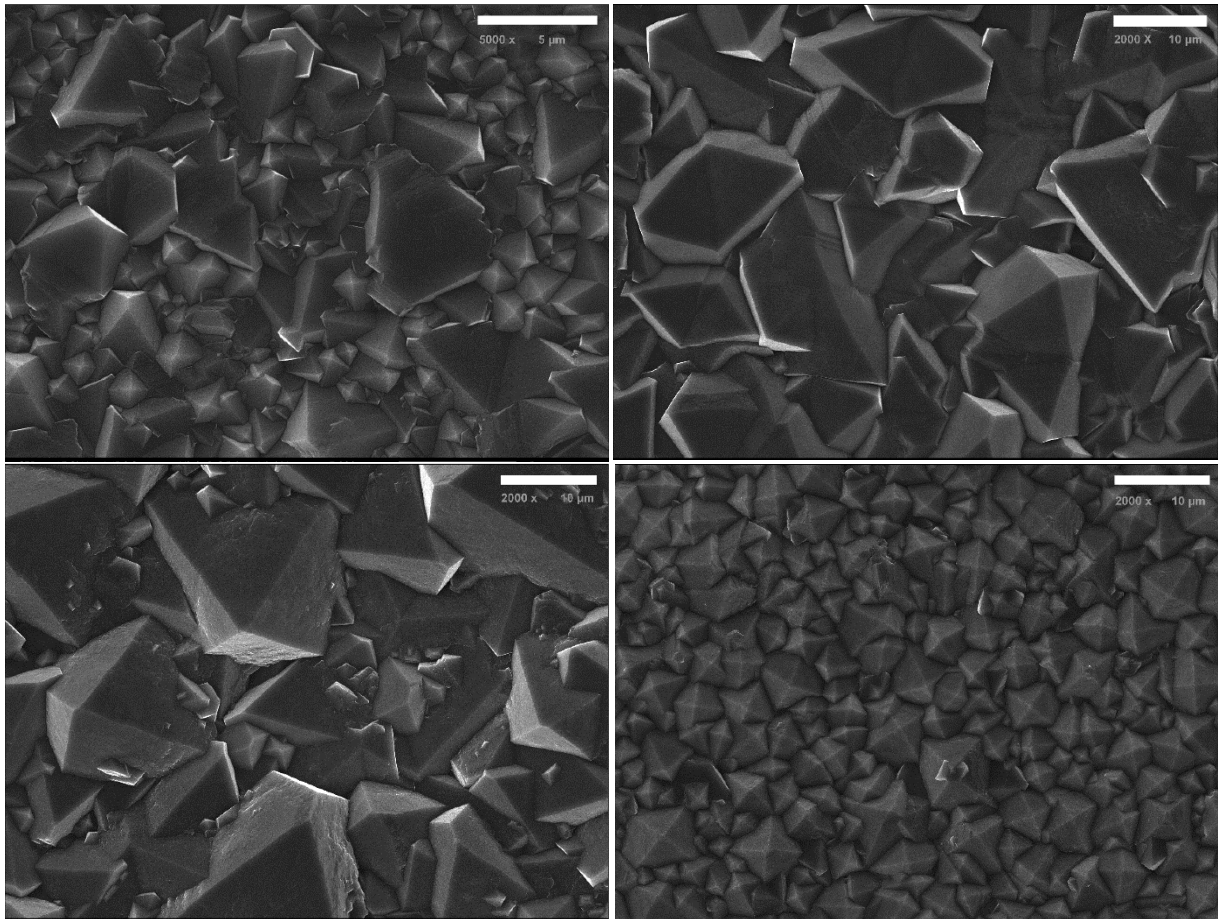


Figure 35: These SEM images show the change in morphology as the power is increased from 1000 W (top left), 1200 W (top right), 1350 W (bottom left), to 1500 W (bottom right). An increase in the number of {111} facets as power increases is due to a rise in substrate temperature.

Raman data (figure 36) shows that diamond was successfully formed for all substrates grown at different powers, as a sharp peak is seen at 1332 cm^{-1} , indicative of the t_{2g} mode of diamond. Variable amounts of non-diamond carbon was formed at different powers, the smallest sp^2 peak was at 1200 W and the largest at 1500 W. The large crystalline graphite peak grown at 1500 W can be rationalised by its small grains. The small grain sizes are as a result of the etching of diamond, and instead, graphite and transpolyacetylene are deposited in these grain boundaries. As the power increases (i.e. the temperature), the so called 'G' band upshifts, and this rise in frequency correlates to the increase of amorphous carbon content produced from the favourable deposition of graphite.⁸¹

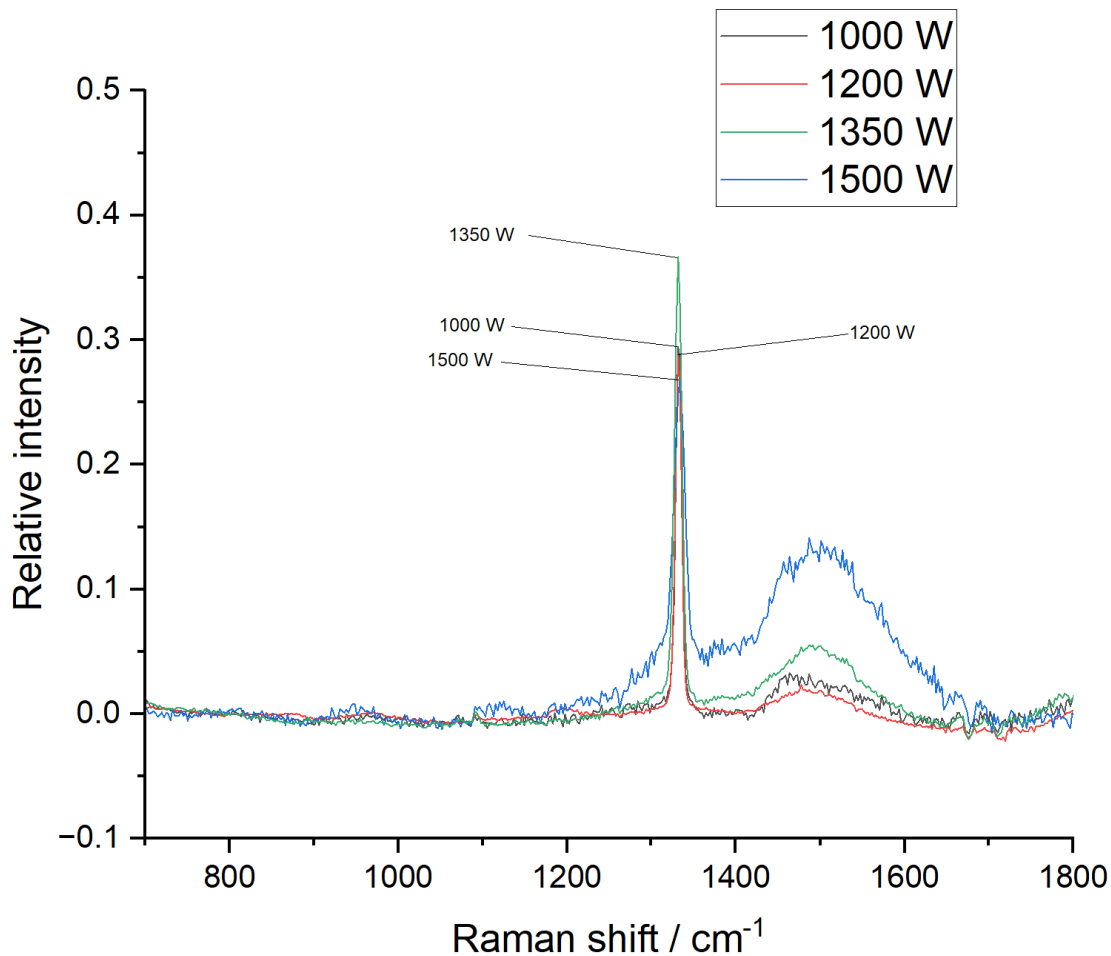


Figure 36: The Raman data shows the respective qualities of diamond film grown under different power conditions. The broad peak ranging from around 1430-1570 cm^{-1} indicates impurities in the form of graphite or amorphous type carbon. The larger this peak is relative to the diamond peak at 1332 cm^{-1} , translates to a worse film quality. Thus, the best quality film is found at 1200 W, and the worse, at 1500 W. The labels indicating the powers at which the diamond is grown at are pointing to the top of the diamond peaks.

2.1.3 Methane Concentration Dependence

The standard methane concentration for growth was set to be 4% (a flow rate of 12.5 Scm). The agreement between grain size and growth rates continue, as we see a decrease in both of these results as the methane concentration is changed either side of standard growth concentrations (4%), (figure 37). The reason for the increase in growth rate from 2% to 4% can be attributed to a larger amount of methyl radicals being incorporated in to the substrate by the mechanism illustrated in figure 5. The growth rate drops off at higher methane concentrations, most likely due to higher graphite formation from increased etching rates.

However, these observations regarding growth rates oppose those found in the literature, where an increase in methane concentration has found to increase growth rates up to 5% of CH_4 .^{82, 83} There are some inconsistencies when comparing literature data to those collected in this report, and this

mainly involves the microwave reactor set up. Xiaobo Hu *et al*, used a microwave plasma reactor at 300 torr, and substrate temperatures of 1150 °C, in an Ardis 300 reactor, capable of producing microwaves up to 6 kW.⁸² Reshi *et al*, kept substrate temperatures at 950 °C, whilst using low pressure at 72-75 Torr, which led them to form diamond film with growth rates at 5.02 μm/hr for a 5% CH₄/H₂ gas mixture.⁸³ The use of different conditions yields different different plasma densities which alters the plasma chemistry. This could be a reason why the 6% growth in this report differs to the 5% CH₄ as seen in the literature. Despite this, there are mitigating errors in the experimental strategy that potentially might of thrown the results. The SEM wasn't taken in the exact same spot on each substrate, and even if it was, the positioning of the substrate in the reactor could have been different each time despite centering it using placers. The reason this is an issue is because the plasma density isn't uniform across the whole substrate. This is known simply by the observation that during optical microscopy, the film went in and out of focus as the lens moved from the centre, outwards. This is indicative of different thicknesses in the film across the substrate resultant from a non-uniform plasma.

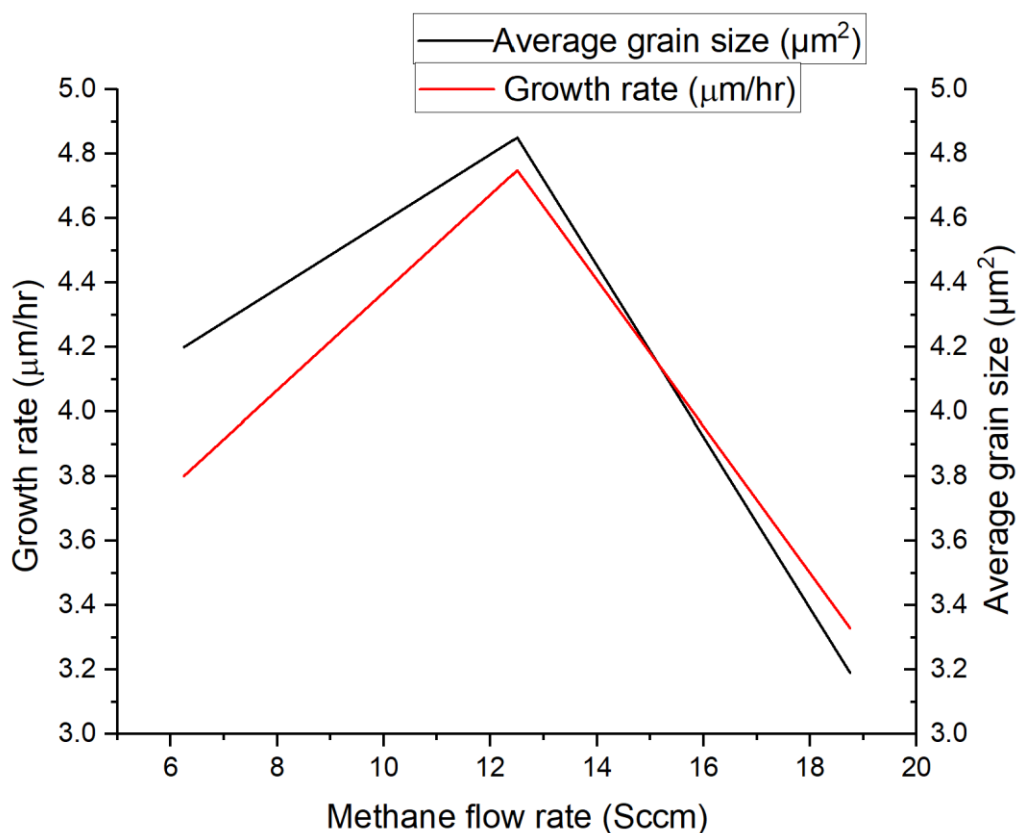


Figure 37: This spectra shows the variation of grain size and growth rate as a result of a change in methane flow rates in the plasma. The agreement between growth rate and grain size can be seen, whereby standard conditions (12.5 Sccm) produces the largest grains.

The Raman data (figure 38) also opposes the literature data, since the peak for diamond is the sharpest for the 6% run as its full width half maximum (FWHM) is 7.71, compared to 8.25 and 8.69 for the 2% and 4% runs respectively.^{82,83} One theory is that the large and irregular shaped grains grown at 4% reflects the light generated from the laser, and thus its intensity is reduced. Raman spectroscopy was repeated two other times to make sure that there were no errors in data collection, but the results were more or less the same. Literature data suggests that as the methane concentration is increased the FWHM of the 1332 cm⁻¹ peak increases.^{82, 83} So, if going by the

literature, the 6% run is the anomalous data point, although the use of different reactor set ups and slightly different reaction conditions could of produced different results. What is quite odd is that the SEM pictures show darker regions for the 2% and 6% film than at 4%, indicating higher graphite content as expected. Also, for all the other growths, the 4% run is in line with all the other results, i.e. when changing the power, the Raman and SEM data follow the trends seen in figure 34, 35, 36, and this indicates that the 2% and 6% growths are anomalous. The broad peak ranging from 1430~1570 cm^{-1} , again, is a result of a mixture of transpolyacetylene and amorphous carbon present in the diamond film.

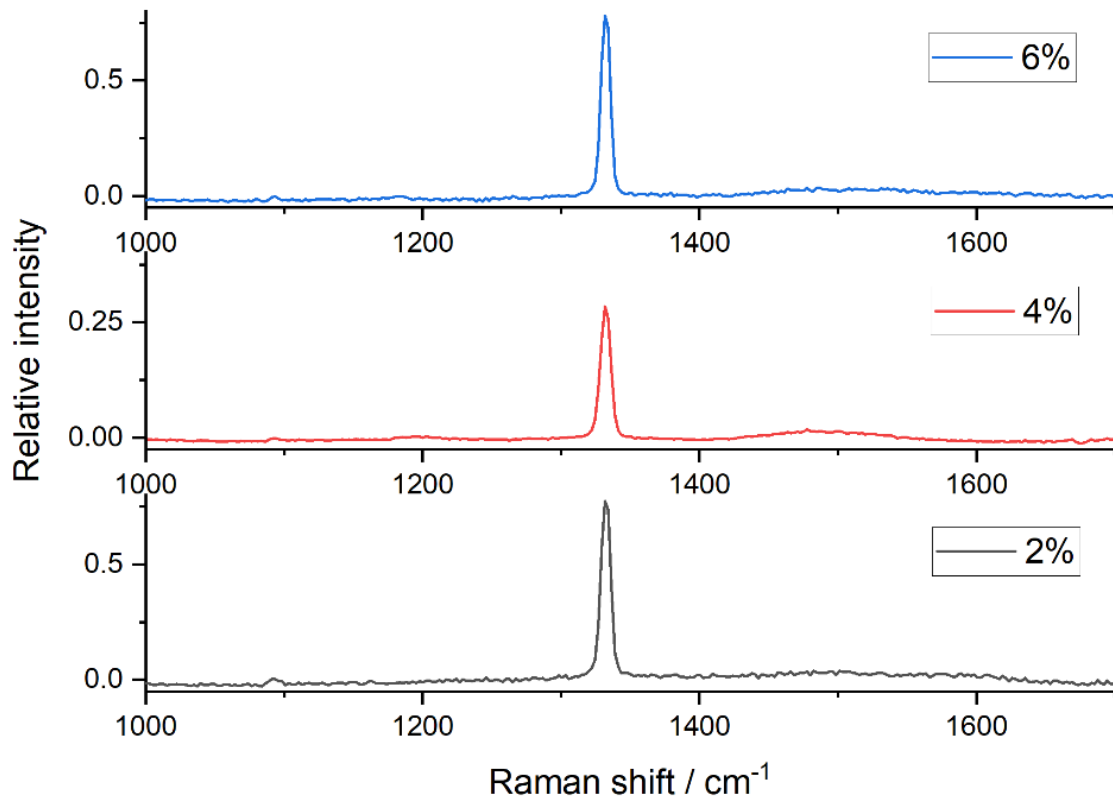


Figure 38: These series of Raman spectra shows how film quality changes with an increase in methane concentration in the microwave plasma. The FWHM are 8.25, 8.69 and 7.71 cm^{-1} at 2%, 4%, and 6% respectively.

Taking a look at the surface of the diamond film shows some obvious differences in growing diamond at different methane concentrations. The change in grain size either side of the 4% growth is quite apparent, however this is just a facet of increased thickness. The more significant difference of the surface are the characteristic shapes of the grains themselves. Figure 39(a) is film grown at 2% methane, where twinning of irregularly shaped {100} grains is observed. There's a mixture of {100}, {110}, and {111} facets, giving no distinct surface morphology. There is an unusual prominence of striations that are present in some of the crystals (figure 40), these are due to high growth times, where the grains overlap each other, creating these micro-ridges. However, the 2% growth has more of these ridges than at any other growth condition, this could be due to insufficient methane levels. A lack of methyl radical formation reduces complete surface nucleation, hence the grains don't grow uniformly, forming the striations. The 4% methane run is at standard conditions and a description of the film has been included in previous discussions regarding power and pressure. What is apparent however is the presence of large, defined {111} facets at 4%, which at 2% and 6% seem much harder to come by. The film grown at 6% is more like the 2% film than the 4% film. The grains are smaller

and have more undefined shapes than at 2%, this is a result of a greater amount of layering, where the grains grow over each other creating irregular shapes.

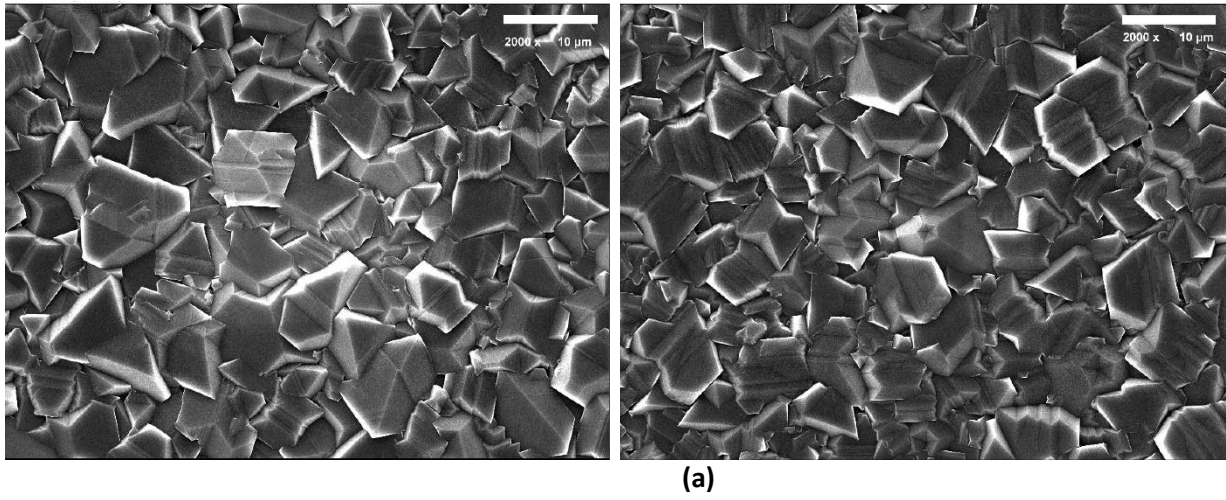


Figure 39: SEM images of diamond film grown at (a) 2%, and (b) 6% $\text{CH}_4:\text{H}_2$. These pictures are at methane concentrations +/- 2% of the standard methane levels, in which they show highly similar surface morphologies.

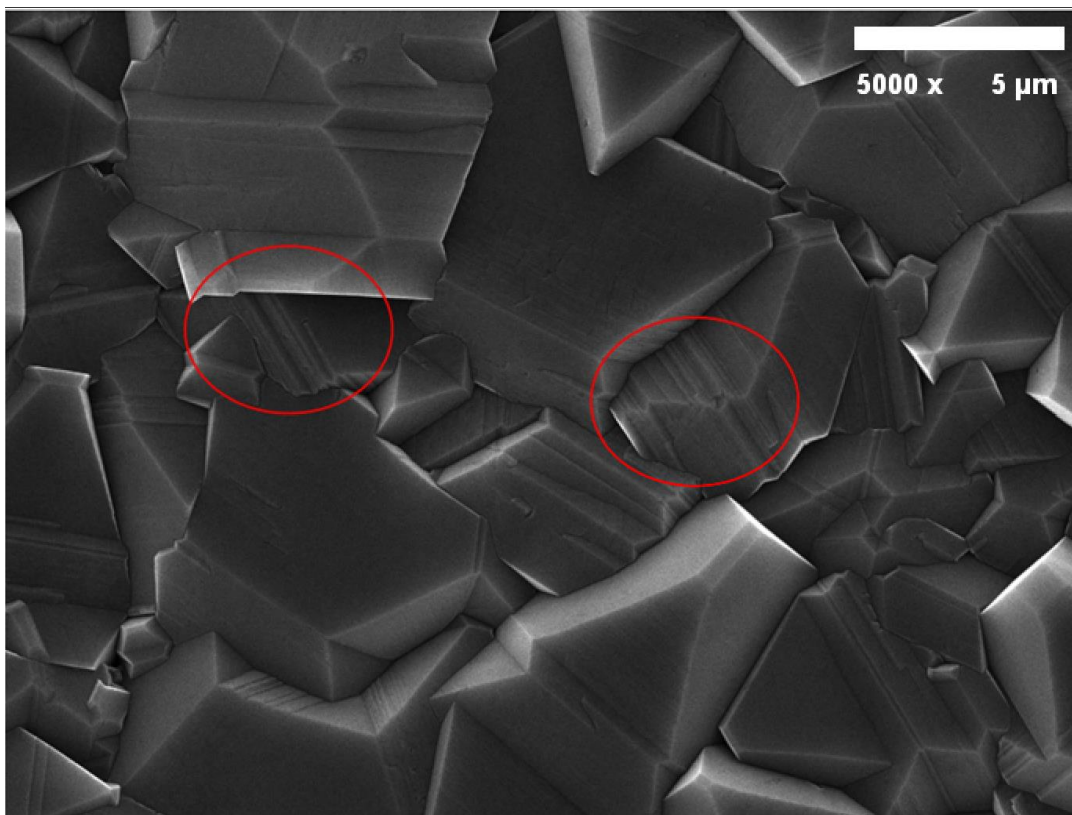


Figure 40: A close up SEM image showing an unusual structural defect at 2% methane. These are described as striations or micro-ridges.

Optical emission spectroscopy (OES) provides useful data regarding the gas composition of the plasma formed, as well as the intensities of some of the electronic transitions occurring in the species present. There are observed peaks (figure 41) at 387, 430, 437, 471, 486, 516, 557, 563, 656 nm labelled a-j. The 5 vibrational modes ($\Delta v = +2, +1, 0, -1, -2$) correlating to the C₂ Swan system are labelled c, d, f, g and i respectively, which arise from electronic transitions ($d^3\Pi_g \rightarrow a^3\Pi_u$).⁸⁴ The peaks labelled a, b and h are from emissions by CH ($B^2\Sigma^- \rightarrow X^2\Pi$), CH ($A^2\Delta \rightarrow X^2\Pi$), and H₂. The emissions at different wavelengths suggests that there are multiple mechanisms in the dissociation of CH₄. These are by electron impact, fragmenting the molecule into CH₃ + H, and by dehydrogenation, which explains the formation of CH. Two further peaks are attributed to atomic hydrogen transitions, e, at 486 nm is from the H- β transition, and j, at 656 nm is from the H- α transition. The peaks relating to the Swan bands have a clear trend, the greater the methane concentration, the greater the intensity of the peak. The peaks relating to the Balmer series are very similar across the methane concentrations, since the change in hydrogen concentration as a result of elevated methane levels is very small.

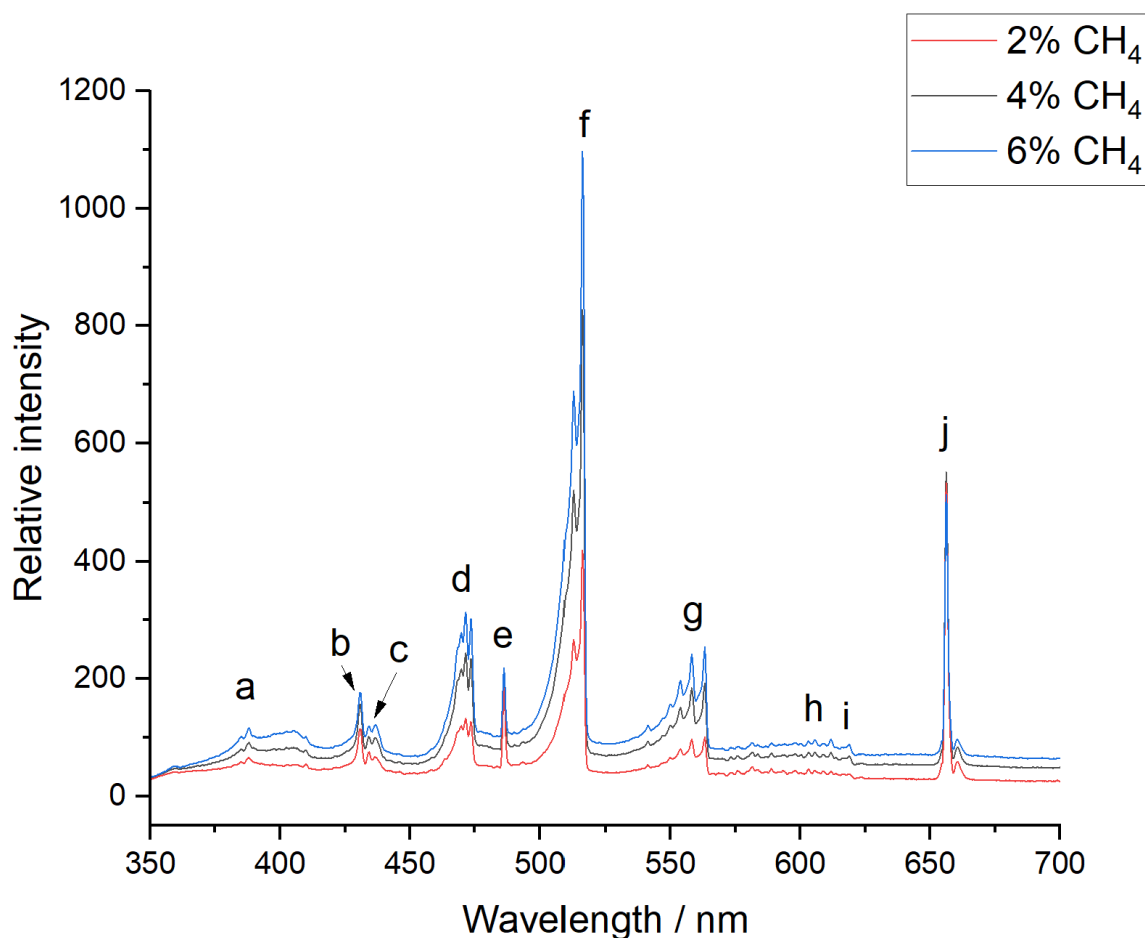


Figure 41: The OES shows the change in intensity when a different gas mixture of H₂/CH₄ is used to form a microwave plasma. The labels a-j are those of significance which relate to the C₂ Swan band, the Balmer series, and other species undergoing electronic transitions in the visible region.

2.1.4 Nitrogen dependence

It was discussed that a small amount of nitrogen added to the plasma atmosphere could increase the rate at which diamond grows. Figure 42 agrees with the literature, and a plateau region of the growth rate is expected to follow at higher nitrogen concentrations.²⁵ This is the first time the growth rates and grain size don't follow the same trend. The lower grain sizes observed at higher nitrogen levels can be rationalised by the film quality. As the nitrogen flow rate is raised, the more graphitic the film becomes since there is greater amount of nitrogen incorporation into the films (figure 43) – where more nitrogen increases the preference for sp^2 carbon formation. Smaller grains are also formed by nitrogen reacting with carbon to form carbon nitride, which can inhibit diamond growth on the surface.⁸⁵

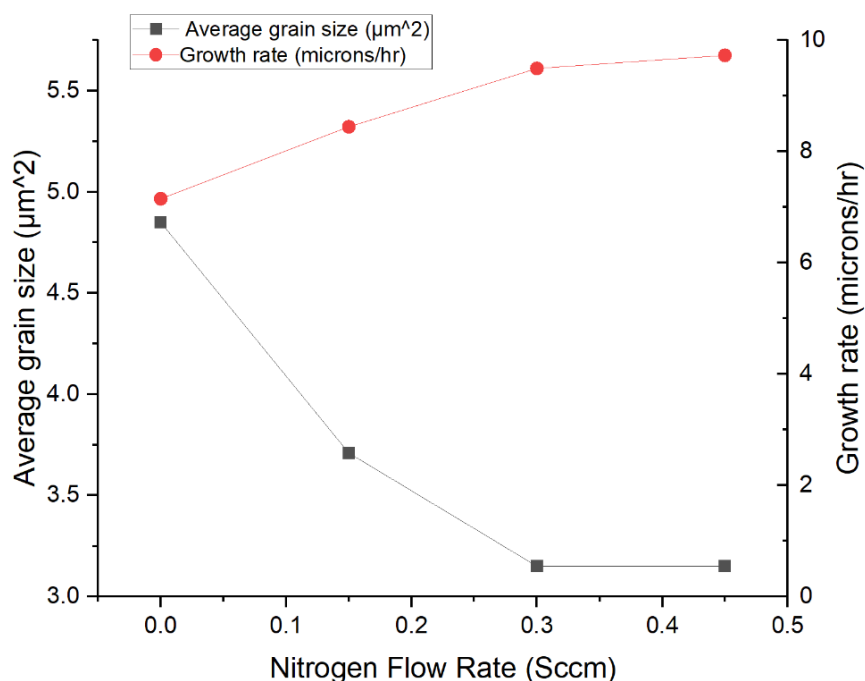


Figure 42: This graph shows the dependence of nitrogen on grain size and growth rate.

There are distinct differences in the surface morphologies when varying the nitrogen concentration, even by small amounts. The SEM images in figure 44 shows how the addition of nitrogen causes the crystals to grow preferentially in the $\{100\}$ plane over the $\{110\}$ and $\{111\}$ direction. At high nitrogen concentrations, the desire for diamond to grow solely in the $\{100\}$ plane is so high, that the resultant film is incredibly smooth. The transition to $\{100\}$ films is obvious when looking at the 0.30 Sccm growth, where $\{100\}$ facets are seen at the top of the $\{110\}$ and $\{111\}$ crystals. This observation proves that nitrogen increases the growth rates in the $\{100\}$ direction, which is in agreement with the literature.²⁴

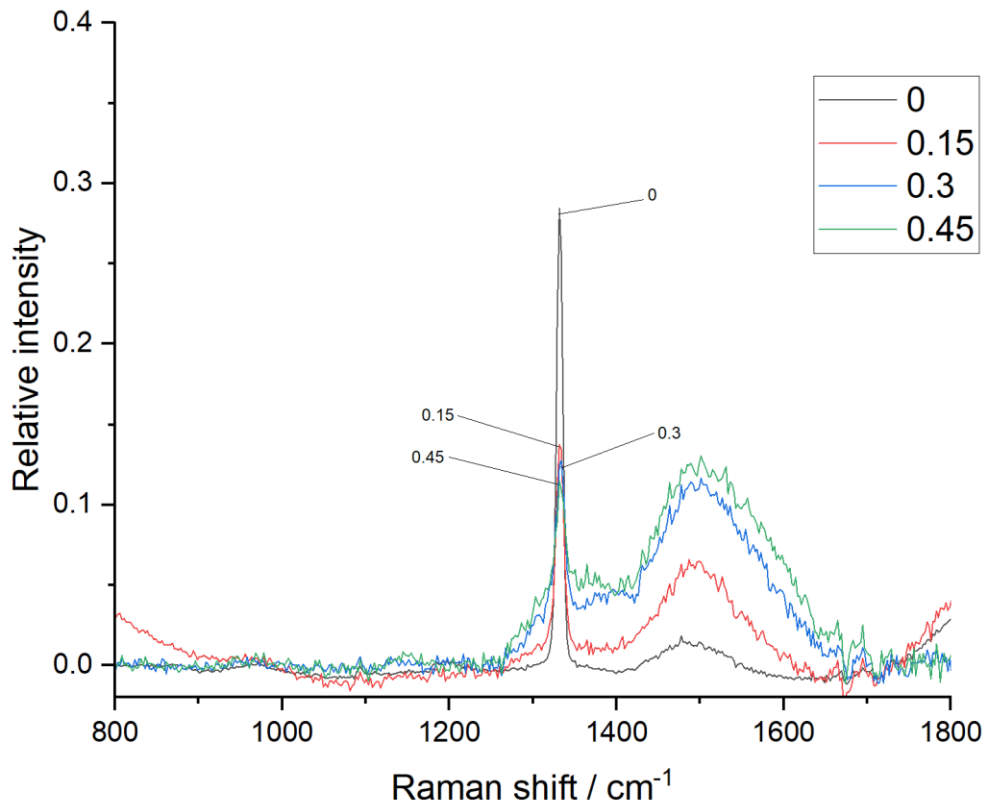


Figure 43: This graph shows the Raman shifts with an increase in nitrogen flow rate measured in Sccm. The greater the nitrogen concentration, the lower the sp^3 peak and the higher the sp^2 peak, showing that the quality of the films decreases as nitrogen concentration increases.

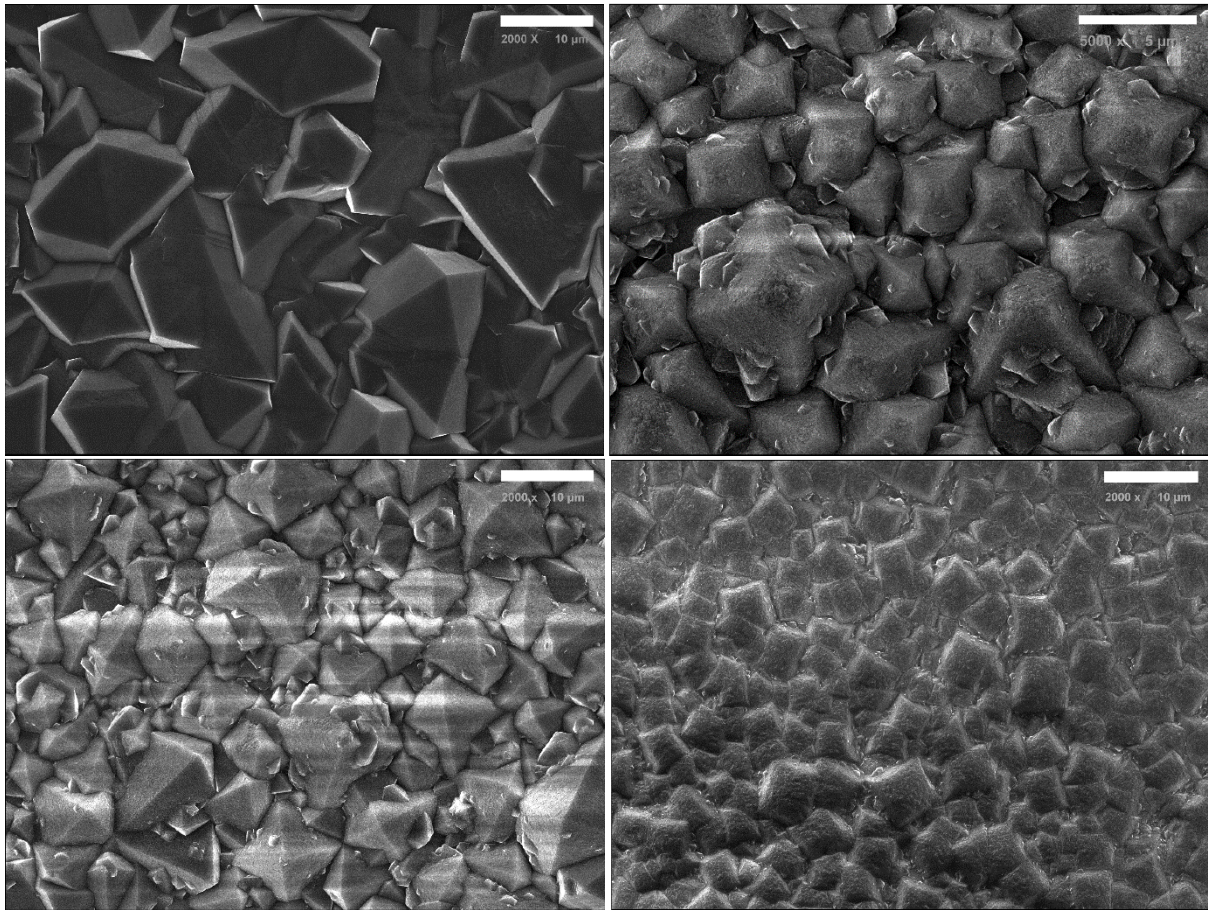


Figure 44: These SEM images shows the change in surface morphology as the nitrogen flow rate is increased. Top left (0 Sccm), bottom left (0.15 Sccm), top right (0.30 Sccm), and bottom right (0.45 Sccm). The surface becomes smoother as nitrogen flow rate is increased, and {100} facets grow more quickly.

OES data was collected for a range of nitrogen flow rates to see how the plasma gas chemistry changes through a change in nitrogen concentration (figure 45). The only significant change in the OES, comes from the CH ($B^2\Sigma^- \rightarrow X^2\Pi$) transition at 387 cm^{-1} . This indicates that the addition of nitrogen increases the production of CH by some pathway, and this could be a contributing factor in the increase in growth rate of the diamond film. The plasma is hot enough to dissociate N_2 into N atoms, atomic nitrogen can then cause methane to dissociate through collisions: $N + CH_4 \rightarrow CH_3 + H + N$. If this repeats itself, $N + CH_2 \rightarrow N + CH + H$ occurs, resulting in higher levels of CH, which explains the OES data.

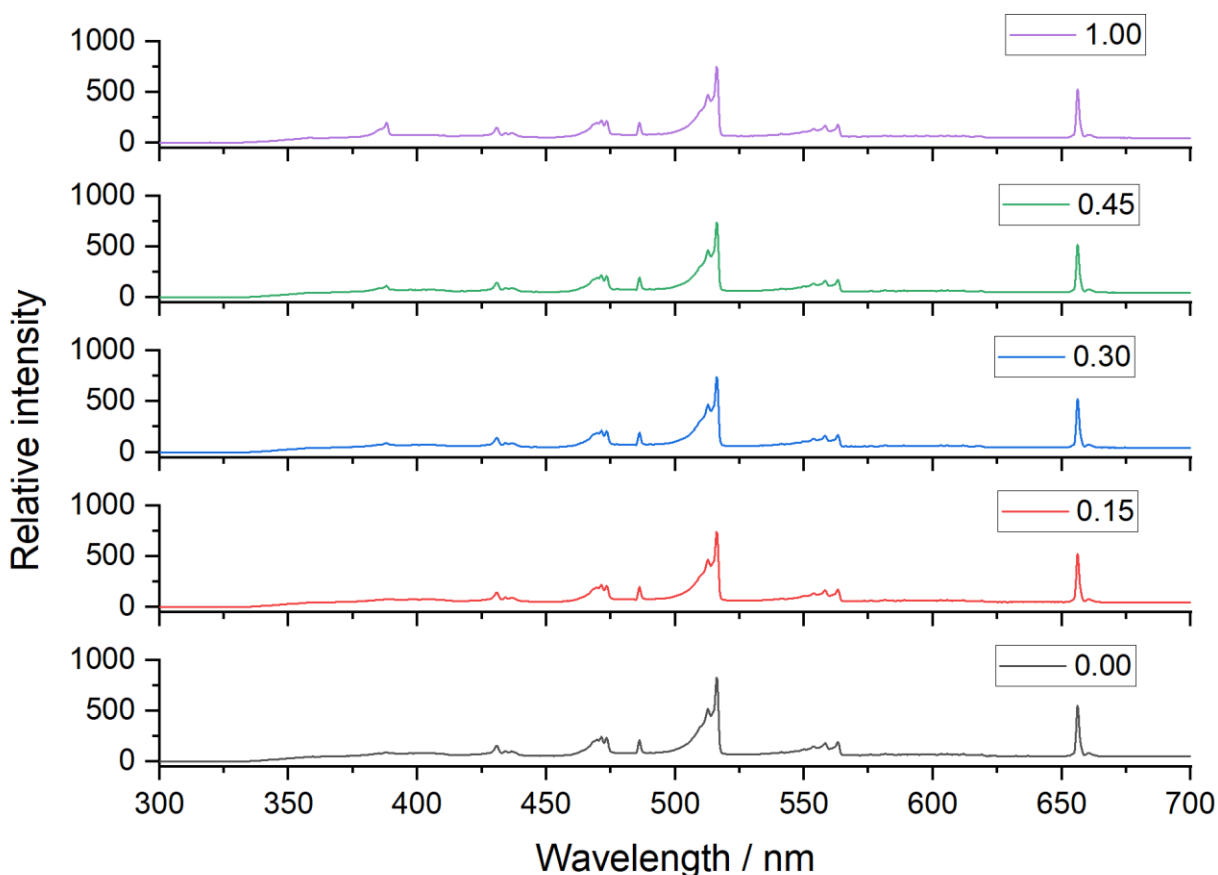


Figure 45: OES data for nitrogen flow rates ranging from 0 to 1 Sccm in a 4% CH₄/H₂ plasma. The only significant change as a result of higher nitrogen flow rates is in the CH ($B^2\Sigma^- \rightarrow X^2\Pi$) transition at 387 cm⁻¹.

2.1.5 Effect of Wire Thickness

A spacer wire is used to separate the molybdenum disc (that holds the substrate) from the cooling plate during diamond growth in the MWPR. A thinner wire means that the substrate will be closer to the cooling plate, and thus the substrate temperature will be lower. A thicker wire has the opposite effect, where the substrate will be further away from the cooling plate, and closer to the hot plasma, causing the substrate temperature to rise. A 0, 2.5, 5 and 8 ml tungsten wire were used, where the unit, ml, is milli inches (1/1000 of an inch). Two independent variables are changed because of the spacer wire used, the first is the substrate temperature, and the other is the distance the substrate is away from the plasma.

Without the use of a spacer wire, the growth rate was extremely slow at 0.21 $\mu\text{m/hr}$, and very small grains were produced, 0.921 μm^2 (figure 46). The small grains are a result of a low growth rate, and the morphology of the crystals grown are largely down to the orientation of the substrates surface from the abrasion process. As the spacer wire increases in thickness the substrate temperature rises. An increase in substrate temperature is what causes the growth rate to increase, and this is correlated to the grain size as previously discussed. At 8 ml, the wire is so thick that the substrate

temperature is 1020 °C which is too high for high quality diamond film to be grown, since etching rates of atomic hydrogen and sp^3 carbon species become too fast. This explains the drop off in growth rate but not the increase in grain size. The grain size continues to increase because the substrate is closer to the plasma ball, where the density of species is greater. Therefore, species important in diamond growth saturate the surface more effectively, and so bridging between grains can occur, owing to larger grains being formed. Raman spectra for the run at 8 and 2.5 ml show a small sharp peak at 1150 cm^{-1} which is trans-polyacetylene (figure 47).⁷⁶ This represents that either side of the standard wire thickness (5 ml), the substrate temperatures are non-optimal for good quality diamond film. For the 8 ml growth, the poor film quality is indicated by the existence of structural defects in the form of step edges (figure 48).

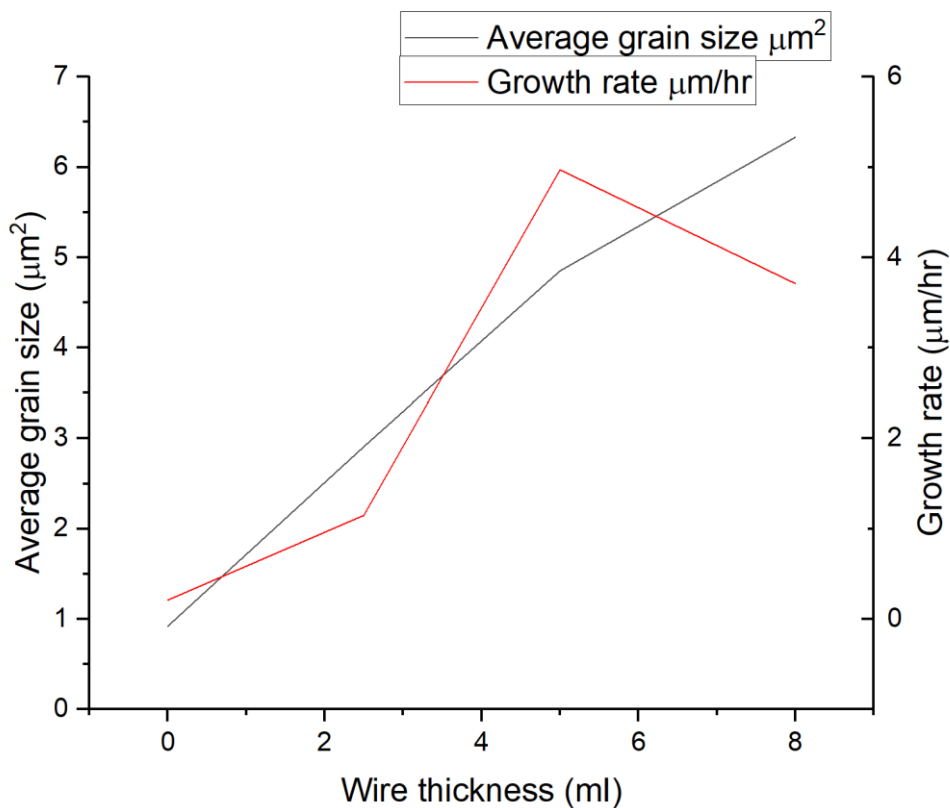
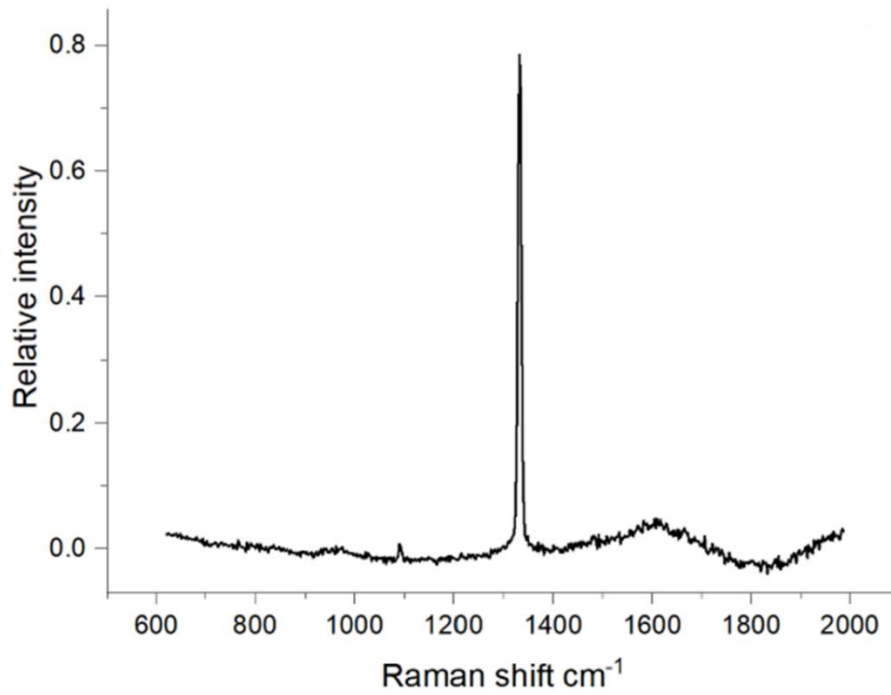
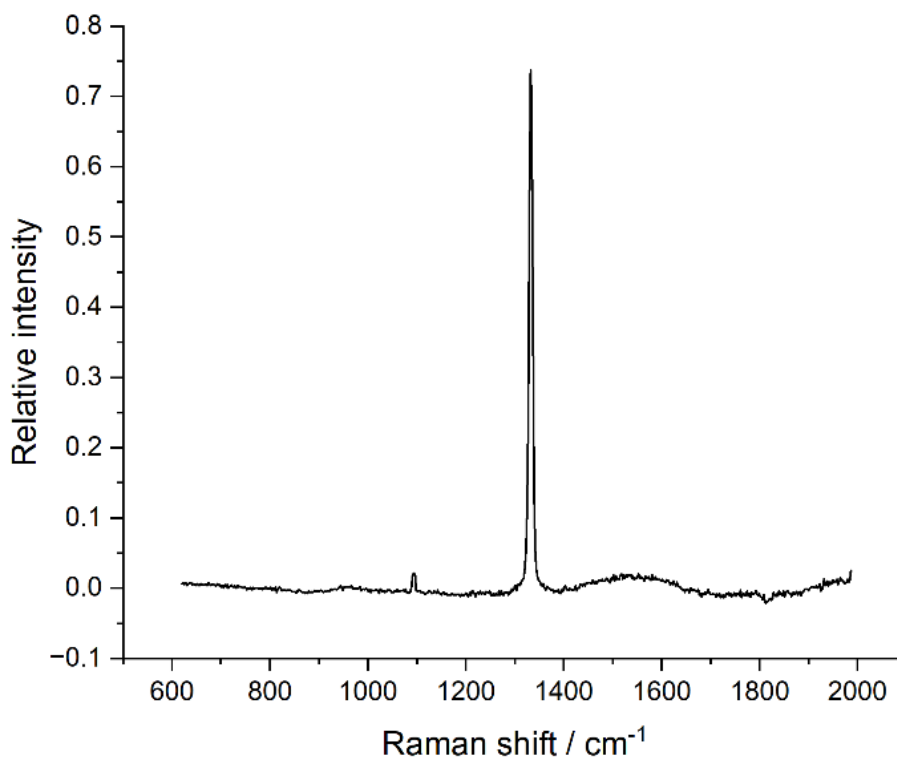


Figure 46: This graph shows the variation in grain size and growth rate as the wire thickness is being changed.



(a)



(b)

Figure 47: These Raman spectra using (a) 2.5 ml, and (b) 8 ml wire, show the presence of non-diamond carbon in the diamond films. The small sharp peak at 1150 cm^{-1} , and the broader peak at $1430\sim 1600\text{ cm}^{-1}$ is indicative of transpolyacetylene and graphite.

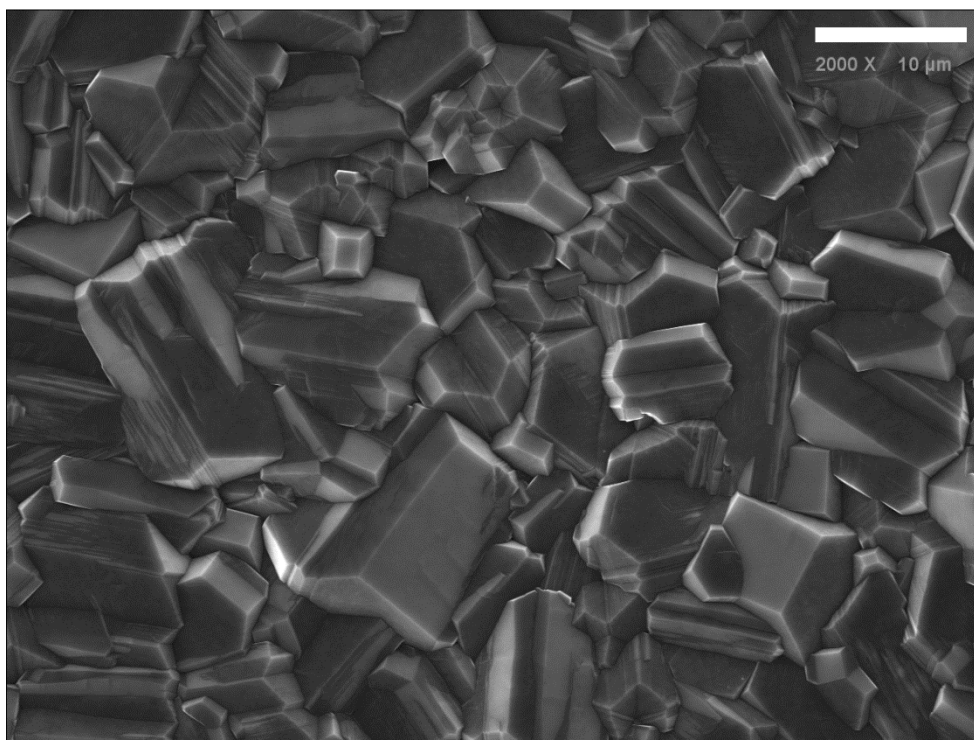


Figure 48: This 2000 x SEM image shows the diamond film grown using an 8 ml tungsten spacer wire. A wide range of grain sizes are observed, with a mixture of surface morphologies, where most grains contain step edges.

For more images and data regarding all the samples grown, see the supplementary information section.

2.2 Diamond Growth Predictions using the Sairem GMP G3 Magnetron System

After diamond growth using the old Astex-Seki magnetron system, the nature of the films grown under a wide range of reaction conditions is now known. The previous experiments have given a considerable amount of data to predict how the diamond grown under the same conditions differs when using the new magnetron setup. The magnetron to be implemented is manufactured by Sairem, the model number is GMP G3, and can produce microwaves up to 2 kW, with a frequency of 2.45 GHz. It is expected that the new magnetron is far more energy efficient than the old one, and so at the same microwave powers used, higher substrate and plasma temperatures will be reached. Higher temperatures cause a greater amount of hydrogen dissociation, where hydrogen atoms are known to increase growth rates. Thus, as the new magnetron can generate higher power microwaves, higher growth rates can be achieved if the substrate temperature can be maintained at optimal levels, which was found to be around 880-950 °C.

At standard growth conditions, 1200 W of power is used, and for the old magnetron, this produced substrate temperatures of 883 °C. When switching to the new magnetron, this temperature is expected to be higher, perhaps around 950 °C. This means that the diamond produced using the Sairem magnetron should look more like the 1350 W growth run on the Astex reactor. A more precise insight into what governs the diamond film grown can be determined from the OES data

collected. The intensities from the Balmer cycle for the H- α and the H- β transitions, as a function of the input microwave power can be summarised in figure 49. An almost linear increase in hydrogen intensities for both transitions are observed. Predictions have been made of the expected intensities from the hydrogen transitions in the Balmer cycles using work from A. Gicquel *et al*, where computer models have been used to simulate H₂ plasma (figure 11).⁴⁰ This has been used to estimate the hydrogen atom density by comparing the computational and experimental data from the intensities of hydrogen transitions in the OES collected. Literature has used 38 torr as their standard pressure, and the data used in these diamond growth runs is from 100-200 torr. I. Koleva *et al* found that at low pressures, hydrogen dissociation increased linearly as pressure did (which is in accordance with the experimental data).⁸⁶ Thus, the data modelled in figure 11 can be used to show how the experimental data is in accordance with the computer models. When comparing hydrogen densities in the centre of the plasma to the H- α transition intensities against power, it's seen that they both follow a linear relationship (figure 50). This provides assurance that the H- α intensities at higher powers follows the same linear relationship, and thus, for the 1500 W run on the new magnetron the H- α intensity can be predicted with high confidence.

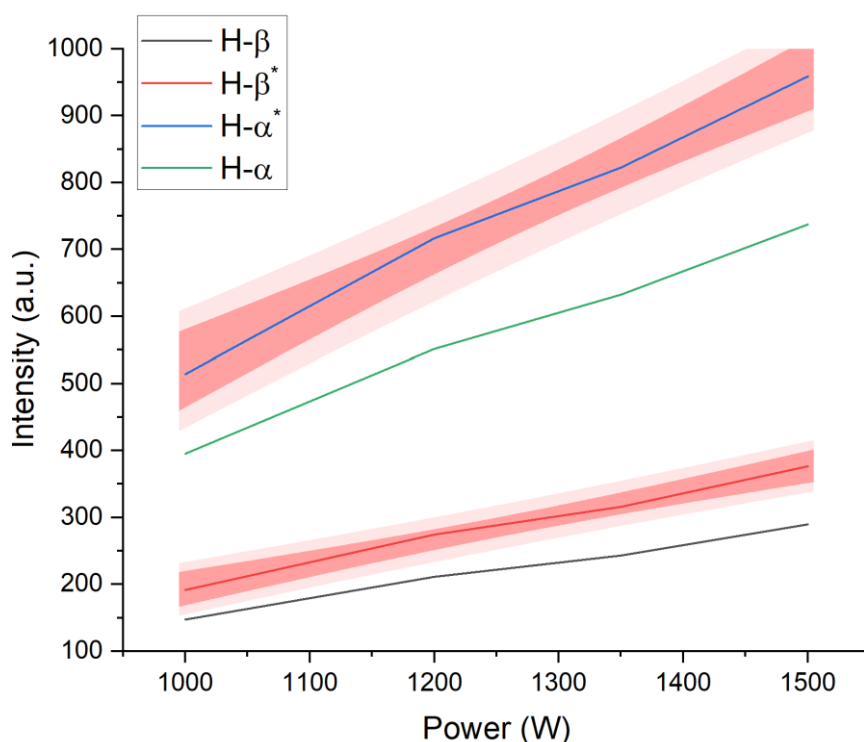


Figure 49: This plot shows the relative intensities of the H- α and H- β transitions from OES data of a H₂/CH₄ plasma (4% CH₄). H- α^* and H- β^* show the predicted intensities for those transitions if a 20% increase in atomic hydrogen production occurred using the new magnetron at the same microwave output power. The darker shaded red shows a stronger confidence level of what the intensities are expected to be, whereas the lightly shaded region shows the outer limits of the hydrogen transition intensities.

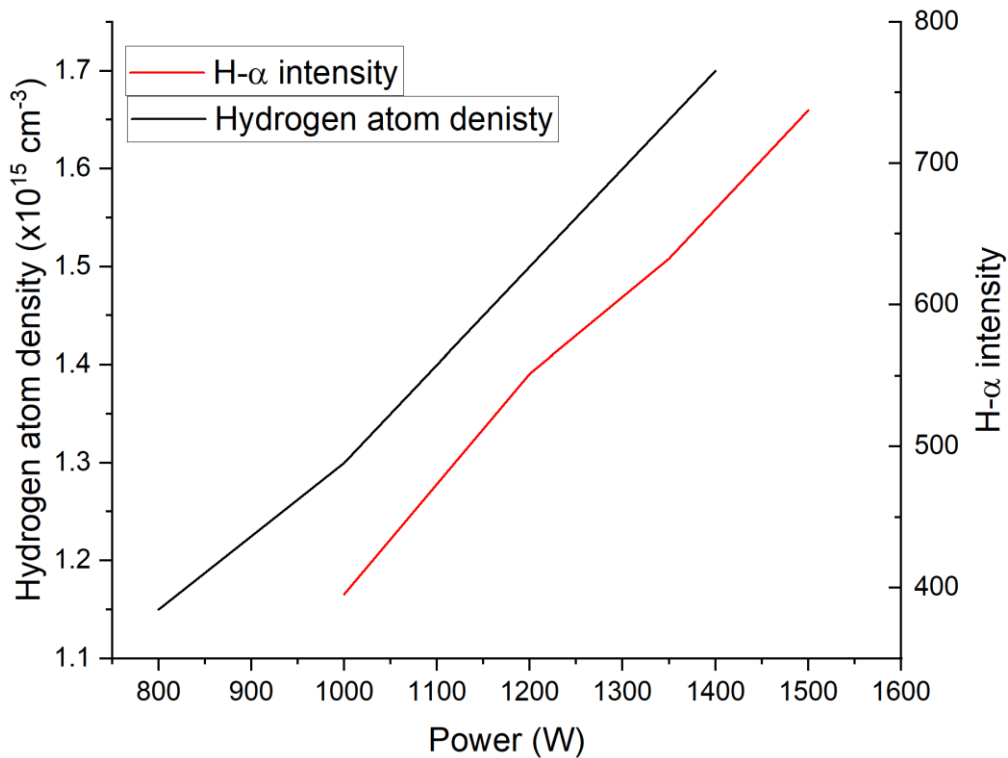


Figure 50: This graph shows the H- α transition intensities and hydrogen atom densities against power. The hydrogen atom densities are computer simulations taken from literature, where they are expected to show a linear relationship with the H- α and H- β transition intensities.⁴⁰

The best way to predict growth rates on the new magnetron is to compare to literature data, where similar growth conditions have been used. J. Asmussen *et al* used a 2.45 GHz MWPR, using a combination of TM₀₁₃ and TEM₀₀₁ modes to grow diamond film under a range of pressures at 4% CH₄ concentration.⁸⁷ Figure 51 shows literature data on the growth rates of diamond against pressures ranging from 180 – 240 torr, at a steady increase in power from 2.1-2.5 kW as pressure increases. Linear regression calculations were used to estimate the growth rate at 150 torr as this was the standard pressure used in the experiments. To maintain the change in power, the rate in change of power against pressure is:

$$\begin{aligned} \text{Rate of change} &= \frac{2500 - 2100}{240 - 180} \\ &= \frac{20}{3} \end{aligned}$$

So, if the pressure is increased by 1 torr, the power would increase by 20/3 to compensate, thus at 150 torr, the power is expected to be:

$$2100 - \left[\frac{20}{3} \times (180 - 150) \right] = 1900 \text{ W} .$$

The data point in green (8.11 $\mu\text{m/hr}$) of figure 51, is therefore an estimate of the of the literature data's growth rates at 150 torr and 1900 W, with a standard error of 0.41 $\mu\text{m/hr}$. The blue square is the experimental data point of 150 torr at 1500 W. Since the new magnetron is expected to be more energy efficient than the old one, the predicted growth rate is expected to fall in the range of the error bar of the green data point. This is based off the fact that the new magnetron is believed to be 10-35% more efficient, thus 1500 W on the new power supply could be more like 1650-2025 W effective. 1900 W falls somewhere in the middle of this; hence the growth rate should fall within the error bars of the green data point. So, for the new magnetron, the expected growth rate at 150 torr and 1500 W should be between 7.7 and 8.5 $\mu\text{m/hr}$ at the same substrate temperature.

There are some differences in the reactor setups used in the literature compared to the new magnetron, such as using different modes, cooling systems, and the substrates distance from the plasma. However, the data plotted is in accordance with the experimental data in this report and should be good enough for reasonable predictions for the new magnetron.

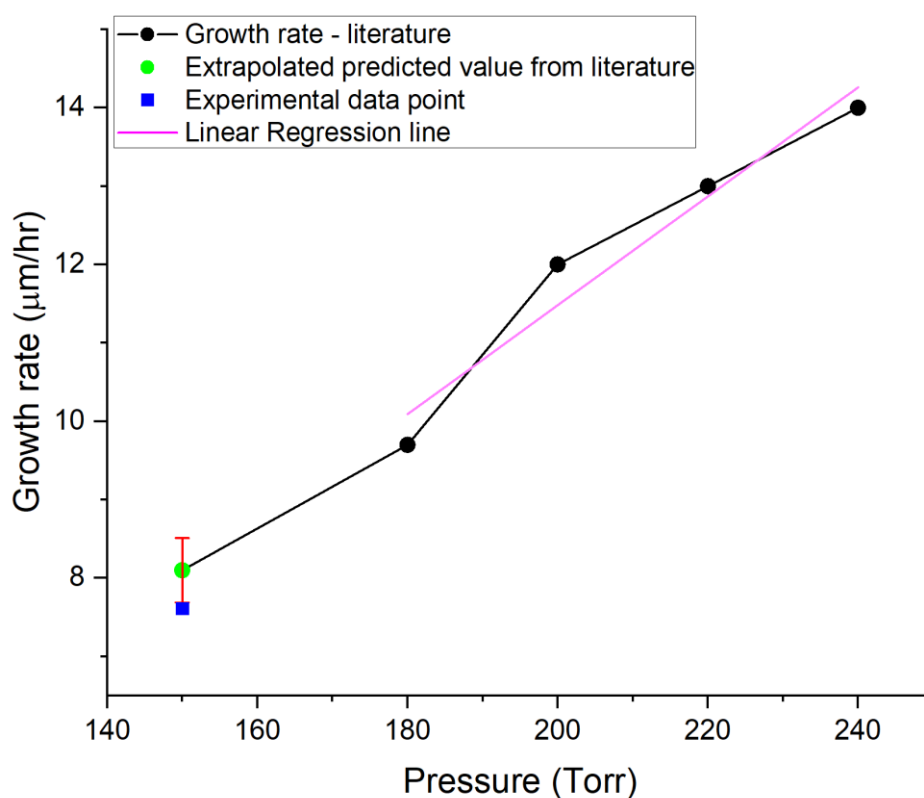


Figure 51: This graph shows a comparison in how growth rates change as a function of the pressure between the experimental data (blue square), and the literature data (black circle). A linear regression calculation (pink line) was completed for the literature data to find the expected growth rate at 150 torr and 1900 W (green circle). An error bar in red is shown to be 0.41 $\mu\text{m/hr}$ either side of the green circle.⁸⁷

It's hard to predict how much more efficient the new magnetron will be than compared to the old one, but sensible judgements can be made when comparing to microwave reactors of similar kind.⁸⁷ Whilst an increase in microwave power leads to more atomic hydrogen produced, the substrate temperature greatly influences the surface chemistry. When the runs are being replicated, all the

growths will happen at elevated temperatures when compared to the old magnetron, and these can be predicted when looking at figure 52. So, if the magnetron is expected to be 10-35% more efficient than the old one, i.e. a run at 1000 W was 820 °C using the old magnetron, the new magnetron might reach temperatures of around 910 °C. The morphology of the grains is dependent on the substrate temperature. Higher substrate temperatures cause {110} and {111} faces to become more dominant due to higher etching rates of {100} facets at temperatures beyond 1000 °C.²⁴

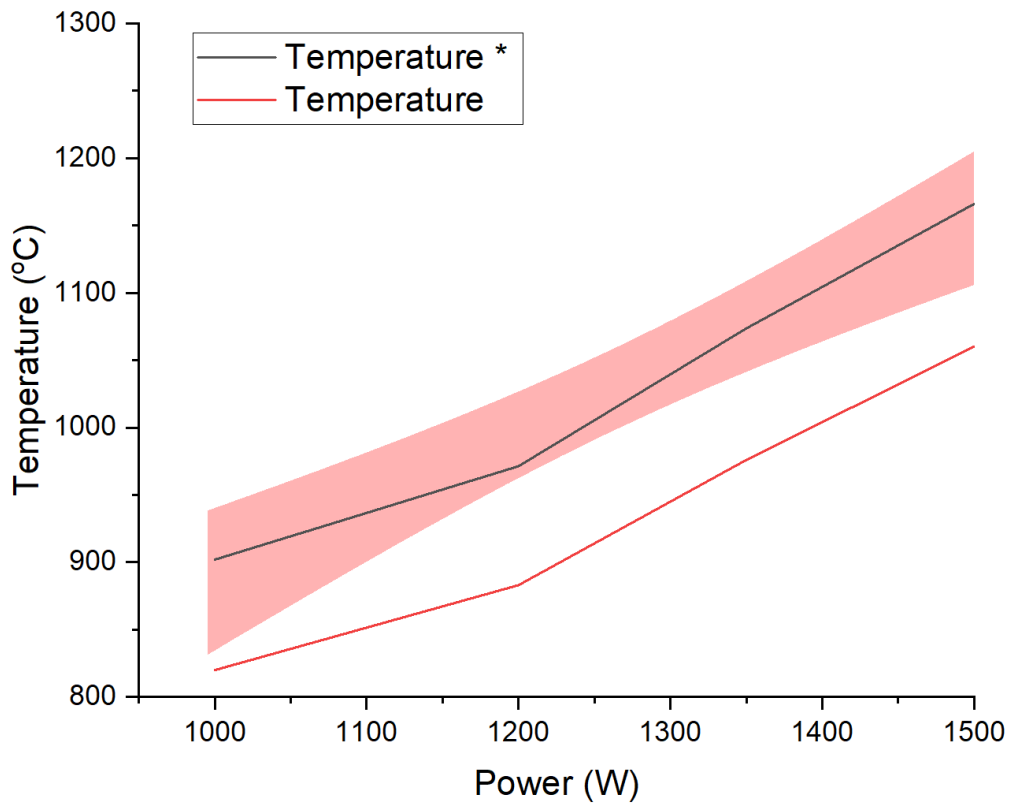


Figure 52: This graph shows how the substrate temperature varies with the microwave output power. Temperature* indicates the predicted temperatures, and the red band is the confidence level for which the predictions should fall between.

3. Conclusions

Diamond films grown under a range of different conditions were shown to have distinct differences in the film quality, growth rate, grain size and surface morphology.

Microwave plasma density is a known parameter that causes higher deposition rates of the reactive species in the plasma since hydrogen dissociation increases. As pressure increased from 100 to 200 torr, the MPD also increases as the plasma plume shrinks. Average grain sizes reached $7.88 \mu\text{m}^2$ at a reasonable growth rate of $5.77 \mu\text{m/hr}$ at 200 torr. The film for the high-pressure run was the worst quality when looking at the Raman spectra (figure 32), whilst standard conditions produced the highest quality films. {111} faces became more common as pressure increased due to higher substrate temperatures, which served to roughen the surface.

Using more microwave power causes the gas temperature and the substrate temperature to rise. This affects the rate at which highly reactive species are formed, i.e., hydrogen dissociation is dependent on temperature, and on the rate at which these reactive species nucleate onto the substrate. Changing the power was shown to significantly change the growth rates of the films. At 1000 W the growth rate was $1.79 \mu\text{m/hr}$, but when risen to 1350 W the growth rate increased over 5-fold to $9.00 \mu\text{m/hr}$. At higher powers, the benefit of higher growth rates is offset by a reduction in film quality as displayed in figure 36.

Referring to figure 9, conditions required for diamond growth are particularly sensitive to the gas composition.²² In the literature it was suggested that as methane concentration increased (up to 5% CH_4) the growth rate increased with worse film quality observed at low and high methane concentrations (<2%, > 6%).^{82, 83} This opposed the results obtained at the 6% methane growth. Raman spectroscopy was likely the source of error as the SEM images show darker, non-uniform grains, consisting of structural defects named striations, elucidating a high graphitic content on the surface.

Small amounts of nitrogen are known to enhance growth rate when added to the gas mixture during CVD of diamond.²⁵ Using 0-0.45 Sccm of nitrogen was found to boost growth rates from 4.96 to $5.68 \mu\text{m/hr}$, which conversely caused a reduction in grain size due to greater preference for sp^2 carbon formation. Raman spectra concluded that nitrogen doping greatly diminishes the film quality, but in exchange, electronic properties arise which offers promise for being used as semiconductors in industry.⁸⁸

Different wire thicknesses are used to alter the influence of the cooling system on the substrates temperature. Either side of the standard wire thickness (5 ml), it's realized that poorer quality film is grown as the substrate temperature becomes too hot or cold for diamond growth to be in its optimal range. Spectroscopic methods confirm the lesser quality by showing graphitic, and transpolyacetylene peaks in the Raman, and darker grains showing structural defects in SEM pictures.

Computer simulations obtained from literature data, calculated key growth parameters such as hydrogen concentration, electron density, and gas temperature. These were then used to predict output data for the new magnetron, whereby growth rates are expected to be 7.7 to $8.5 \mu\text{m/hr}$ at 150 torr and 1500 W. Increased growth rates are a result of a greater amount of hydrogen atoms

from higher MW plasma density, and these have been predicted using the intensity of the H- α and H- β transitions using OES data (figure 49).

4. Future Work

To extend this project, the growth runs completed on the old magnetron should be repeated for the new magnetron, where Raman spectroscopy, SEM, and OES will be used to characterise the diamond film and the plasmas characteristics. There is a major flaw however to this methodology, and that is the substrate temperature will be higher than the optimal levels for diamond growth. Whilst this method will show the exact differences in the magnetrons and the diamond grown at the same conditions, the diamond film won't be grown under optimal conditions. To maximise the benefits of using a higher power magnetron, the microwave plasma density should be increased, whilst the substrate temperature is in its optimal range between 850-950 °C. This can be done by altering the thickness of the spacer wire, as this effectively controls the substrate temperature, and high pressure and power to create high plasma densities. In this way, hydrogen dissociation is maximised, and hydrogen atoms and methyl radicals can nucleate on the substrate at ideal temperatures, to hopefully increase growth rates.

The setup for the new magnetron setup can be seen in figure 53, where a new magnetron, circulator, and directional coupler have been introduced. During this project the new magnetron was attempted to be integrated into the microwave reactor system. The component that prevented this process was the cooling system, where the water interlock mechanism failed due to being too sensitive. The water flow was changed, along with different pipes being used in efforts to get the water flow working properly. This ultimately, will affect how cold the cooling plate will get during synthesis, due to changing the flow rates, hence the substrate temperature will be affected when using the same conditions and spacer wire. When the interlock system gets fixed, it will be vital that under the same conditions, the substrate temperatures are the same for both the old and new magnetron growths.



Figure 53: An image of the new magnetron setup at UoB.

Other than optimising the new microwave plasma reactor for higher growth rates, it would be useful to optimise it for other purposes. When PCD is grown, the surface is generally very rough due to columnar growth, this causes an element of inherent porosity within the diamond film.⁸⁹ Attempting to grow smooth PCD surfaces would be useful for potential tribological purposes. This is because smooth PCD is less susceptible to thermal degradation under high friction and pressures.

Diamond being the most thermally conductive material, allows it to be utilised for heat spreading applications for high power electronics and X-ray lasers. The diamond grown in the results section can be seen to have a range of grain sizes when grown under different conditions. Large grains have shown to be more thermally conductive by R. B. Simon *et al*, where they have used 500 μm thick films to obtain high thermal conductivities, similar to that of single crystal diamond.⁹⁰ Therefore, to replicate similar results on the new magnetron, growth times will have to be greatly increased, i.e., if 10 $\mu\text{m/hr}$ growth rates are achieved, 50 hours is needed to grow 500 μm thick films.

It's important to know that the new magnetron setup isn't solely the changing of magnetrons, but also involves new directional couplers and circulators being used. Using equations **10** and **11** in section 2.5.2, the power output of the magnetron can be quantified, and thus the true power transmission from the magnetron to the waveguide can be measured. These measurements can then be compared to the old setup for a range of powers. Plotting the power outputs on a graph against the input power for both reactor set ups, will yield the offset of the powers generated by the

reactors. The power loss from the attenuation in the waveguide and mode converter can be ignored since they are both the same.

5. Experimental Details

5.1 Substrates and Abrasion

All diamond growths were carried out on the same n-type silicon wafer that were cut using an Oxford Lasers laser cutting machine. This produced many 1 cm x 1 cm samples of 500-550 μm in thickness. The substrates were then manually abraded using diamond nanoparticles. This involved putting a pinch of diamond nanoparticles on one substrate, and then placing another substrate on top of it, making sure the shiny side faced inwards. Pressure was applied to the top layer using a metal instrument and was moved around to create friction. A high pitched squeak was heard when doing the manual abrasion, and this indicated that the substrates were being abraded. The two substrates were then flipped over once all edges were covered of the bottom substrate, and the same abrasion process was completed for the other substrate. The substrates were then cleaned with acetone using a cotton wool bud.

5.2 The University of Bristol MWPR

A brief description of the MWPR at the University of Bristol (UoB) has already been mentioned, and this is the reactor that has been used in the growth of CVD diamond for this thesis. The machinery was made by Element Six, Ltd based upon an ASTeX design (figure 54). Microwaves are generated by a 1.5 kW ASTeX magnetron (HS-1000) that are attached to the chamber using a directional coupler (DCS-1000). Some power can be reflected and thus lost from the chamber. To minimise losses a waveguide system is introduced to slightly alter the height at which the microwaves are released at. The substrate sits on a molybdenum plate which is on top of a tungsten spacer wire (variable thicknesses were used) which then sits on a water-cooled surface. The cylindrical aluminium chamber is also water cooled and is divided by a vacuum-sealed silica window (Knight optical UV Grade, 119.5 mm diameter x 7.44 mm thickness). Gas inlets are attached to the chamber where a variety of gases can be pumped in at specific flow rates.

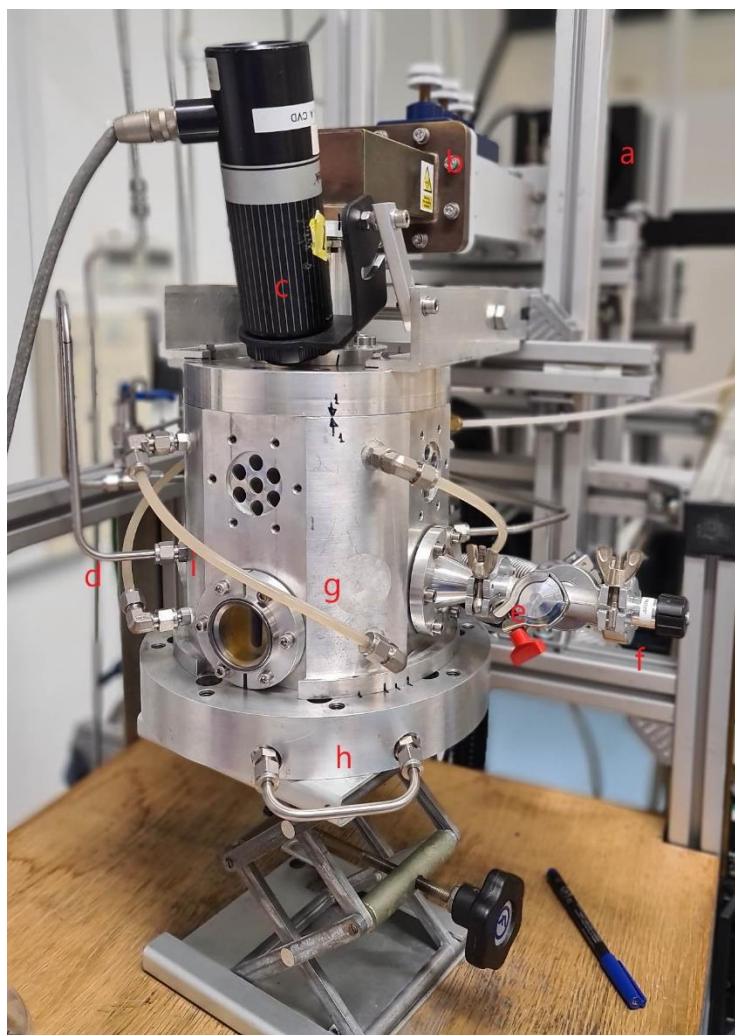


Figure 54: A picture of the microwave plasma reactor at the School of Chemistry, University of Bristol. (a) magnetron, (b) waveguide, (c) optical pyrometer, (d) gas inlet, (e) vacuum exhaust pump, (f) gas inlet, (g) vacuum chamber, (h) water cooled base plate, (i) water cooling system.

5.3 Growth Runs Using the MWPR

The substrates were loaded into the microwave chamber on a molybdenum disk that sat on top of a spacer wire. The plasma was ignited when the power reached 450 W in a pure H₂ atmosphere at 15 torr. Once the plasma had grown, and the pressure was dialled up to 50 torr, other gases (CH₄, N₂) were added to the chamber through mass flow controllers (MFCs). The pressure and power dials were slowly increased until the desired parameters were reached (table 4). Safety interlocks were turned on, and the growth times were kept to 6 hours long, where the MWPR was checked every 30 minutes. After growth times, the MWPR was turned off, and the sample was collected and placed in a container for Raman spectroscopy and SEM.

A 2.2 μm , single wavelength pyrometer was used to measure the temperature of the substrate. The emissivity value for the silicon substrate is 0.19, and this was used to calibrate the pyrometer.

Table 4: This table shows all the growth runs using the Astex-seki reactor design. Samples 1, 13, and 15 have been omitted due to problems occurring with the reactor.

Sample number	Power (W)	Pressure (Torr)	Wire thickness (ml)	Methane flow rate (Sccm)	Hydrogen flow rate (Sccm)	Nitrogen flow rate (Sccm)
2	1000	150	5	12.5	300	0
3	1200	150	5	12.5	300	0
4	1350	150	5	12.5	300	0
5	1500	150	5	12.5	300	0
6	1200	200	5	12.5	300	0
7	1200	100	5	12.5	300	0
8	1200	150	8	12.5	300	0
9	1200	150	2.5	12.5	300	0
10	1200	150	0	12.5	300	0
11	1200	150	5	6.25	300	0
12	1200	150	5	18.75	300	0
13	N/A	N/A	N/A	N/A	N/A	N/A
14	1200	150	5	12.5	300	0.3
15	N/A	N/A	N/A	N/A	N/A	N/A
16	1200	150	5	12.5	300	0.45
17	1200	150	5	12.5	300	0.15

5.4 Characterisation Apparatus

5.4.1 Raman Spectroscopy

The Raman spectroscopy setup involved using a Renishaw 2000 laser spectrometer, where a 514 nm green laser was used. All spectra collected were measured using 10 % laser power, with 10, 2-second-long acquisitions. The data was then normalised and fitted using origin software.

5.4.2 SEM

All SEM images used in this report were collected using the University of Bristol Chemistry departments SEM instrument. A Jeol IT300 SEM system was used where both top view and side view images were collected. The samples were cut in half using a scribe and were mounted at a 70 ° degree angle. To measure the thickness of the samples the angle must be accounted for, hence Pythagoras's theorem was used. The grain sizes were measured using ImageJ software, where areas of all grain were measured, and then an average was taken.

5.4.3 OES

A single point probe was used to gauge the plasma chemistry from the centre of the plasma. A Broadcom Qmini OES system with a kodial window was used for the OES system, where PGOPHER was used as the software for processing the data.

6. Bibliography

1. P. *Allotropes of Carbon: Structures, Properties & Examples*. 2022. <https://www.embibe.com/exams/allotropes-of-carbon/#:~:text=Allotropes%20of%20Carbon%20are%20referred%20to%20elements%20that,of%20forming%20many%20allotropes%20cause%20of%20its%20valency>, (accessed 18/10/22)
2. F. P. Bundy, W. A. Bassett, M. S. Weathers, R. J. Hemley, H. U. Mao and A. F. Goncharov, *Carbon*, 1996, **34**, 141–153.
3. C. Liu, J.-H. Wang and J. Weng, *Journal of Crystal Growth*, 2015, **410**, 30–34.
4. A. Tallaire, J. Achard, F. Silva, R. S. Sussmann and A. Gicquel, *Diamond and Related Materials*, 2005, **14**, 249–254.
5. Y. A. Sorb, F. P. Bundy and R. C. DeVries, *Reference Module in Materials Science and Materials Engineering*, 2016.
6. B. B. Bokhonov, D. V. Dudina and M. R. Sharafutdinov, *Diamond and Related Materials*, 2021, **118**, 108563.
7. F. P. Bundy, H. T. Hall, H. M. Strong and R. H. Wentorfjun., *Nature*, 1955, **176**, 51–55.
8. H. Schmellenmeier, *Zeitschrift für Physikalische Chemie*, 1956, **2050**, 349–350.
9. J. J. Gracio, Q. H. Fan and J. C. Madaleno, *Journal of Physics D: Applied Physics*, 2010, **43**, 374017.
10. S. Matsumoto, Y. Sato, M. Tsutsumi and N. Setaka, *Journal of Materials Science*, 1982, **17**, 3106–3112.
11. R. Haubner, *ChemTexts*, 2021, **7**, 10.
12. P. W. May, *Philosophical Transactions of the Royal Society of London. Series A: Mathematical, Physical and Engineering Sciences*, 2000, **358**, 473–495.
13. C. M. Donnelly, R. W. McCullough and J. Geddes, *Diamond and Related Materials*, 1997, **6**, 787–790.
14. W. Banholzer, *Surface and Coatings Technology*, 1992, **53**, 1–12.
15. M. G. Jubber, J. I. B. Wilson, I. C. Drummond, P. John and D. K. Milne, *Diamond and Related Materials*, 1993, **2**, 402–406.
16. V. Damle, K. Wu, O. De Luca, N. Ortí-Casañ, N. Norouzi, A. Morita, J. de Vries, H. Kaper, I. S. Zuhorn, U. Eisel, D. E. P. Vanpoucke, P. Rudolf and R. Schirhagl, *Carbon*, 2020, **162**, 1–12.
17. R. Tu, T. Xu, D. Li, S. Zhang, M. Yang, Q. Li, L. Zhang, T. Shimada, T. Goto and J. Shi, *RSC Advances*, 2018, **8**, 16061–16068.
18. R. Haubner, & B. Lux, *Hard Metals*, 1987, **6** (4) 210-215
19. M. Nishitani-Gamo, I. Sakaguchi, K. Ping Loh, Tomohide Takami, I. Kusunoki, and T. Ando, *Diamond and Related Materials*, 1999, **8**, 693–700.
20. CVD Diamond Group - School of Chemistry - Bristol University, <http://www.chm.bris.ac.uk/pt/diamond/semflat.htm>, (accessed 15/11/22)
21. J. Weng, L. W. Xiong, J. H. Wang, S. Y. Dai, W. D. Man and F. Liu, *Diamond and Related Materials*, 2012, **30**, 15–19.
22. P. K. Bachmann, D. Leers and H. Lydtin, *Diamond and Related Materials*, 1991, **1**, 1–12.
23. A. Tallaire, J. Achard, O. Brinza, V. Mille, M. Naamoun, F. Silva and A. Gicquel, *Diamond and Related Materials*, 2013, **33**, 71–77.
24. C. C. Battaile, D. J. Srolovitz, I. I. Oleinik, D. G. Pettifor, A. P. Sutton, S. J. Harris and J. E. Butler, *The Journal of Chemical Physics*, 1999, **111**, 4291–4299.
25. J. Achard, F. Silva, A. Tallaire, X. Bonnin, G. Lombardi, K. Hassouni and A. Gicquel, *Journal of Physics D: Applied Physics*, 2007, **40**, 6175–6188.

26. J. Achard, F. Silva, O. Brinza, A. Tallaire and A. Gicquel, *Diamond and Related Materials*, 2007, **16**, 685–689.
27. A. Tallaire, A. T. Collins, D. Charles, J. Achard, R. Sussmann, A. Gicquel, M. E. Newton, A. M. Edmonds and R. J. Cruddace, *Diamond and Related Materials*, 2006, **15**, 1700–1707.
28. S. Kanagasabay, *Current Approaches to Occupational Health*, 1982, ch. 7, 134–168.
29. J. G. Brennan, *Encyclopedia of Food Sciences and Nutrition*, 2003, 1938–1942.
30. A. Harrison and A. G. Whittaker, *Comprehensive Coordination Chemistry II*, 2003, 741–745.
31. D. M. Mingos and D. R. Baghurst, *Chemical Society Reviews*, 1991, **20**, 1.
32. F. Mehmood, T. Kamal and U. Ashraf, *Preprints.org*, 2018.
33. E. Igenbergs, J. Sporer, M. Rott and K. G. Schmitt-Thomas, *IEEE Transactions on Magnetics*, 1995, **31**, 735–739.
34. H. Conrads and M. Schmidt, *Plasma Sources Science and Technology*, 2000, **9**, 441–454.
35. F. L. Tabares and I. Junkar, *Molecules*, 2021, **26**, 1903.
36. F. Silva, K. Hassouni, X. Bonnin and A. Gicquel, *Journal of Physics: Condensed Matter*, 2009, **21**, 364202.
37. P. Capezuto, F. Cramarossa, R. D'Agostino and E. Molinari, *The Journal of Physical Chemistry*, 1975, **79**, 1487–1496.
38. T. Sharda, D. S. Misra, D. K. Avasthi and G. K. Mehta, *Solid State Communications*, 1996, **98**, 879–883.
39. G. J. Hagelaar, K. Hassouni and A. Gicquel, *Journal of Applied Physics*, 2004, **96**, 1819–1828.
40. K. Hassouni, F. Silva and A. Gicquel, *Journal of Physics D: Applied Physics*, 2010, **43**, 153001.
41. Y. A. Lebedev, *Plasma Sources Science and Technology*, 2015, **24**, 053001.
42. J. E. Brittain, *Physics Today*, 1985, **38**, 60–67.
43. Lesics, Magnetron, How does it work?, <https://www.youtube.com/watch?v=bUsS5KUMLvw>, (accessed 5/03/23).
44. Microwave Engineering – Magnetrons, https://www.tutorialspoint.com/microwave_engineering/microwave_engineering_magnetrons.htm, (accessed 5/03/23)
45. The Magnetron, <http://hyperphysics.phy-astr.gsu.edu/hbase/Waves/magnetron.html>, (accessed 5/03/23)
46. Ms. V. Bharathi, *Microwave Engineering (15A04703) lecture Notes*, Vemu Institute of Technology, 2019.
47. D. M. Pozar, *Microwave Engineering*, 2nd Edition, New York, Wiley, 1998, **3**, 105-181
48. X. Cui, G. Wang, T. Jiang, H. Shao, J. Sun, X. Wu, X. Bai, X. Zhang and Z. Zhang, *IEEE Access*, 2018, **6**, 14996–15003.
49. X. Zhao, C. Yuan, Q. Zhang and L. Zhao, *Review of Scientific Instruments*, 2016, **87**, 074707.
50. H. Gong, C. Yuan, X. Zhao and Q. Zhang, *AIP Advances*, 2019, **9**, 045114.
51. S. C. Halliwell, PhD thesis, University of Bristol, 2017.
52. 3.3 mode TM01. https://www.qwed.eu/QuickWave/qwmodeller_help/microwave_course/3_3_mode_tm01.htm, (accessed, 28/11/22)
53. F. Silva, A. Michau, X. Bonnin, A. Gicquel, N. Boutroy, N. Chomel and L. Desoutter, *Diamond and Related Materials*, 2007, **16**, 1278–1281.
54. Y. F. Li, J. J. Su, Y. Q. Liu, M. H. Ding, X. L. Li, G. Wang, P. L. Yao and W. Z. Tang, *Diamond and Related Materials*, 2014, **44**, 88–94.
55. J. Asmussen, J. Zhang, US Patents, 5311103, 890877, 1994.
56. W. Tan and T. A. Grotjohn, *Journal of Vacuum Science & Technology A: Vacuum, Surfaces, and Films*, 1994, **12**, 1216–1220.
57. Dielectric Resonators, <https://exxelia.com/uploads/PDF/e7000-v1.pdf>, (accessed 5/01/23)
58. Resonant Cavities and Waveguides, <C:\CPA\Chap12\chap12.wpd> (mit.edu), (accessed 8/12/22)

59. C.S. Meierbachtol, PhD Thesis, Michigan State University, 2013.
60. X. J. Li, W. Z. Tang, F. Y. Wang, C. M. Li, L. F. Hei and F. X. Lu, *Diamond and Related Materials*, 2011, **20**, 374–379.
61. M. Fünér, C. Wild and P. Koidl, *Surface and Coatings Technology*, 1999, **116-119**, 853–862.
62. Iplas innovative plasma systems, <https://www.iplas.de/en>, (accessed 7/02/23)
63. S. Kunuku, K. J. Sankaran, K.-C. Leou and I.-N. Lin, *Materials Research Express*, 2017, **4**, 025001.
64. M. S. Komlenok, V. V. Kononenko, V. M. Gololobov and V. I. Konov, *Quantum Electronics*, 2016, **46**, 125–127.
65. J. Achard, V. Jacques and A. Tallaire, *Journal of Physics D: Applied Physics*, 2020, **53**, 313001.
66. E. L. Thomas, L. Ginés, S. Mandal, G. M. Klemencic and O. A. Williams, *AIP Advances*, 2018, **8**, 035325.
67. S. M. Leeds, PhD Thesis, University of Bristol, 1999
68. C. Wang, M. Irie and T. Ito, *Diamond and Related Materials*, 2000, **9**, 1650–1654.
69. J. Weng, F. Liu, L. W. Xiong, J. H. Wang and Q. Sun, *Vacuum*, 2018, **147**, 134–142.
70. D. K. Smith, M. P. J. Gaudreau, US Patents, 4866346, 65281, 1987
71. P. Fortugno, S. Musikhin, X. Shi, H. Wang, H. Wiggers and C. Schulz, *Carbon*, 2022, **186**, 560–573.
72. J. H. Robert *et al*, European Patent Specification, 11799160.4, 2011
73. A. Mallik, *Journal of Coating Science and Technology*, 2016, **3**, 75–99.
74. M. Griesser, M. Grasserbauer, R. Kellner, S. Bohr, R. Haubner and B. Lux, *Fresenius' Journal of Analytical Chemistry*, 1995, **352**, 763–770.
75. S. Praver and R. J. Nemanich, *Philosophical Transactions of the Royal Society of London. Series A: Mathematical, Physical and Engineering Sciences*, 2004, **362**, 2537–2565.
76. A. C. Ferrari and J. Robertson, *Physical Review B*, 2001, **63**.
77. E. J. Mahoney, B. S. Truscott, M. N. Ashfold and Y. A. Mankelevich, *The Journal of Physical Chemistry A*, 2017, **121**, 2760–2772.
78. K. W. Hemawan and R. J. Hemley, *Journal of Vacuum Science & Technology A: Vacuum, Surfaces, and Films*, 2015, **33**, 061302.
79. K. W. Hemawan and R. J. Hemley, *Journal of Vacuum Science & Technology A: Vacuum, Surfaces, and Films*, 2015, **33**, 061302.
80. R. Tu, T. Xu, D. Li, S. Zhang, M. Yang, Q. Li, L. Zhang, T. Shimada, T. Goto and J. Shi, *RSC Advances*, 2018, **8**, 16061–16068.
81. M. A. Pimenta, G. Dresselhaus, M. S. Dresselhaus, L. G. Cançado, A. Jorio and R. Saito, *Phys. Chem. Chem. Phys.*, 2007, **9**, 1276–1290.
82. Wang, Duan, Cao, Liu, Wang, Peng and Hu, *Materials*, 2019, **12**, 3953.
83. B. A. Reshi, S. Kumar, A. Misra and R. Varma, *Materials Research Express*, 2019, **6**, 046407.
84. A. Mohanta, B. Lanfant, M. Asfaha and M. Leparoux, *Journal of Physics: Conference Series*, 2017, **825**, 012010.
85. F. K. de Theije, J. J. Schermer and W. J. P. van Enkevort, *Diamond and Related Materials*, 2000, **9**, 1439–1449.
86. S. Iordanova, I. Koleva and T. Paunskas, *Spectroscopy Letters*, 2011, **44**, 8–16.
87. K.W. Hemawan, T. A. G., D.K. Reinhard, J. Asmussen, *Diamond and Related Materials* 2010, **19**, 1446-1452.
88. D. Araujo, M. Suzuki, F. Lloret, G. Alba and P. Villar, *Materials*, 2021, **14**, 7081.
89. A. Kumar Mallik, *Some Aspects of Diamonds in Scientific Research and High Technology*, 2020.
90. R. B. Simon, J. Anaya, F. Faily, R. Balmer, G. T. Williams, D. J. Twitchen and M. Kuball, *Applied Physics Express*, 2016, **9**, 061302.

